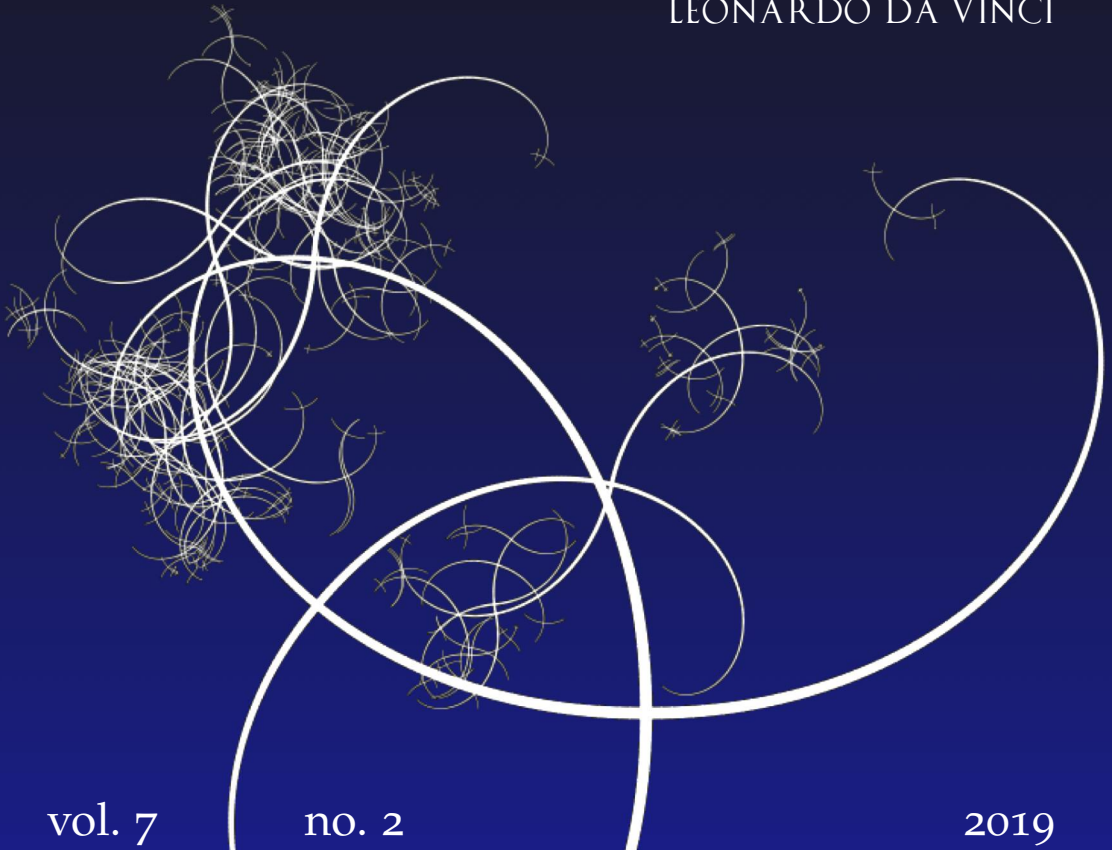


NISSUNA UMANA INVESTIGAZIONE SI PUO DIMANDARE  
VERA SCIENZA S'ESSA NON PASSA PER LE  
MATEMATICHE DIMOSTRAZIONI  
LEONARDO DA VINCI



vol. 7

no. 2

2019

MATHEMATICS AND MECHANICS  
*of*  
**Complex Systems**



# MATHEMATICS AND MECHANICS OF COMPLEX SYSTEMS

[msp.org/memocs](http://msp.org/memocs)

## EDITORIAL BOARD

ANTONIO CARCATERRA	Università di Roma "La Sapienza", Italia
ERIC A. CARLEN	Rutgers University, USA
FRANCESCO DELL'ISOLA	(CO-CHAIR) Università di Roma "La Sapienza", Italia
RAFFAELE ESPOSITO	(TREASURER) Università dell'Aquila, Italia
ALBERT FANNJIANG	University of California at Davis, USA
GILLES A. FRANCFORT	(CO-CHAIR) Université Paris-Nord, France
PIERANGELO MARCATI	Università dell'Aquila, Italy
JEAN-JACQUES MARIGO	École Polytechnique, France
PETER A. MARKOWICH	DAMTP Cambridge, UK, and University of Vienna, Austria
MARTIN OSTOJA-STARZEWSKI	(CHAIR MANAGING EDITOR) Univ. of Illinois at Urbana-Champaign, USA
PIERRE SEPPECHER	Université du Sud Toulon-Var, France
DAVID J. STEIGMANN	University of California at Berkeley, USA
PAUL STEINMANN	Universität Erlangen-Nürnberg, Germany
PIERRE M. SUQUET	LMA CNRS Marseille, France

## MANAGING EDITORS

MICOL AMAR	Università di Roma "La Sapienza", Italia
ANGELA MADEO	Université de Lyon-INSA (Institut National des Sciences Appliquées), France
MARTIN OSTOJA-STARZEWSKI	(CHAIR MANAGING EDITOR) Univ. of Illinois at Urbana-Champaign, USA

## ADVISORY BOARD

ADNAN AKAY	Carnegie Mellon University, USA, and Bilkent University, Turkey
HOLM ALTENBACH	Otto-von-Guericke-Universität Magdeburg, Germany
MICOL AMAR	Università di Roma "La Sapienza", Italia
HARM ASKES	University of Sheffield, UK
TEODOR ATANACKOVIĆ	University of Novi Sad, Serbia
VICTOR BERDICHEVSKY	Wayne State University, USA
GUY BOUCHITTÉ	Université du Sud Toulon-Var, France
ANDREA BRAIDES	Università di Roma Tor Vergata, Italia
ROBERTO CAMASSA	University of North Carolina at Chapel Hill, USA
MAURO CARFORE	Università di Pavia, Italia
ERIC DARVE	Stanford University, USA
FELIX DARVE	Institut Polytechnique de Grenoble, France
ANNA DE MASI	Università dell'Aquila, Italia
GIANPIETRO DEL PIERO	Università di Ferrara and International Research Center MEMOCS, Italia
EMMANUELE DI BENEDETTO	Vanderbilt University, USA
VICTOR A. EREMEYEV	Gdansk University of Technology, Poland
BERNOLD FIEDLER	Freie Universität Berlin, Germany
IRENE M. GAMBA	University of Texas at Austin, USA
DAVID Y. GAO	Federation University and Australian National University, Australia
SERGEY GAVRILYUK	Université Aix-Marseille, France
TIMOTHY J. HEALEY	Cornell University, USA
DOMINIQUE JEULIN	École des Mines, France
ROGER E. KHAYAT	University of Western Ontario, Canada
CORRADO LATTANZIO	Università dell'Aquila, Italy
ROBERT P. LIPTON	Louisiana State University, USA
ANGELO LUONGO	Università dell'Aquila, Italia
ANGELA MADEO	Université de Lyon-INSA (Institut National des Sciences Appliquées), France
JUAN J. MANFREDI	University of Pittsburgh, USA
CARLO MARCHIORO	Università di Roma "La Sapienza", Italia
ANIL MISRA	University of Kansas, USA
ROBERTO NATALINI	Istituto per le Applicazioni del Calcolo "M. Picone", Italy
PATRIZIO NEFF	Universität Duisburg-Essen, Germany
THOMAS J. PENCE	Michigan State University, USA
ANDREY PIATNITSKI	Narvik University College, Norway, Russia
ERRICO PRESUTTI	Università di Roma Tor Vergata, Italy
MARIO PULVIRENTI	Università di Roma "La Sapienza", Italia
LUCIO RUSSO	Università di Roma "Tor Vergata", Italia
MIGUEL A. F. SANJUAN	Universidad Rey Juan Carlos, Madrid, Spain
PATRICK SELVADURAI	McGill University, Canada
MIROSLAV ŠILHAVÝ	Academy of Sciences of the Czech Republic
GUIDO SWEERS	Universität zu Köln, Germany
ANTOINETTE TORDÉSILLAS	University of Melbourne, Australia
LEV TRUSKINOVSKY	École Polytechnique, France
JUAN J. L. VELÁZQUEZ	Bonn University, Germany
VINCENZO VESPRI	Università di Firenze, Italia
ANGELO VULPIANI	Università di Roma La Sapienza, Italia

MEMOCS (ISSN 2325-3444 electronic, 2326-7186 printed) is a journal of the International Research Center for the Mathematics and Mechanics of Complex Systems at the Università dell'Aquila, Italy.

Cover image: "Tangle" by © John Horigan; produced using the *Context Free* program ([contextfreeart.org](http://contextfreeart.org)).

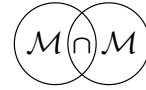
PUBLISHED BY



mathematical sciences publishers  
nonprofit scientific publishing

<http://msp.org/>

© 2019 Mathematical Sciences Publishers



## A POLYNOMIAL CHAOS EXPANDED HYBRID FUZZY-STOCHASTIC MODEL FOR TRANSVERSELY FIBER REINFORCED PLASTICS

EDUARD PENNER, ISMAIL CAYLAK, ALEX DRIDGER AND ROLF MAHNKEN

This work is focused on polymorphic uncertainties in the framework of constitutive modeling for transversely isotropic materials. To this end, we propose a hybrid fuzzy-stochastic model, where the stochastic part accounting for aleatory uncertainties of material parameters is expanded with the multivariate polynomial chaos expansion. In order to account for epistemic uncertainties, polynomial chaos coefficients are treated as fuzzy variables. The underlying minimum and maximum optimization problem for the fuzzy analysis is approximated by  $\alpha$ -level discretization, resulting in a separation of minimum and maximum problems. To become more universal, so-called quantities of interest are employed, which allow a general formulation for the target problem. Numerical examples with fuzzy, fuzzy-stochastic, and hybrid fuzzy-stochastic input demonstrate the versatility of the proposed formulation.

### 1. Introduction

A fundamental data uncertainty of different types underlies most materials in engineering science. Possible examples are variations in the manufacturing process, where composites are typical materials, measurement errors, and missing or incomplete information. In order to improve the credibility of mathematical models in engineering science, uncertainties have to be taken into account, where two categories are distinguished: aleatory and epistemic; see, e.g., [Sullivan 2015].

Aleatory uncertainties refer to variability as a consequence of, e.g., fluctuations through time, variation across space, or manufacturing differences. This type of uncertainty is irreducible and can be treated with a stochastic analysis. An aleatory uncertain problem of a mechanical system can be modeled by stochastic partial differential equations (SPDEs), where the system response may be described by a distribution with statistical moments. The solution of these SPDEs can be obtained

---

**Communicated by Paul Steinmann.**

*MSC2010:* 60A86.

*Keywords:* polymorphic uncertainty, fuzzy, stochastic, fuzzy-stochastic, polynomial chaos expansion, fiber reinforced plastics, transversely isotropic materials, imprecise probability, epistemic, aleatory.

numerically using a stochastic simulation, where the Monte Carlo (MC) method [Caffisch 1998; Hurtado and Barbat 1998] is widely used. Alternatively, spectral stochastic surrogate models, e.g., polynomial chaos expansion (PCE), are used in order to reduce the computational effort. Corresponding research areas are: linear elasticity of solids and mechanics [Ghanem and Spanos 1991], plasticity of solids and mechanics [Anders and Hori 1999; Rosić 2013], large deformations [Acharjee and Zabarar 2006; Acharjee 2006; Caylak et al. 2018], fluid flow [Le Maître et al. 2001; 2002], flow-structure interactions [Xiu and Karniadakis 2002; Xiu et al. 2001], and linear convection problems [Jardak et al. 2002].

Contrary to aleatory uncertainties, epistemic uncertainties refer to subjectivity as a consequence of, e.g., incomplete scientific understanding or lack of measurements, which indicate a possible value range rather than a probability function. In addition, epistemic uncertainties are reducible by empirical effort, e.g., investing more in measurements. Methodologies for the modeling of epistemic uncertainties are, e.g., interval analysis and, increasingly applied over the last years, fuzzy analysis, which represents indistinct boundaries [Zadeh 1965]. In order to perform mathematical operations with fuzzy sets, the so-called  $\alpha$ -level discretization method is applied. Here, the fuzzy response at each selected  $\alpha$ -level is obtained by solving a minimum-maximum problem of a *quantity of interest* (QoI). In [Mahnken 2017] QoIs are employed within a variational formulation for fuzzy analysis in continuum mechanics.

A realistic modeling of uncertainties requires a combination of different uncertainty types. Following [Graf et al. 2015], this is referred to as polymorphic uncertainties. Corresponding models are: Dempster–Shafer evidence theory [Dempster 1967], coherent lower prevision theory [Walley 1991], possibility theory [Dubois and Prade 2012], probability box (P-box) theory [Ferson et al. 2003], and fuzzy probability theory [Gudder 1998; Beer 2009] or fuzzy-randomness [Möller and Beer 2004]. Recently published works using fuzzy-randomness are in the field of civil engineering [Reuter et al. 2012], fuzzy-random dynamical structural analysis [Graf et al. 2015], failure probability evaluation [Jahani et al. 2014], and fuzzy-stochastic partial differential equations [Motamed 2017].

Note that the QoI in the publications listed in the previous paragraph may be a fuzzy-stochastic random variable. The numerical computation of the stochastic part is realized by sampling methods which require a large number of samples. From the received samples, different statistical moments can be computed to solve the minimum-maximum problem of the QoI at each  $\alpha$ -level. Thus, at each optimization step, statistical moments must be determined, which lead to high computational costs. In order to reduce this effort, we introduce a novel hybrid fuzzy-stochastic model based on the polynomial chaos expansion. In particular the following aspects are investigated:

- The stochastic part of the hybrid polymorphic model is expanded with the PCE.
- For the fuzzy part of the hybrid polymorphic model, the polynomial chaos (PC) coefficients are treated as fuzzy variables.
- At each optimization step, the statistical moment only depends on deterministic PC coefficients.
- Experimental investigation and uncertainty quantification of transversely fiber reinforced plastics are carried out.

This paper is structured as follows. Section 2 provides the stochastic formulation for the state and target problem and their discretizations with the PCE. In Section 3 the hybrid fuzzy-stochastic formulation and the computational scheme for the numerical implementation with polymorphic uncertainties are proposed. Section 4 incorporates the experimental investigation and the parameter identification for fiber reinforced plastics (FRP). Finally, in Section 5 the representative numerical examples demonstrate the versatility of the proposed model considering different types of uncertainties.

## 2. Stochastic analysis

**2.1. Constitutive stochastic state problem.** To set the stage for a hybrid fuzzy-stochastic model accounting for polymorphic uncertainties, we introduce a design vector

$$[s_1, \dots, s_{n_s}]^T = \underline{s} \in \mathcal{S} \tag{1}$$

within a design space  $\mathcal{S} \subset \mathbb{R}^{n_s}$  of  $n_s$  design variables. In general it may represent several influences on a structure, such as material properties, loading parameters, geometric properties, and boundary conditions. In this section, we assume the design space  $\mathcal{S} \subset \mathbb{R}^{n_s}$  in (1) is a precise set or a fundamental set of ordered pairs. The aleatory uncertainties are modeled by stochastic random variables. In this context the probability space is denoted by  $(\Omega, \Sigma, \mathbb{P})$ , where  $\Omega$  is the set of elementary events,  $\Sigma$  is the  $\sigma$ -algebra, and  $\mathbb{P}$  is the probability measure. Moreover, we let  $\omega$  be an element of  $\Omega$ .

Typically, constitutive modeling in mechanics is based on stress-strain relations. To this end, we introduce a stress-strain space  $\mathcal{M} \subset \mathcal{E}^3 \times \mathcal{E}^3$ , where  $\mathcal{E}^3$  denotes the Euclidean space. An uncertain functional for a strain tensor  $\boldsymbol{\epsilon}$  on the design space  $\mathcal{S}$  and on the probability space  $\Omega$  may be interpreted as a random variable  $\boldsymbol{\epsilon}(\cdot, \underline{s}) : \Omega \rightarrow \mathcal{M}$  indexed by  $\underline{s} \in \mathcal{S}$  on the design space  $\mathcal{S}$ , where for any elementary event  $\omega$  yields a realization  $\boldsymbol{\epsilon}(\omega, \cdot) : \mathcal{S} \rightarrow \mathcal{M}$ ; see, e.g., [Wang and Zhang 1992].

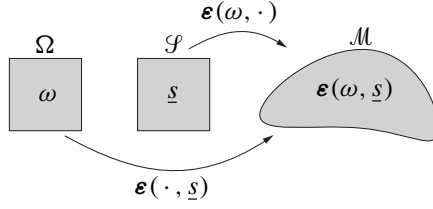


**Figure 1.** Mapping from stochastic and design space to strain space.

In both interpretations, an uncertain functional is a measurable function

$$\boldsymbol{\varepsilon}(\omega, \underline{s}) := \begin{cases} \Omega \times \mathcal{S} \rightarrow \mathcal{M} \subset \mathcal{E}^3 \times \mathcal{E}^3, \\ (\omega, \underline{s}) \mapsto \boldsymbol{\varepsilon}(\omega, \underline{s}). \end{cases} \quad (2)$$

The mapping  $\boldsymbol{\varepsilon}(\cdot, \cdot)$  from stochastic and design space to strain space is visualized in Figure 1, where for simplicity time dependence, explicit probabilistic dependence, and explicit design dependence are not considered in the illustration.

Based on the stochastic strain-driven mapping equation (2), a stochastic linear elastic constitutive problem can be formulated as

1. (constitutive equation)  $\boldsymbol{\sigma} = \mathbb{C}(\underline{\kappa}(\omega, \underline{s})) : \boldsymbol{\varepsilon}(\underline{\kappa}(\omega, \underline{s})) \in \mathcal{M}$ ,
2. (stress constraint)  $\boldsymbol{\sigma} = \bar{\boldsymbol{\sigma}}(\omega, \underline{s}) \in \mathcal{M}_\sigma \subset \mathcal{M}$ , (3)
3. (strain constraint)  $\boldsymbol{\varepsilon} = \bar{\boldsymbol{\varepsilon}}(\omega, \underline{s}) \in \mathcal{M}_\varepsilon \subset \mathcal{M}$ ,

where

$$\underline{\kappa}(\omega, \underline{s}) = [\kappa_1(\omega, \underline{s}), \dots, \kappa_i(\omega, \underline{s}), \dots, \kappa_{n_m}(\omega, \underline{s})]^T \quad (4)$$

is the material parameter vector of  $n_m$  polymorphic uncertain material parameters. In addition, in (3)<sub>1</sub> the symmetric Cauchy stress tensor  $\boldsymbol{\sigma}$  and the polymorphic uncertain elasticity material tensor  $\mathbb{C}(\underline{\kappa}(\omega, \underline{s}))$  are used. Stress and strain constraints in (3)<sub>2</sub> and (3)<sub>3</sub> are formulated on the spaces  $\mathcal{M}_\sigma$  and  $\mathcal{M}_\varepsilon$ , where  $\mathcal{M}_\sigma \cup \mathcal{M}_\varepsilon = \mathcal{M}$  and  $\mathcal{M}_\sigma \cap \mathcal{M}_\varepsilon = \emptyset$  hold, and defined by prescribed stresses  $\bar{\boldsymbol{\sigma}}(\omega, \underline{s})$  and strains  $\bar{\boldsymbol{\varepsilon}}(\omega, \underline{s})$ , respectively. In the sequel, we assume that  $\underline{\kappa}(\omega, \underline{s})$  is the only uncertain input variable that depends on the aleatory elementary event  $\omega$  and on the design variables  $\underline{s}$ . We exploit a strain based method and formulate

*the stochastic state problem:*

for given  $\underline{s} \in \mathcal{S}$  and  $\omega \in \Omega$  find  $\boldsymbol{\varepsilon}(\underline{\kappa}(\omega, \underline{s}))$  such that

$$\mathbf{r}(\underline{\kappa}(\omega, \underline{s})) := \underbrace{\mathbb{C}(\underline{\kappa}(\omega, \underline{s})) : \boldsymbol{\varepsilon}(\underline{\kappa}(\omega, \underline{s}))}_{\boldsymbol{\sigma}(\boldsymbol{\varepsilon}(\underline{\kappa}(\omega, \underline{s})))} - \bar{\boldsymbol{\sigma}} = \mathbf{0}, \quad (5)$$

where  $\mathbf{r}(\underline{\kappa}(\omega, \underline{s}))$  has the interpretation of a stochastic residual for a strain-driven algorithm.

**2.2. Stochastic quantity of interest and target problem.** In the subsequent exposition we do not merely want to characterize the design properties of the random strain tensor  $\boldsymbol{\varepsilon}(\underline{\kappa}(\omega, \underline{s}))$  satisfying the stochastic state equation (5). Instead, we are more interested in the stochastic design analysis of a physical event or a feature of a structure that depends upon  $\boldsymbol{\varepsilon}$ , where quantities of interest (QoIs) are characterized by functionals  $Q(\boldsymbol{\varepsilon}(\underline{\kappa}(\omega, \underline{s})))$  of the solutions  $\boldsymbol{\varepsilon}(\underline{\kappa}(\omega, \underline{s}))$  to (5). A possible realization of the QoI is

$$Q(\boldsymbol{\varepsilon}(\underline{\kappa}(\omega, \underline{s}))) = \boldsymbol{\sigma}(\boldsymbol{\varepsilon}(\underline{\kappa}(\omega, \underline{s}))) : \boldsymbol{\sigma}(\boldsymbol{\varepsilon}(\underline{\kappa}(\omega, \underline{s}))). \quad (6)$$

Note that the QoI may be a stochastic random variable  $Q(\underline{\kappa}(\omega, \underline{s}))$  that depends on  $\omega$  and  $\underline{s}$ . Therefore, it is common to generate a relatively large number  $n_{MC}$  of samples  $Q_j(\underline{s})$ ,  $j = 1, \dots, n_{MC}$ , for  $Q(\underline{\kappa}(\omega, \underline{s}))$ , as, e.g., in the Monte Carlo (MC) simulation, based on its stochastic distribution described by a probability density function and to evaluate a QoI based on the computed results of all samples  $Q_j(\underline{s})$ ,  $j = 1, \dots, n_{MC}$ . From the received samples, different deterministic values can be computed to evaluate a so-called *surrogate QoI*  $Q^\omega$ . The upper index  $\omega$  indicates that  $Q^\omega$  is a surrogate QoI with respect to a QoI  $Q$ . Possible realizations for the surrogate QoI  $Q^\omega$  of the state problem in (5) are:

- expectation value (or sample mean)

$$Q^\omega = \mathbb{E}[Q(\boldsymbol{\varepsilon}(\underline{\kappa}(\omega, \underline{s})))] \approx \frac{1}{n_{MC}} \sum_{j=1}^{n_{MC}} Q_j, \quad (7)$$

- variance (or adjusted sample variance)

$$Q^\omega = \text{var}[Q(\boldsymbol{\varepsilon}(\underline{\kappa}(\omega, \underline{s})))] \approx \frac{1}{n_{MC} - 1} \sum_{j=1}^{n_{MC}} (Q_j - \mathbb{E}[Q])^2, \quad (8)$$

- square norm in  $L_2(\Omega, \Sigma, \mathbb{P})$  or second moment, also called stochastic norm [Le Maître and Knio 2010]

$$Q^\omega = \mathbb{E}[Q^2(\boldsymbol{\varepsilon}(\underline{\kappa}(\omega, \underline{s})))] \approx \frac{1}{n_{MC}} \sum_{j=1}^{n_{MC}} Q_j^2, \quad (9)$$

- functional dependencies of stochastic and design variables

$$Q^\omega = Q^\omega(\underline{\kappa}(\omega, \underline{s})), \quad (10)$$

whereby surrogate QoIs (7)–(9) are based on sample empirical moments. The adjusted sample variance in (8) refers to the fact that the sum of squared deviations is divided by  $n_{MC} - 1$  rather than by  $n_{MC}$ . With a specific choice of a surrogate

QoI  $Q^\omega$ , for example according to (7)–(10), we formulate

*the stochastic target problem:*

for given  $\underline{s} \in \mathcal{S}$  and  $\omega \in \Omega$  find  $z := Q^\omega(\underline{s}, \underline{\varepsilon}(\underline{\kappa}(\omega, \underline{s})))$ .

(11)

Note that, due to the dependency  $\underline{\varepsilon}(\underline{\kappa}(\omega, \underline{s}))$ , solution of the target problem in (11) involves solution of the state problem in (5).

**2.3. Discretization by polynomial chaos expansion.** As mentioned before in Section 2.2, the MC simulation, based on a relatively large number of samples, could be used for numerical evaluation of the QoI in (6). However, if only individual empirical moments in (7)–(9) are sought, a *discrete surrogate model*, e.g., in terms of the polynomial chaos expansion (PCE) [Ghanem and Spanos 1991; Caylak et al. 2018] can be used in order to reduce the numerical effort. This expansion involves a basis of known random functions with deterministic PC coefficients. Therefore, stochastic variables  $\underline{\kappa}(\omega, \underline{s})$  may be represented with the PCE

$$\underline{\kappa}(\omega, \underline{s}) \approx \sum_{l=0}^{n_P} \hat{\underline{\kappa}}_l(\underline{s}) \Psi_l(\underline{\theta}(\omega)) = \hat{\underline{\kappa}}_0(\underline{s}) + \sum_{l=1}^{n_P} \hat{\underline{\kappa}}_l(\underline{s}) \Psi_l(\underline{\theta}(\omega)), \quad (12)$$

where  $\hat{\underline{\kappa}}_l(\underline{s})$  are  $n_m \times 1$  PC coefficient vectors,  $n_P + 1$  is the number of the accompanying PC terms, and  $\Psi_l(\underline{\theta}(\omega))$  are PC basis functions described by multivariate single-index polynomials with uncorrelated standard distributed random variables  $\underline{\theta}$ .

In this paper Hermite polynomials with standard normal distributed random variables  $\underline{\theta} = [\theta_1, \dots, \theta_{n_m}]$  are chosen. Table 1 provides a single-index representation with a polynomial order  $p = 1$  for  $n_m = 5$  stochastic parameters. For a more detailed description, we refer to [Keese 2004]. The 0-th PC coefficient in (12) represents the expectation value  $\hat{\underline{\kappa}}_0(\underline{s}) = \mathbb{E}[\underline{\kappa}(\omega, \underline{s})]$ . With (12) the  $i$ -th material parameter

order $p$	$l$	$\Psi_l$
0	0	$\Psi_0 = 1$
1	1	$\Psi_1 = \theta_1$
	2	$\Psi_2 = \theta_2$
	3	$\Psi_3 = \theta_3$
	4	$\Psi_4 = \theta_4$
	5	$\Psi_5 = \theta_5$

**Table 1.** Single-index representation of the multivariate polynomials for  $n_m = 5$  stochastic parameters and polynomial order  $p = 1$ , which leads to  $n_P = 5$ .

can be expanded as

$$\kappa_i(\omega, \underline{s}) \approx \sum_{l=0}^{n_P} \hat{\kappa}_{il}(\underline{s}) \Psi_l(\underline{\theta}(\omega)) = \hat{\kappa}_{i0}(\underline{s}) + \sum_{l=1}^{n_P} \hat{\kappa}_{il}(\underline{s}) \Psi_l(\underline{\theta}(\omega)), \quad i=1, \dots, n_m. \quad (13)$$

Note that in the deterministic case of the  $i$ -th material parameter with  $n_P = 0$  and the independence on  $\underline{s}$ , (13) renders  $\kappa_i = \hat{\kappa}_{i0}$ . Similarly, a nonstochastic  $i$ -th material parameter with  $n_P = 0$  is given by  $\kappa_i(\underline{s}) = \hat{\kappa}_{i0}(\underline{s})$ .

Inserting (12) into the stochastic state problem of (5) and applying the Galerkin projection [Ghanem and Spanos 1991] renders

*the discrete stochastic state problem:*

for given  $\underline{s} \in \mathcal{S}$  and  $\omega \in \Omega$  find  $\hat{\mathbf{e}}_m(\underline{s}, \hat{\kappa})$  such that

$$\mathbf{r}_k(\underline{\kappa}(\omega, \underline{s})) := \sum_{l=0}^{n_P} \sum_{m=0}^{n_P} c_{klm}(\omega) \hat{\mathbb{C}}_l(\underline{s}, \hat{\kappa}) : \hat{\mathbf{e}}_m(\underline{s}, \hat{\kappa}) - \bar{\boldsymbol{\sigma}}_k = 0 \quad \text{for all } k \in \{0, \dots, n_P\}, \quad (14)$$

where

1.  $c_{klm}(\omega) = \mathbb{E}[\Psi_k \Psi_l \Psi_m]$ ,
2.  $\bar{\boldsymbol{\sigma}}_k = \mathbb{E}[\bar{\boldsymbol{\sigma}} \Psi_k]$ ,
3.  $\mathbf{r}_k(\underline{\kappa}(\omega, \underline{s})) = \mathbb{E}[\mathbf{r}(\underline{\kappa}(\omega, \underline{s})) \Psi_k]$ .

(15)

In (14)  $\hat{\kappa}(\underline{s})$  describes the  $n_m \times (n_P + 1)$  matrix of PC coefficients

$$\hat{\kappa}(\underline{s}) = [\hat{\kappa}_0(\underline{s}), \dots, \hat{\kappa}_{n_P}(\underline{s})] = \begin{bmatrix} \hat{\kappa}_{10}(\underline{s}) & \dots & \hat{\kappa}_{1n_P}(\underline{s}) \\ \vdots & \ddots & \vdots \\ \hat{\kappa}_{n_m0}(\underline{s}) & \dots & \hat{\kappa}_{n_m n_P}(\underline{s}) \end{bmatrix} \in \mathbb{R}^{n_m \times (n_P+1)}. \quad (16)$$

With the above preliminaries at hand, the PCE based discrete surrogate QoI  $Q^\omega$  for an arbitrary QoI  $Q$  can be formulated using the PCE in (12). The PCE based discrete QoI is

$$Q(\underline{\kappa}(\omega, \underline{s})) = \sum_{k=0}^{n_P} \hat{Q}_k(\underline{s}, \hat{\kappa}) \Psi_k(\underline{\theta}(\omega)), \quad (17)$$

where  $\hat{Q}_k(\underline{s}, \hat{\kappa})$  are the corresponding PC coefficients. For a specific case, inserting the QoI in (6) into the PC expanded QoI in (17) renders the PC coefficients as

$$\hat{Q}_k = \frac{1}{d_k} \sum_{l=0}^{n_P} \sum_{m=0}^{n_P} c_{klm} \hat{\sigma}_l \hat{\sigma}_m \quad \text{for all } k \in \{0, \dots, n_P\}, \quad (18)$$

where  $c_{klm}$  is given in (15)<sub>1</sub> and

$$d_k = c_{kk0} = \mathbb{E}[\Psi_k^2] \quad \text{for all } k \in \{0, \dots, n_P\}. \quad (19)$$

With the PCE based discrete QoI in (17) the discrete surrogate QoIs of (7)–(9) become

$$Q^\omega = \mathbb{E}[Q(\underline{\kappa}(\omega, \underline{s}))] = \widehat{Q}_0(\underline{s}, \widehat{\underline{\kappa}}), \quad (20)$$

$$Q^\omega = \text{var}[Q(\underline{\kappa}(\omega, \underline{s}))] = \sum_{k=1}^{n_P} d_k \widehat{Q}_k^2(\underline{s}, \widehat{\underline{\kappa}}), \quad (21)$$

$$Q^\omega = \mathbb{E}[Q^2(\underline{\kappa}(\omega, \underline{s}))] = \sum_{k=0}^{n_P} d_k \widehat{Q}_k^2(\underline{s}, \widehat{\underline{\kappa}}); \quad (22)$$

see, e.g., [Le Maître and Knio 2010]. In (20)–(22) it can be seen that the surrogate QoIs of random variables depend only on the design variables  $\underline{s}$  in (1), the deterministic PC coefficients  $\widehat{\underline{\kappa}}(\underline{s})$  in (16), and the expectation values in (19).

With a specific choice of a discrete surrogate QoI  $Q^\omega$ , for example according to (20)–(22), we formulate

*the discrete stochastic target problem:*

for given  $\underline{s} \in \mathcal{S}$  and  $\omega \in \Omega$  find  $z := Q^\omega(\underline{s}, \widehat{\underline{\kappa}}(\underline{s}, \widehat{\underline{\kappa}}), \underline{d})$ ,

(23)

where  $\widehat{\underline{\kappa}}(\underline{s}, \widehat{\underline{\kappa}}) = [\widehat{\kappa}_0(\underline{s}, \widehat{\underline{\kappa}}), \dots, \widehat{\kappa}_{n_P}(\underline{s}, \widehat{\underline{\kappa}})]^T$  and  $\underline{d} = [d_0, \dots, d_{n_P}]^T$ . Note that, due to the dependency  $\widehat{\underline{\kappa}}(\underline{s}, \widehat{\underline{\kappa}})$ , solution of the discrete target problem in (23) involves solution of the discrete state problem in (14).

**2.4. Example.** In order to demonstrate the concept of a surrogate QoI in linear isotropic elasticity we consider a uniaxial strain-driven loading case with  $\varepsilon = 0.1$ . Furthermore, a PC expanded Young's modulus  $E(\omega)$  is assumed as a normal distributed random variable according to (13) with  $n_m = 1$  and  $n_P = 1$ :

$$E(\omega) = \widehat{E}_0 + \widehat{E}_1 \theta(\omega) = 80 \text{ GPa} + 5 \text{ GPa } \theta(\omega). \quad (24)$$

In Figure 2, left, the distribution of the random variable in (24) is illustrated as a solid line, where in addition the histogram represents Young's modulus  $E(\omega)$  using  $n_{\text{MC}} = 10^8$  Monte Carlo samples. From the solution of the discrete stochastic state problem in (14), we obtain the stress random variable  $\sigma(\omega)$  as

$$\sigma(\omega) = \widehat{\sigma}_0 + \widehat{\sigma}_1 \theta(\omega) = \widehat{E}_0 \varepsilon + \widehat{E}_1 \varepsilon \theta(\omega) = 8 \text{ GPa} + 0.5 \text{ GPa } \theta(\omega). \quad (25)$$

The stress PC coefficients in (25) are used to calculate the QoI PC coefficients with  $n_P = 1$  according to (18), where  $c_{klm}$  and  $d_k$  in (15)<sub>1</sub> and (19), respectively, for

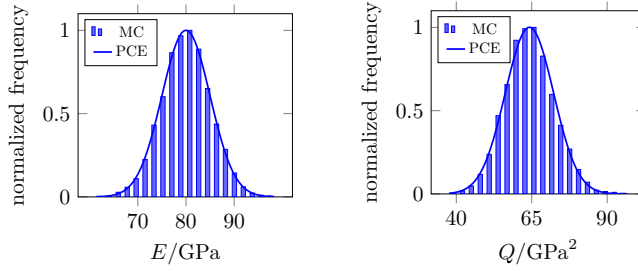


**Figure 2.** PCE and MC distribution of Young’s modulus  $E(\omega)$  (left) and QoI  $Q(\omega)$  (right) of (24) and (27), respectively.

$k$	$l$	$m$	$c_{klm}$	$d_k$
0	0	0	1	1
	0	1	0	
	1	0	0	
	1	1	1	
1	0	0	0	1
	0	1	1	
	1	0	1	
	1	1	0	

**Table 2.** Values of  $c_{klm}$  and  $d_k$  for a stochastic dimension  $n_m = 1$  and polynomial order  $p = 1$ , which leads to  $k, l, m = 0, \dots, 1$ .

$k, l, m = 0, 1$  are known by [Ghanem and Spanos 1991] according to Table 2. With the resulting PC coefficients

$$\widehat{Q}_0 = \hat{\sigma}_0^2 + \hat{\sigma}_1^2 = 64.25 \text{ GPa}^2, \quad \widehat{Q}_1 = 2\hat{\sigma}_0\hat{\sigma}_1 = 8 \text{ GPa}^2 \quad (26)$$

the PCE based QoI  $Q(\omega)$  in (17) becomes

$$Q(\omega) = \widehat{Q}_0 + \widehat{Q}_1\theta(\omega) = 64.25 \text{ GPa}^2 + 8 \text{ GPa}^2\theta(\omega). \quad (27)$$

In Figure 2, right, the distribution of the random variable in (27) is illustrated as a solid line, where in addition the histogram represents the QoI  $Q(\omega)$  obtained from  $n_{MC} = 10^8$  Monte Carlo samples.

Finally, results for surrogate QoIs using the PCE in (20)–(22) with  $n_P = 1$  and MC in (7)–(9) with  $n_{MC} = 10^4$  and  $n_{MC} = 10^8$  are summarized in Table 3. In addition to the quantitative values of three surrogate QoIs  $\mathbb{E}[Q]$ ,  $\text{var}[Q]$ , and  $\mathbb{E}[Q^2]$ , the corresponding computational times  $t_C$  are presented. It can be seen that the PCE based results are in good agreement with MC based results and show convergence

$Q^\omega$	MC ( $n_{MC} = 10^4$ )		MC ( $n_{MC} = 10^8$ )		PCE ( $n_p = 1$ )	
	$Q^\omega$	$t_C/\text{ms}$	$Q^\omega$	$t_C/\text{ms}$	$Q^\omega$	$t_C/\text{ms}$
$\mathbb{E}[Q]/\text{GPa}^2$	64.3062	0.375	64.2494	126.1	64.25	13.8
$\text{var}[Q]/\text{GPa}^4$	64.3729	0.841	64.1268	226.3	64	23.6
$\mathbb{E}[Q^2]/\text{GPa}^4$	4199.6	0.542	4192.1	218.1	4192.7	21.8

**Table 3.** Surrogate QoIs and computational times  $t_C$  for MC with  $n_{MC} = 10^4$ , MC with  $n_{MC} = 10^8$ , and PCE with  $n_p = 1$ .

after  $n_{MC} = 10^8$  realizations. The increase to  $n_{MC} = 10^9$ , which is not shown here, results in a similar behavior.

### 3. Hybrid fuzzy-stochastic analysis

**3.1. Fuzzy set and fuzzy number.** So far, the design space  $\mathcal{S} \subset \mathbb{R}^{n_s}$  in (1) has been assumed to be a precise set or a fundamental set of ordered pairs. However, in the case of a lack of knowledge also known as epistemic uncertainty, this is not realistic. Therefore, in the sequel, modeling of epistemic uncertainty is accounted for by the fuzzy analysis. To this end, the precise set  $\mathcal{S}$  in (1) is replaced by a nonprecise set, or fuzzy set [Möller and Beer 2004], respectively, of ordered pairs

1.  $\widehat{\mathcal{S}} = \{(\underline{s}, \mu_{\widehat{\mathcal{S}}}(\underline{s})) \mid \underline{s} \in \mathbb{R}^{n_s}, \mu_{\widehat{\mathcal{S}}}(\underline{s}) = \min_{i=1, \dots, n_s} \{\mu_{\mathcal{G}_i}(s_i)\}\},$
2.  $\widehat{\mathcal{G}}_i = \{(s_i, \mu_{\mathcal{G}_i}(s_i)) \mid s_i \in \mathbb{R}, \mu_{\mathcal{G}_i}(s_i) \in [0, 1]\},$  (28)
3.  $\mu_{\mathcal{G}_i} : \mathbb{R} \rightarrow [0, 1], \quad s_i \mapsto \mu_{\mathcal{G}_i}(s_i).$

According to (28)<sub>1</sub>  $\widehat{\mathcal{S}}$  comprises all combinations of the design variables  $s_1, \dots, s_{n_s}$  of the fuzzy sets  $\widehat{\mathcal{G}}_i$  in (28)<sub>2</sub>. The corresponding function  $\mu_{\mathcal{G}_i}(s_i)$  in (28)<sub>3</sub> describes the degree of membership of  $s_i \in \mathcal{G}_i \subset \mathbb{R}$  and therefore is called the membership function. In this work only normalized membership functions with the property  $\sup_{s_i \in \mathcal{G}_i} [\mu_{\mathcal{G}_i}(s_i)] = 1$  are considered. A triangular fuzzy number [Möller and Beer 2004]

$$\widehat{\mathcal{G}}_i = \langle s_i^L, s_i^M, s_i^R \rangle, \quad \text{where } s_i^L < s_i^M < s_i^R, \quad (29)$$

is a special case of a fuzzy set and is illustrated in Figure 3, left. The stochastic QoI  $Q(\underline{\kappa}(\omega, \underline{s}))$  in (6) becomes a function of the fuzzy design variables  $\underline{s}$  and can be treated as a hybrid fuzzy-stochastic function. In order to determine  $Q(\underline{\kappa}(\omega, \underline{s}))$ , we introduce a novel hybrid fuzzy-stochastic model based on the polynomial chaos expansion. In this way, the fuzzy-random material parameter vector  $\underline{\kappa}(\omega, \underline{s})$  in (4) propagates the fuzzy-random output variable  $Q(\underline{\kappa}(\omega, \underline{s}))$  in (6) or the fuzzy output variable  $Q^\omega(\underline{\kappa}(\omega, \underline{s}))$  in (7)–(10).

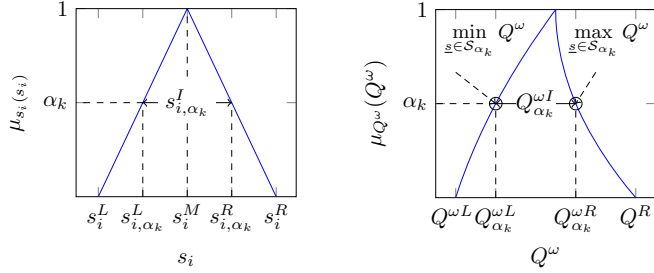


**Figure 3.** Schematic graph of fuzzy analysis with  $\alpha$ -level optimization from (left) design variable (triangular) to (right) QoI.

With  $\mathcal{S}$  in (1) replaced by  $\widehat{\mathcal{S}}$  in (28) the hybrid fuzzy-stochastic representation (4) for the input quantity  $\underline{\kappa}(\omega, \underline{s})$  of the state and target problem in (5) and (11) accounts for the most general case in which every single component  $\kappa_i(\omega, \underline{s})$  can be subjected to polymorphic uncertainty. Depending on the given uncertainty type of  $\underline{\kappa}(\omega, \underline{s})$  in (4), the following five scenarios of uncertainty analysis (of PCE based hybrid fuzzy-stochastic analysis) can be distinguished:

- deterministic analysis

$$\underline{\kappa} = \widehat{\underline{\kappa}} = \widehat{\underline{\kappa}}_0, \quad n_P = 0, \quad n_S = 0, \quad (30)$$

where each material parameter  $\kappa_i = \widehat{\kappa}_i = \widehat{\kappa}_{i0}, i = 1, \dots, n_m$ , is deterministic,

- stochastic analysis

$$\underline{\kappa} = \underline{\kappa}(\omega), \quad \kappa_i = \kappa_i(\omega), \quad n_P > 0, \quad n_S = 0, \quad \text{and deterministic } \widehat{\underline{\kappa}}, \quad (31)$$

where at least one material parameter is a random variable,

- fuzzy analysis

$$\underline{\kappa} = \underline{\kappa}(\underline{s}), \quad \kappa_i = \kappa_i(\underline{s}), \quad n_P = 0, \quad n_S > 0, \quad (32)$$

where at least one material parameter is a fuzzy variable,

- fuzzy-stochastic analysis

$$\underline{\kappa} = \underline{\kappa}(\omega, \underline{s}), \quad \kappa_i = \kappa_i(\omega), \quad \kappa_j = \kappa_j(\underline{s}), \quad n_P > 0, \quad n_S > 0, \quad (33)$$

where at least one material parameter is a random variable and one parameter is a fuzzy variable,

- hybrid fuzzy-stochastic analysis

$$\underline{\kappa} = \underline{\kappa}(\omega, \underline{s}), \quad \kappa_i = \kappa_i(\omega, \underline{s}), \quad n_P > 0, \quad n_S > 0, \quad (34)$$

where at least one material parameter is a (polymorphic uncertain) fuzzy-random variable.

We recall that in (30)–(34)  $n_s$  is the number of design variables of  $\underline{s}$  in (1),  $n_m$  is the number of material parameters of  $\underline{\kappa}(\omega, \underline{s})$  in (4), and  $n_P$  is the number of PC truncations in (12).

**3.2.  $\alpha$ -level discretization and optimization.** To avoid significant numerical effort the determination of a fuzzy output can be approximated by the so-called  $\alpha$ -level discretization, which represents fuzzy sets numerically by  $\alpha$ -cuts as

$$\mathcal{S}_{i,\alpha_k} = \{s_i \mid \mu_{\mathcal{S}_{i,\alpha_k}}(s_i) \geq \alpha_k, s_i \in \mathcal{S}_i\} = [s_{i,\alpha_k}^L, s_{i,\alpha_k}^R] := s_{i,\alpha_k}^I, \quad i = 1, \dots, n_s. \quad (35)$$

The  $\alpha$ -cuts are characterized by lower and upper bounds  $s_{i,\alpha_k}^L$  and  $s_{i,\alpha_k}^R$  and therefore define crisp intervals. Figure 3, left, illustrates the crisp interval  $s_{i,\alpha_k}^I$  and the membership function  $\mu_{\mathcal{S}_i}(\underline{s}_i)$  discretized by  $n_\alpha$   $\alpha$ -levels. In this context,  $0 \leq \alpha_k \leq 1$  denotes the membership level; see, e.g., [Möller and Beer 2004]. All fuzzy design variables  $s_i$  are discretized using the same  $\alpha$ -level structure, i.e., the number and the increments of  $\alpha$ -levels, to form the associated crisp sets. Therefore, intervals in (35) lead to an  $n_s$ -dimensional constrained design space

$$\mathcal{S}_{\alpha_k} = [\mathcal{S}_{1,\alpha_k} \times \dots \times \mathcal{S}_{i,\alpha_k} \times \dots \times \mathcal{S}_{n_s,\alpha_k}] \subset \mathcal{S} \subset \mathbb{R}^{n_s}. \quad (36)$$

The determination of the minimum and maximum values of the surrogate QoI in (11) or (23), respectively, at each  $\alpha$ -level requires the solutions of

*two hybrid fuzzy-stochastic  $\alpha$ -level optimization problems:*

1. find  $Q_{\alpha_k}^{\omega L} = \min_{\underline{s} \in \mathcal{S}_{\alpha_k}} Q^\omega(\underline{s}, \boldsymbol{\varepsilon}(\underline{\kappa}(\omega, \underline{s}))) \approx \min_{\underline{s} \in \mathcal{S}_{\alpha_k}} Q^\omega(\underline{s}, \hat{\boldsymbol{\varepsilon}}(\underline{s}, \hat{\boldsymbol{\kappa}}), \underline{d})$ ,
2. find  $Q_{\alpha_k}^{\omega R} = \max_{\underline{s} \in \mathcal{S}_{\alpha_k}} Q^\omega(\underline{s}, \boldsymbol{\varepsilon}(\underline{\kappa}(\omega, \underline{s}))) \approx \max_{\underline{s} \in \mathcal{S}_{\alpha_k}} Q^\omega(\underline{s}, \hat{\boldsymbol{\varepsilon}}(\underline{s}, \hat{\boldsymbol{\kappa}}), \underline{d})$ .

(37)

As visualized in Figure 3, right, the two extrema  $Q_{\alpha_k}^{\omega L}$  and  $Q_{\alpha_k}^{\omega R}$  render two points of the membership function  $\mu_Q(Q)$  for the membership level  $\alpha_k$ . The interval  $Q_{\alpha_k}^{\omega I} = [Q_{\alpha_k}^{\omega L}, Q_{\alpha_k}^{\omega R}]$  is fully described by the lower and upper bounds  $Q_{\alpha_k}^{\omega L}$  and  $Q_{\alpha_k}^{\omega R}$ . As no requirements are formulated for the continuous mapping model, both optimization problems in (37) involve only simple constraints. Problems of this kind are discussed in detail in [Bertsekas 1982].

**3.3. Numerical implementation.** In principle, fuzzy and stochastic dominated approaches with polymorphic uncertainties are conceivable [Reuter et al. 2012] for numerical determination of the target (11) or (23). The two approaches are illustrated in Figure 4, top and bottom. The difference between both approaches is the sequences of the evaluations of uncertainties.

For the fuzzy dominated approach, the stochastic analysis is performed inside the fuzzy analysis, which leads to  $\alpha$ -level optimization loops (sequence: fuzzy

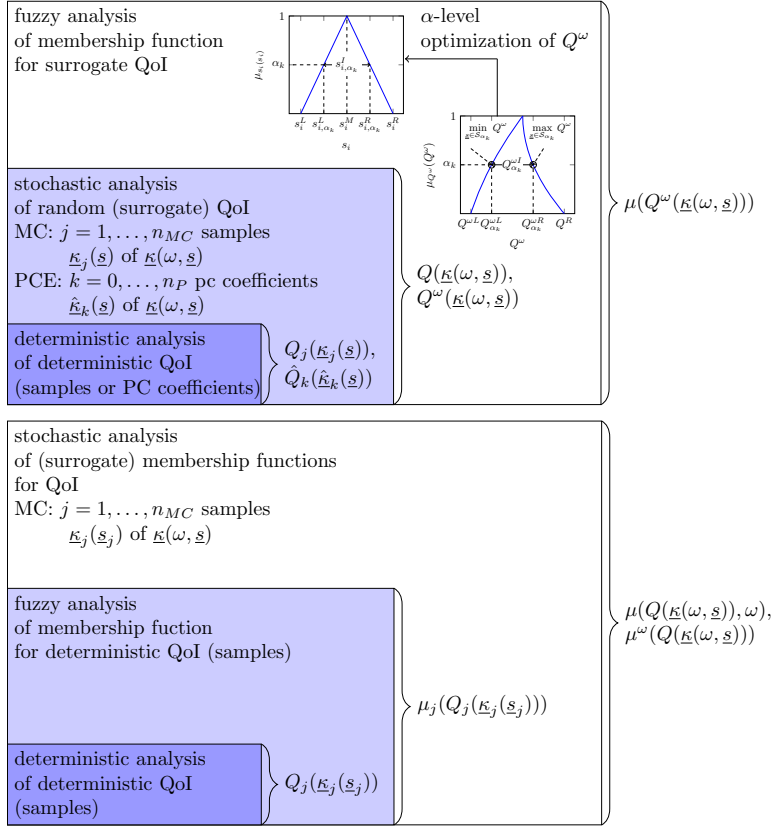


**Figure 4.** Computational scheme for the determination of QoIs with polymorphic uncertain parameters: (top) fuzzy dominated approach and (bottom) stochastic dominated approach.

analysis) (see (37)) with fuzzy-random variables  $\underline{\kappa}(\omega, \underline{s})$ . Within each iteration of the optimization loop a certain number  $n_{MC}$  of samples  $\underline{\kappa}_j(\underline{s})$  (e.g., MC method) or PC coefficients  $\hat{\underline{\kappa}}_k(\underline{s})$  (PCE method) are generated (sequence: stochastic analysis). Then, samples  $Q_j(\underline{s})$  or PC coefficients  $\hat{Q}_k(\underline{s})$  for a QoI  $Q(\underline{\kappa}(\omega, \underline{s}))$ , e.g., (6), are calculated (sequence: deterministic analysis). After that, surrogate QoIs in (7)–(10) or the discrete PCE based surrogate QoIs in (20)–(22) (sequence: stochastic analysis) are determined and used for the  $\alpha$ -level optimization (sequence: fuzzy analysis). Note, with a specific choice of a surrogate QoI, the  $\alpha$ -level optimization problems at each  $\alpha$ -level will be solved only once using the fuzzy dominated approach. The required design variables  $\underline{s}$  for the solution of the membership function for (surrogate) QoIs will be used for further calculation of, e.g., stresses or strains.

In contrast, the stochastic dominated approach, where the fuzzy analysis is performed inside the stochastic analysis, leads to a certain number  $n_{MC}$  (sequence:

stochastic analysis) of optimization loops (sequence: fuzzy analysis) with deterministic samples, e.g.,  $\underline{\kappa}_j$  of  $\underline{\kappa}(\omega)$  (sequence: deterministic analysis). The required design variables  $\underline{s}_j$  for the solution of the membership function for each QoI sample  $\mu_j(Q_j(\underline{\kappa}_j, \underline{s}_j))$  may be used for further calculation of interested quantity samples, e.g., samples of stresses or strains. After the fuzzy deterministic analysis, the outer stochastic analysis leads to stochastic distributions of membership functions  $\mu$  or to surrogate membership functions  $\mu^\omega$ , respectively.

In this paper, the hybrid fuzzy-stochastic analysis is performed by the PCE based surrogate model, which directly provides the calculation of the surrogate QoIs in (20)–(22) and the required design variables. Therefore, and due to the small number of optimizations loops, only one fuzzy optimization of the chosen surrogate QoI, fuzzy dominated approach is preferred. In contrast, in the stochastic dominated approach, the fuzzy optimization must be performed for all samples  $n_{MC}$ . The MC simulation, in the fuzzy dominated and also in the stochastic dominated approaches, is also performed for each example to verify the accuracy of the results, as well as the computational time.

#### 4. Experimental investigation of fiber reinforced plastics

In order to describe unidirectional fiber reinforced plastics (FRP), a transversely isotropic elasticity model is used, where the plane normal to the fiber direction can be considered as an isotropic plane. In Figure 5, the fibers are aligned with the 1-axis, which is normal to the 2-3-plane of isotropy.

In Voigt notation, the constitutive equation (3)<sub>1</sub> for transversely isotropic elasticity reads

1.  $\underline{\sigma} = \underline{C}\underline{\varepsilon}$ , where
2.  $\underline{\sigma} = [\sigma_{11}, \sigma_{22}, \sigma_{33}, \sigma_{12}, \sigma_{13}, \sigma_{23}]^T$ ,  $\underline{\varepsilon} = [\varepsilon_{11}, \varepsilon_{22}, \varepsilon_{33}, \gamma_{12}, \gamma_{13}, \gamma_{23}]^T$ ,
3. 
$$\underline{C} = \begin{bmatrix} C_{11} & 2\nu(\lambda + G_{\perp}) & 2\nu(\lambda + G_{\perp}) & 0 & 0 & 0 \\ & \lambda + 2G_{\perp} & \lambda & 0 & 0 & 0 \\ & & \lambda + 2G_{\perp} & 0 & 0 & 0 \\ & & & G_{\parallel} & 0 & 0 \\ \text{sym} & & & & G_{\parallel} & 0 \\ & & & & & G_{\perp} \end{bmatrix}, \quad (38)$$
4. 
$$C_{11} = \frac{E_{\parallel}^2(E_{\perp} - 4G_{\perp})}{4E_{\perp}G_{\perp}\nu^2 + E_{\parallel}E_{\perp} - 4E_{\parallel}G_{\perp}},$$
5. 
$$\lambda = -\frac{2G_{\perp}(2E_{\perp}G_{\perp}\nu^2 + E_{\parallel}E_{\perp} - 2E_{\parallel}G_{\perp})}{4E_{\perp}G_{\perp}\nu^2 + E_{\parallel}E_{\perp} - 4E_{\parallel}G_{\perp}}.$$

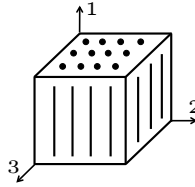


**Figure 5.** A transversely isotropic volume element, where fibers are aligned with the 1-axis.

In addition to the Voigt notation in (38)<sub>2</sub> of the stress tensor  $\sigma$ , the Mandel notation

$$\underline{\sigma}_M = [\sigma_{11}, \sigma_{22}, \sigma_{33}, \sqrt{2}\sigma_{12}, \sqrt{2}\sigma_{13}, \sqrt{2}\sigma_{23}]^T \tag{39}$$

is introduced, whereby (6) reads

$$Q(\underline{\varepsilon}(\underline{\kappa}(\omega, \underline{s}))) = \underline{\sigma}_M^T(\underline{\varepsilon}(\underline{\kappa}(\omega, \underline{s})))\underline{\sigma}_M(\underline{\varepsilon}(\underline{\kappa}(\omega, \underline{s}))). \tag{40}$$

In (38)  $\nu$  is the dimensionless Poisson ratio and  $E_{\parallel}$ ,  $E_{\perp}$  and  $G_{\parallel}$ ,  $G_{\perp}$  are Young’s moduli and shear moduli in fiber and transverse direction, respectively. According to (4), the  $n_m = 5$  required transversely isotropic material parameters are summarized in the material parameter vector

$$\underline{\kappa} = [\kappa_1, \kappa_2, \kappa_3, \kappa_4, \kappa_5]^T = [E_{\parallel}, E_{\perp}, G_{\parallel}, G_{\perp}, \nu]^T. \tag{41}$$

The determination of the shear modulus  $G_{\perp}$  in the isotropic plane requires a shear test apparatus, which currently is not available. Instead only tensile tests can be performed, which are used to determine the material parameters in (41), except  $G_{\perp}$ , experimentally.

To this end, three plates made of unidirectional FRP with different fiber orientations ( $0^\circ$ ,  $45^\circ$ ,  $90^\circ$ ) were produced. From each plate 30 tensile specimens were cut out. The geometry of the tensile specimen is depicted in Figure 6b. The width  $b_0$  and the thickness  $t_0$  of the specimens differ from  $0^\circ$  orientation to  $45^\circ$  and  $90^\circ$  orientation, where the dimensions for the different fiber orientations are summarized in Table 4. Furthermore, Figure 6c–e shows schematically the different fiber orientations of the specimens. These are clamped into a tensile testing machine with hydraulic clamping jaws as illustrated in the experimental setup in Figure 6a. The FRP is subjected to an off-axis uniaxial stress loading, in which the fibers are oriented in the 1-direction, and rotated around the 3-direction by an angle  $\varphi$ . With respect to the testing machine a machine-fixed coordinate system  $(x, y)$  in Figure 6 is defined. The experiments, which are displacement controlled according to DIN EN ISO 527-5, are loaded in the longitudinal direction  $x$  at an angle  $\varphi$  with respect to the fiber direction. In particular,  $\varphi = 0^\circ$  and  $\varphi = 90^\circ$  correspond to longitudinal and transverse uniaxial stress loading, respectively. A load cell supplies forces  $\bar{F}$

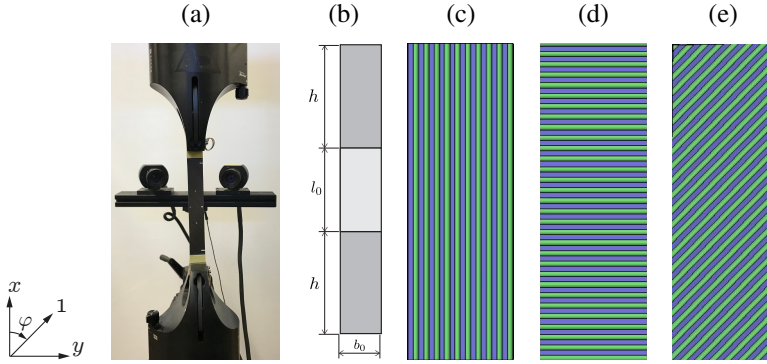


**Figure 6.** Experimental investigation: (a) experimental setup, (b) geometry of specimens, and schematic specimens for fiber orientation (c)  $0^\circ$ , (d)  $90^\circ$ , and (e)  $45^\circ$ . Machine-fixed coordinate system  $(x, y)$  and fibers aligned to 1-axis.

[mm]	$0^\circ$	$45^\circ/90^\circ$
length $l_0$	150	150
clamping length $h$	50	50
width $b_0$	15	25
thickness $t_0$	1	2

**Table 4.** Measures of specimens depending on fiber orientations.

at different observation states, whereby corresponding stresses in longitudinal direction  $\bar{\sigma}_x = \bar{F}/A_0$  are determined using the cross-sectional area  $A_0 = b_0 t_0$ ; see Table 4. By applying a video extensometer, the strains in longitudinal and transverse directions  $\bar{\varepsilon}_x$  and  $\bar{\varepsilon}_y$  are measured.

*Fiber orientation  $\varphi = 0^\circ$ .* In order to determine the Young’s modulus  $E_{\parallel}$  in fiber direction as well as the Poisson’s ratio  $\nu$ , tensile tests are applied for samples illustrated in Figure 6c. DIN EN ISO 527-1 provides further information regarding the test procedure and the data evaluation. The resulting curves for stress  $\sigma_{11} = \bar{\sigma}_x$  versus strain  $\varepsilon_{11} = \bar{\varepsilon}_x$  for 30 experiments are shown in Figure 7, left, where the slope of each curve describes the corresponding Young’s modulus  $E_{\parallel} = \Delta\sigma_{11}/\Delta\varepsilon_{11}$  in fiber direction. Furthermore, in Figure 7, right, experimental longitudinal strain  $\varepsilon_{11}$  versus transversal strain  $|\varepsilon_{22}| = |\bar{\varepsilon}_y|$  curves are illustrated, where the slope of each regression line for each curve renders the corresponding Poisson’s ratio  $\nu = -\Delta\varepsilon_{22}/\Delta\varepsilon_{11}$ . The frequency distributions of  $E_{\parallel}$  and  $\nu$  are illustrated in Figure 8, left and right.

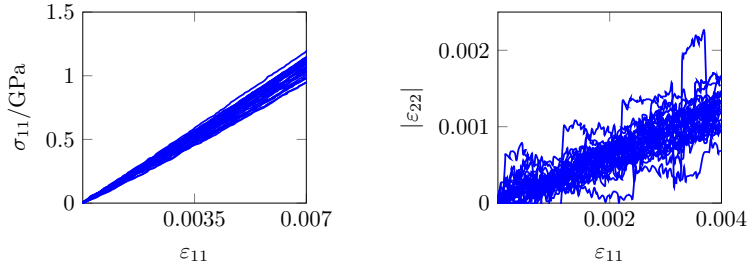


**Figure 7.** Experimental results for fiber orientation  $0^\circ$ : (left) longitudinal stress  $\sigma_{11}$  versus longitudinal strain  $\epsilon_{11}$  curves and (right) longitudinal strain  $\epsilon_{11}$  versus transversal absolute strain  $|\epsilon_{22}|$  curves.

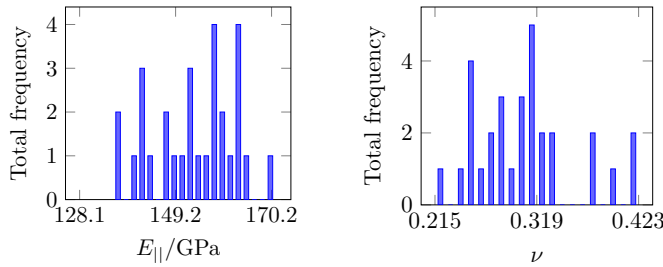


**Figure 8.** Frequency distributions of identified parameters for fiber orientation  $0^\circ$ : (left) Young's modulus in fiber direction  $E_{\parallel}$  and (right) Poisson's ratio  $\nu$ .

*Fiber orientation  $\varphi = 90^\circ$ .* To determine the Young's modulus  $E_{\perp}$  transverse to the fiber direction, tensile tests are applied for samples illustrated in Figure 6d. DIN EN ISO 527-1 provides further information regarding the test procedure and the data evaluation. Results for 30 experimental stress  $\sigma_{22} = \bar{\sigma}_x$  versus strain  $\epsilon_{22} = \bar{\epsilon}_x$  curves are illustrated in Figure 9, left, where the slope of each curve renders the corresponding Young's modulus  $E_{\perp} = \Delta\sigma_{22}/\Delta\epsilon_{22}$ . The frequency distribution of  $E_{\perp}$  is illustrated in Figure 9, right.

*Fiber orientation  $\varphi = 45^\circ$ .* In order to determine the shear modulus  $G_{\parallel}$  in fiber direction, tensile tests according to DIN EN ISO 527-5 are applied for samples illustrated in Figure 6e. Results for 30 experimental maximal shear stress  $\sigma_{12} = \bar{\sigma}_x/2$  versus shear strain  $\gamma_{12} \approx \bar{\epsilon}_x - \bar{\epsilon}_y$ , according to DIN EN ISO 14129, are illustrated in Figure 10, left, where the slope of each regression line for each curve renders the corresponding shear modulus  $G_{\parallel} = \Delta\sigma_{12}/\Delta\gamma_{12}$ . The frequency distribution of  $jG_{\parallel}$  is illustrated in Figure 10, right.

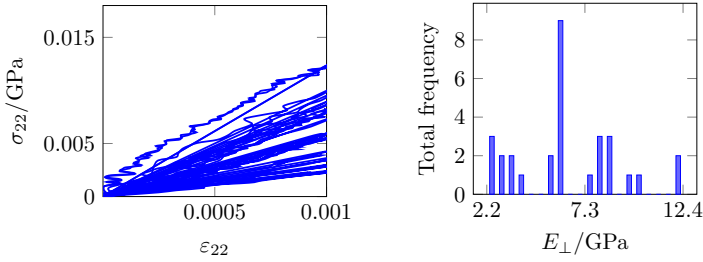


**Figure 9.** Experimental results and identification for fiber orientation  $90^\circ$ : (left) curves for stress  $\sigma_{22}$  transversal to fiber versus strain  $\epsilon_{22}$  transversal to fiber and (right) frequency distribution of Young’s modulus in transverse direction  $E_{\perp}$ .

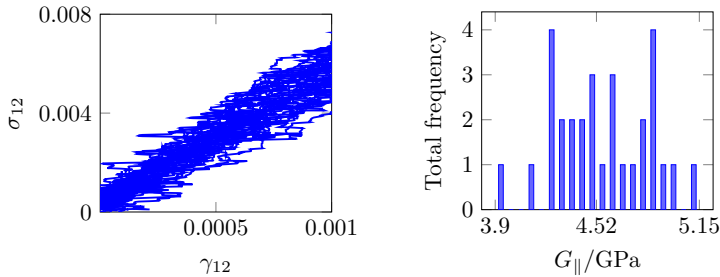


**Figure 10.** Experimental results and identification for fiber orientation  $45^\circ$ : (left) maximal shear stress  $\sigma_{12}$  versus maximal shear strain  $\gamma_{12}$  curves and (right) frequency distribution of shear modulus in fiber direction  $G_{\parallel}$ .

### 5. Representative numerical examples

For the following strain controlled examples, fuzzy analysis, fuzzy-stochastic analysis, and hybrid fuzzy-stochastic analysis, the strain vector is given as

$$\underline{\varepsilon} = [\varepsilon_{11}, \varepsilon_{22}, \varepsilon_{33}, \gamma_{12}, \gamma_{13}, \gamma_{23}]^T = [0.05, 0.02, 0.03, 0.005, 0.004, 0.002]^T. \quad (42)$$

As mentioned in Section 4, we are currently not able to determine the shear modulus in the isotropic plane. Therefore,  $G_{\perp} = 3.9286$  GPa is taken from the literature according to [Soden et al. 1998] and is regarded as deterministic.

**5.1. Fuzzy analysis.** In the first representative example, all material parameters except  $G_{\perp}$  in (41) are assumed as purely epistemic uncertain. Since  $G_{\perp}$  is deterministic it can be considered as a degenerated fuzzy variable in Figure 11e. The (fuzzy) input according to (32) includes no (stochastic) random variables and is

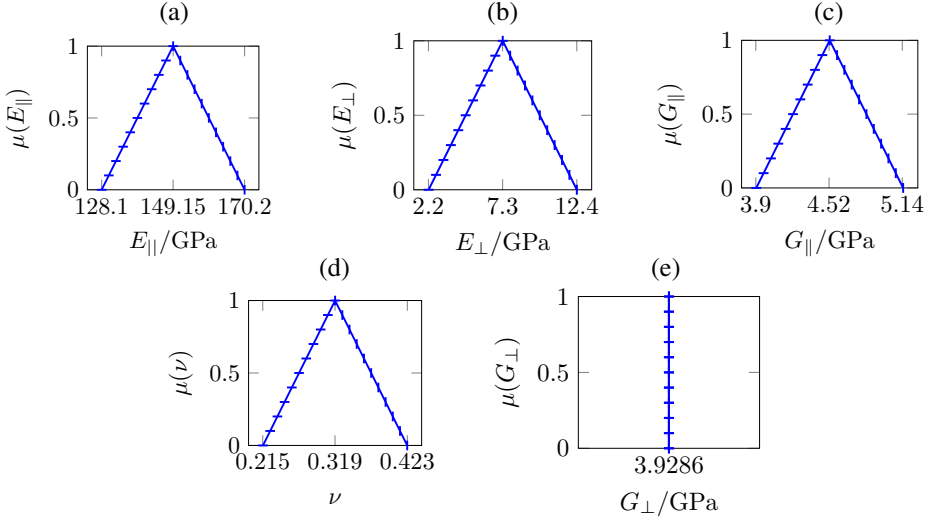


**Figure 11.** Fuzzy analysis: input membership functions for material design variables (a)  $E_{\parallel}$ , (b)  $E_{\perp}$ , (c)  $G_{\parallel}$ , (d)  $\nu$ , and (e)  $G_{\perp}$ .

defined as

$$\underline{\kappa}(\underline{s}) = [E_{\parallel}(\underline{s}), E_{\perp}(\underline{s}), G_{\parallel}(\underline{s}), G_{\perp}, \nu(\underline{s})]^T = [s_1, s_2, s_3, G_{\perp}, s_4]^T, \quad (43)$$

such that the vector in (1) of  $n_s = 4$  design variables for  $n_m = 5$  material parameters is given by

$$\underline{s} = [s_1, s_2, s_3, s_4]^T = [E_{\parallel}, E_{\perp}, G_{\parallel}, \nu]^T. \quad (44)$$

In the special case of fuzzy analysis according to (32), the matrix of PC coefficients in (16) reduces with  $n_p = 0$  to a vector corresponding to the material parameter vector in (43)

$$\hat{\underline{\kappa}}(\underline{s}) = \hat{\underline{\kappa}}_0(\underline{s}) = \underline{\kappa}(\underline{s}). \quad (45)$$

As discussed in [Möller and Beer 2004] several possible membership functions can be laid over the frequency distributions. This may depend, e.g., on the available data. Since there are no experimental results available for validation in the current work, we decided to use simple triangular shape functions by normalizing the memberships. Based on the identified parameters represented as frequency distributions in Figures 8; 9, right; and 10, right; membership functions  $\mu(\underline{s})$  are generated for the input quantities  $E_{\parallel}$ ,  $E_{\perp}$ ,  $G_{\parallel}$ , and  $\nu$  according to Figure 11a–d. To this end, the empirical mean  $\mathbb{E}[s_i^*]$  of the identified parameter samples  $s_i^*$  are chosen as mean values  $s_i^M$  to obtain triangular fuzzy numbers according to (29) as

$$\hat{\mathcal{P}}_i = \langle s_i^L, s_i^M, s_i^R \rangle = \langle \mathbb{E}[s_i^*] - f_i^*, \mathbb{E}[s_i^*], \mathbb{E}[s_i^*] + f_i^* \rangle, \quad (46)$$

where  $f_i^* = \max\{\mathbb{E}[s_i^*] - \min s_i^*, \max s_i^* - \mathbb{E}[s_i^*]\}$ , that is, for each material parameter a maximum deviation of  $f_i^*$  for the epistemic uncertainty is assumed. Thus, the triangular fuzzy numbers

$$\begin{aligned}
 1. \quad & \widehat{\mathcal{P}}_1 = \langle 128.1, 149.15, 170.2 \rangle \text{ GPa}, & f_1^* &= 21.05 \text{ GPa}, \\
 2. \quad & \widehat{\mathcal{P}}_2 = \langle 2.2, 7.3, 12.4 \rangle \text{ GPa}, & f_2^* &= 5.1 \text{ GPa}, \\
 3. \quad & \widehat{\mathcal{P}}_3 = \langle 3.9, 4.52, 5.14 \rangle \text{ GPa}, & f_3^* &= 0.62 \text{ GPa}, \\
 4. \quad & \widehat{\mathcal{P}}_4 = \langle 0.215, 0.319, 0.423 \rangle, & f_4^* &= 0.104
 \end{aligned} \tag{47}$$

are chosen for the four design variables in (44). The  $\alpha$ -discretization is performed with  $n_\alpha = 11$  cuts. These discrete input parameters define the stresses in (38) and the QoI in (40). Note that the QoI  $Q(\underline{s})$  in (40) in the purely (epistemic) fuzzy analysis is independent on  $\omega$  such that no surrogate QoIs are needed. The minimization and maximization problems in (37)<sub>1</sub> and (37)<sub>2</sub> are solved for  $Q(\underline{s})$  in (40) at each  $\alpha$ -level using a standard optimization tool for constrained functions. In this work the function `fmincon` with the sequential quadratic programming [Nocedal and Wright 1999] algorithm of the Matlab Optimization Toolbox is applied.

In Figure 12, the resulting output membership function of the optimization problems in (37) for the QoI  $Q(\underline{s})$  presented in (40) is illustrated. The marks  $-$  and  $|$  show that from each pair of interval bounds of the design variables  $s_{i,\alpha_k}^L$  and  $s_{i,\alpha_k}^R$  at each  $\alpha$ -level  $\alpha_k, k = 1, \dots, 11$ , in Figure 11a,d, the interval bounds of the QoIs  $Q_{\alpha_k}^{\omega L}$  and  $Q_{\alpha_k}^{\omega R}$  are obtained. Therefore, calculating the stresses  $\underline{\sigma}(\omega, \underline{s})$  in (38), the left and right interval bounds  $s_{i,\alpha_k}^L$  and  $s_{i,\alpha_k}^R$  at each  $\alpha$ -level  $\alpha_k, k = 1, \dots, 11$ , can be used.

The uncertain stress coefficients  $\sigma_{ij}$  of the stress vector  $\underline{\sigma}$  in (38) are illustrated in Figure 13. Due to Hooke’s law described in (38) the normal stress coefficients  $\sigma_{ii}(\underline{s})$  are effected by the design variables  $\underline{s} = [E_{\parallel}, E_{\perp}, G_{\parallel}, \nu]^T$  and the fixed material parameter  $G_{\perp}$ . Remarkably, the membership functions for the normal stress coefficients  $\sigma_{ii}(\underline{s})$  in Figure 13a–c become nonlinear. This is due to the nonlinear mathematical operations of fuzzy variables for the calculation of  $C_{11}$  and  $\lambda$  in (38).

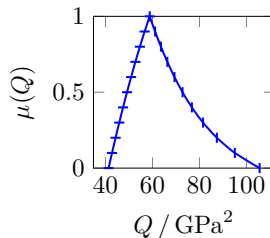


**Figure 12.** Fuzzy analysis: output membership function for quantity of interest  $Q(\underline{\varepsilon}(\underline{s}))$  in (40).

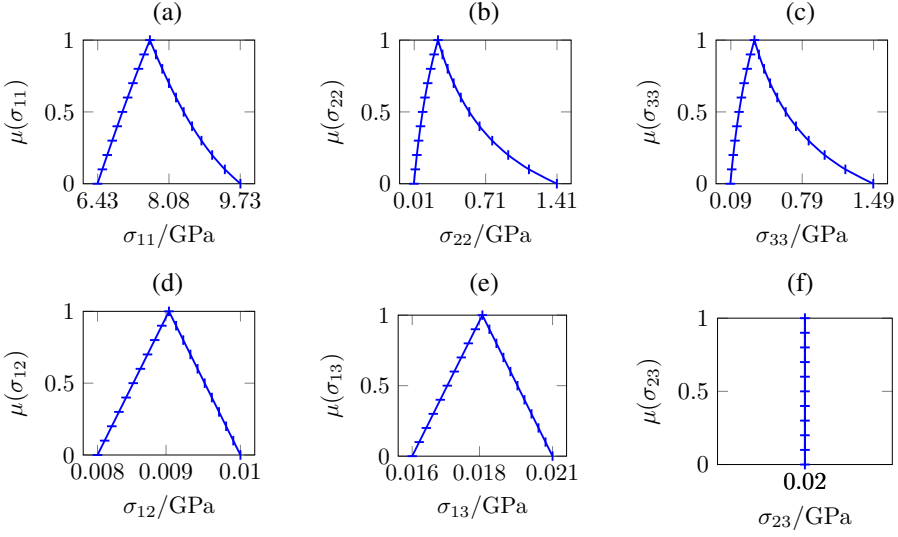


**Figure 13.** Fuzzy analysis: output membership functions for stresses (a)  $\sigma_{11}$ , (b)  $\sigma_{22}$ , (c)  $\sigma_{33}$ , (d)  $\sigma_{12}$ , (e)  $\sigma_{13}$ , and (f)  $\sigma_{23}$ .

The stress components  $\sigma_{12}(\underline{s})$  and  $\sigma_{13}(\underline{s})$  are only effected by the design variables  $G_{\parallel}(\underline{s})$ . Therefore, the membership functions  $\mu(\sigma_{12})$  and  $\mu(\sigma_{13})$  in Figure 13d–e have the same triangular shape as the membership function  $\mu(G_{\parallel})$  of the design variable  $G_{\parallel}$  in Figure 11c. The shear stress  $\sigma_{23}$  depends on the deterministic parameter  $G_{\perp}$ . Therefore, The membership function  $\mu(\sigma_{23})$  in Figure 13f becomes deterministic and is represented by a straight vertical line.

**5.2. Fuzzy-stochastic analysis.** From an industrial point of view, the mechanical properties in the fiber direction are of great interest. Therefore, in practice more experimental investigations are carried out in the fiber direction than in the transverse direction. Consequently, in the second representative example, two material parameters  $E_{\parallel}(\omega)$  and  $\nu(\omega)$  of the input vector in (41) are assumed as purely aleatoric, whereas  $E_{\perp}(\underline{s})$ ,  $G_{\parallel}(\underline{s})$ , and  $G_{\perp} = 3.9286$  GPa remain epistemic and deterministic as in Section 5.1. For a fuzzy-stochastic analysis the input material parameter vector (41) according to (33) is defined as

$$\underline{\kappa}(\omega, \underline{s}) = [E_{\parallel}(\omega), E_{\perp}(\underline{s}), G_{\parallel}(\underline{s}), G_{\perp}, \nu(\omega)]^T, \quad (48)$$

such that the design variable vector (1) of material parameters is given by

$$\underline{s} = [s_1, s_2]^T = [E_{\perp}, G_{\parallel}]^T. \quad (49)$$

The stochastic parameters  $E_{\parallel}(\omega)$  and  $\nu(\omega)$  are assumed to be normally distributed random variables, which requires a truncation of  $n_P = 2$  in (12). The membership

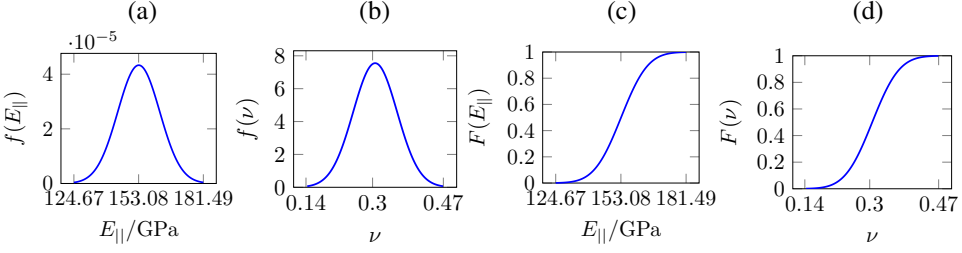


**Figure 14.** Fuzzy-stochastic analysis: input density functions for the aleatory material parameters (a) PDF for  $E_{\parallel}$ , (b) PDF for  $\nu$ , (c) CDF for  $E_{\parallel}$ , and (d) CDF for  $\nu$ .

functions  $\mu(\underline{s})$  for the material parameters  $E_{\perp}$  and  $G_{\parallel}$  remain unchanged according to Figure 11a,d and used as input quantities for the fuzzy analysis. Based on the frequency distributions in Figure 8 normally distributed density functions are generated from the expectation values  $\mathbb{E}[E_{\parallel}(\omega)]$ ,  $\mathbb{E}[\nu(\omega)]$  and standard deviations  $\text{std}[E_{\parallel}(\omega)]$ ,  $\text{std}[\nu(\omega)]$  for material parameters  $E_{\parallel}(\omega)$ ,  $\nu(\omega)$ , which are used as input quantities for the stochastic sequence in the fuzzy-stochastic analysis. In Figure 14 the corresponding probability density functions (PDFs) and cumulative density functions (CDFs) are given. According to (13), the PCEs for the normally distributed random variables  $E_{\parallel}(\omega)$  and  $\nu(\omega)$  for  $n_p = 2$  are

$$\begin{aligned} E_{\parallel}(\omega) &= \widehat{E}_{\parallel 0} + \widehat{E}_{\parallel 1}\theta_1(\omega) + \widehat{E}_{\parallel 2}\theta_2(\omega), \\ \nu(\omega) &= \widehat{\nu}_0 + \widehat{\nu}_1\theta_1(\omega) + \widehat{\nu}_2\theta_2(\omega). \end{aligned} \quad (50)$$

We assume, further, that  $E_{\parallel}(\omega)$  and  $\nu(\omega)$  are independent random variables such that (50) renders

$$\begin{aligned} E_{\parallel}(\omega) &= \widehat{E}_{\parallel 0} + \widehat{E}_{\parallel 1}\theta_1(\omega), \\ \nu(\omega) &= \widehat{\nu}_0 + \widehat{\nu}_2\theta_2(\omega), \end{aligned} \quad (51)$$

with PC coefficients

$$\begin{aligned} \widehat{E}_{\parallel 0} &= \mathbb{E}[E_{\parallel}] = 153.145, & \widehat{E}_{\parallel 1} &= \text{std}[E_{\parallel}] = 9.214, \\ \widehat{\nu}_0 &= \mathbb{E}[\nu] = 0.306, & \widehat{\nu}_2 &= \text{std}[\nu] = 0.0528. \end{aligned} \quad (52)$$

Consequently, the corresponding input matrix in (16) of material parameter PC coefficients becomes

$$\widehat{\underline{k}}(\underline{s}) = \begin{bmatrix} \widehat{E}_{\parallel 0} & \widehat{E}_{\parallel 1} & 0 \\ E_{\perp}(\underline{s}) & 0 & 0 \\ G_{\parallel}(\underline{s}) & 0 & 0 \\ G_{\perp} & 0 & 0 \\ \widehat{\nu}_0 & 0 & \widehat{\nu}_2 \end{bmatrix} = \begin{bmatrix} 153.145 & 9.214 & 0 \\ s_1 & 0 & 0 \\ s_2 & 0 & 0 \\ 3.9286 & 0 & 0 \\ 0.306 & 0 & 0.0528 \end{bmatrix}. \quad (53)$$

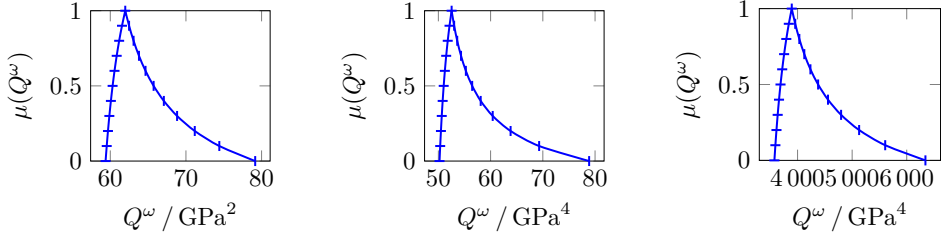


**Figure 15.** Fuzzy-stochastic analysis: membership function for surrogate QoIs in (20)–(22) according to QoI in (40), (left)  $Q^\omega = \mathbb{E}[Q]$ , (center)  $Q^\omega = \text{var}[Q]$ , and (right)  $Q^\omega = \mathbb{E}[Q^2]$ .

As mentioned in Section 3.3, both analyses, the fuzzy and the stochastic ones, are combined with the fuzzy dominated or stochastic dominated approach as illustrated in the computational scheme in Figure 4. Here, the focus is on the PCE based fuzzy dominated approach, in which the PC coefficients in (53), although only the 0-th, are represented as fuzzy design variables. Since the QoI in (40) will be a fuzzy-random variable, it is necessary to choose a surrogate QoI to perform the outer fuzzy optimization introduced in Figure 4, left (sequence: fuzzy analysis).

In Figure 15, the resulting output membership functions of the optimization problems in (37) for three possible realizations of surrogate QoIs presented in (20)–(22) are illustrated. The marks – and | show that from each pair of interval bounds of the design variables  $s_{i,\alpha_k}^L$  and  $s_{i,\alpha_k}^R$  at each  $\alpha$ -level  $\alpha_k$ ,  $k = 1, \dots, 11$ , in Figure 11b–c, the interval bounds of the surrogate QoIs  $Q_{\alpha_k}^{\omega L}$  and  $Q_{\alpha_k}^{\omega R}$  are obtained. Therefore, for postprocessing, e.g., calculating the stresses  $\underline{\sigma}(\omega, \underline{s})$  in (38), the left and right interval bounds  $s_{i,\alpha_k}^L$  and  $s_{i,\alpha_k}^R$  at each  $\alpha$ -level  $\alpha_k$ ,  $k = 1, \dots, 11$ , can be used.

In the fuzzy dominated approach as presented in Figure 4, left, for verification, the MC method with  $n_{\text{MC}} = 10^4$  Monte Carlo samples renders similar values. Results for surrogate QoIs using the PCE in (20)–(22) with  $n_p = 2$  and MC in (7)–(9) with  $n_{\text{MC}} = 10^3$  and  $n_{\text{MC}} = 10^4$  are summarized in Table 5. In addition to the quantitative values of the three surrogate QoIs  $\mathbb{E}[Q]$ ,  $\text{var}[Q]$ , and  $\mathbb{E}[Q^2]$ , the computational times  $t_C$  are presented. It can be seen that in the MC solution, even with a small number of samples, the computational effort is considerably greater than with the PCE solution, although the deviations are not negligible.

Due to the Hooke’s law (38) the stress components  $\sigma_{12}(\underline{s})$  and  $\sigma_{13}(\underline{s})$  are only effected by the design variables  $G_{\parallel}(\underline{s})$ , where  $\sigma_{23}$  depends on the deterministic parameter  $G_{\perp}$ . Consequently,  $\sigma_{12}$ ,  $\sigma_{13}$ , and  $\sigma_{23}$  remain unchanged compared to the results in Figure 13d–f of the fuzzy analysis in Section 5.1. However, by (38) the normal stresses  $\sigma_{ii}(\omega, \underline{s})$ ,  $i = 1, 2, 3$ , are effected by design variables  $E_{\perp}(\underline{s})$ ,  $G_{\parallel}(\underline{s})$  and stochastic variables  $E_{\parallel}(\omega)$ ,  $\nu(\omega)$ . Therefore,  $\sigma_{ii}(\omega, \underline{s})$  become

$Q^\omega$	$\alpha_k$	MC ( $n_{MC} = 10^3$ )			MC ( $n_{MC} = 10^4$ )			PCE ( $n_p = 2$ )		
		$Q_{\alpha_k}^{\omega L}$	$Q_{\alpha_k}^{\omega R}$	$t_C/s$	$Q_{\alpha_k}^{\omega L}$	$Q_{\alpha_k}^{\omega R}$	$t_C/s$	$Q_{\alpha_k}^{\omega L}$	$Q_{\alpha_k}^{\omega R}$	$t_C/s$
$\frac{\mathbb{E}[Q]}{\text{GPa}^2}$	1	62.10	62.10		61.31	61.31		61.98	61.98	
	0.5	60.57	65.36	192	60.17	64.97	1916	60.31	65.73	3.7
	0	59.69	76.16		59.29	75.81		59.38	79.16	
$\frac{\text{var}[Q]}{\text{GPa}^4}$	1	58.37	58.37		53.38	53.38		52.54	52.54	
	0.5	56.23	63.46	218	51.85	51.85	2011	51.02	56.47	3.8
	0	55.07	86.95		51.03	76.71		50.22	78.87	
$\frac{\mathbb{E}[Q^2]}{\text{GPa}^4}$	1	3856	3856		3864	3864		3894	3894	
	0.5	3667	4277	110	3675	4282	1071	3688	4377	3.5
	0	3560	5833		3569	5826		3576	6343	

**Table 5.** Surrogate QoIs and computational times  $t_C$  using MC with  $n_{MC} = 10^3$ , MC with  $n_{MC} = 10^4$  and PCE with  $n_p = 2$ .

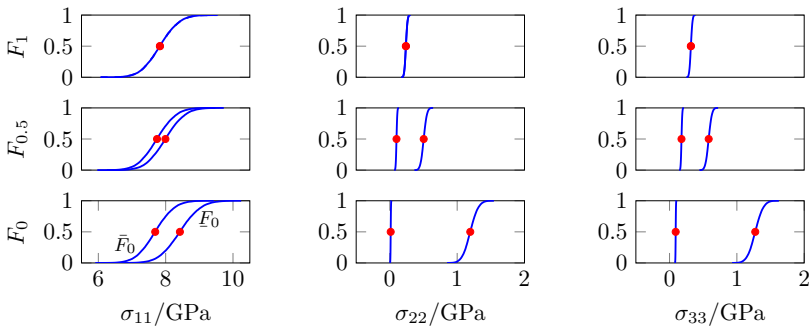


**Figure 16.** Fuzzy-stochastic analysis: P-boxes at  $\alpha$ -levels  $\alpha_1 = 0$ ,  $\alpha_6 = 0.5$  and  $\alpha_{11} = 1$  for normal stresses (left)  $\sigma_{11}$ , (center)  $\sigma_{22}$ , and (right)  $\sigma_{33}$ .

hybrid fuzzy-stochastic variables, which can be seen in Figure 16, i.e., the CDFs of  $\sigma_{ii}(\omega, \underline{s})$  are not anymore given by a unique CDF as for a stochastic variable, e.g., in Figure 14c–d. Instead, they are given by left upper bounds  $\bar{F}_{\alpha_k}(\sigma_{ii})$  and right lower bounds  $\underline{F}_{\alpha_k}(\sigma_{ii})$  at each  $\alpha$ -level, where the intervals of CDFs  $[\bar{F}_{\alpha_k}(\sigma_{ii}), \underline{F}_{\alpha_k}(\sigma_{ii})]$  are called probability boxes (P-boxes). For further explanation on P-boxes the reader is referred to [Ferson et al. 2003]. The P-boxes of the normal stresses  $\sigma_{ii}$  at three  $\alpha$ -levels 0, 0.5, and 1 are shown in Figure 16.

In addition, different statistical moments of the fuzzy-stochastic variables  $\sigma_{ii}$  can be calculated. The expectation values  $\mathbb{E}[\sigma_{ii}]$  and variances  $\text{var}[\sigma_{ii}]$  are illustrated in Figures 17 and 18. While, as shown in Figure 16,  $\sigma_{ii}$  are fuzzy-stochastic random variables, their moments in Figures 17 and 18 are fuzzy variables. The red dots in

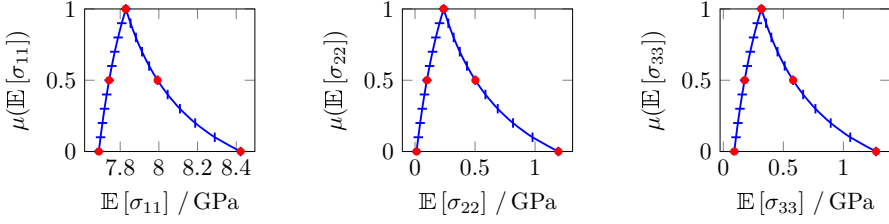


**Figure 17.** Fuzzy-stochastic analysis: output membership functions for expectation values of normal stresses (left)  $\mathbb{E}[\sigma_{11}]$ , (center)  $\mathbb{E}[\sigma_{22}]$ , and (right)  $\mathbb{E}[\sigma_{33}]$ .

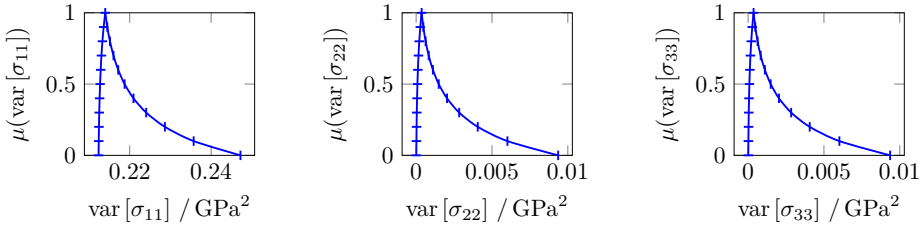


**Figure 18.** Fuzzy-stochastic analysis: output membership functions for variances of normal stresses (left)  $\text{var}[\sigma_{11}]$ , (center)  $\text{var}[\sigma_{22}]$ , and (right)  $\text{var}[\sigma_{33}]$ .

Figure 16 indicate the expectation values of the left upper bounds  $\bar{F}_{\alpha_k}(\sigma_{ii})$  and right lower bounds  $\underline{F}_{\alpha_k}(\sigma_{ii})$  at three  $\alpha$ -levels  $\alpha_1 = 0$ ,  $\alpha_6 = 0.5$ , and  $\alpha_{11} = 1$ . The same values are also shown by red dots in Figure 17. Among others, these figures are suitable for investigating the influence of design variables  $\underline{s}$  on statistical moments  $\mathbb{E}[\sigma_{ii}]$  and  $\text{var}[\sigma_{ii}]$ , respectively. Both in Figures 17 and 18 the sensitivity of the design variables  $\underline{s}$  can be clearly seen. Higher values of  $\underline{s}$  result in a larger increase in statistical moments than for smaller values of  $\underline{s}$ . The study of such influences are of great importance in industrial applications and can be used in the risk and reliability analysis.

**5.3. Hybrid fuzzy-stochastic analysis.** In the third representative example, all material parameters are the same as in the previous example in Section 5.2 except  $E_{\parallel}$ , which is assumed as a polymorphic uncertain material parameter  $E_{\parallel}(\omega, \underline{s})$  as illustrated in Figure 19. For a hybrid fuzzy-stochastic analysis the input material parameter vector equation (41) is given as

$$\underline{\kappa}(\omega, \underline{s}) = [E_{\parallel}(\omega, \underline{s}), E_{\perp}(\underline{s}), G_{\parallel}(\underline{s}), G_{\perp}, \nu(\omega)]^T, \tag{54}$$

whereas the design variable vector equation (1) of material parameters is given by

$$\underline{s} = [s_1, s_2, s_3, s_4]^T = [\hat{E}_{\parallel 0}, \hat{E}_{\parallel 1}, E_{\perp}, G_{\parallel}]^T. \tag{55}$$

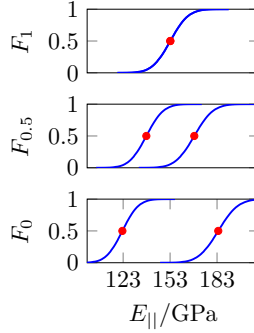


**Figure 19.** Hybrid fuzzy-stochastic analysis: P-boxes at  $\alpha$ -levels  $\alpha_1 = 0$ ,  $\alpha_6 = 0.5$ , and  $\alpha_{11} = 1$  for  $E_{||}$ .

The PCE in (12) for the polymorphic uncertain and stochastic parameters  $E_{||}(\omega, \underline{s})$  and  $\nu(\omega)$  is truncated by  $n_P = 2$ . The membership functions  $\mu(\underline{s})$  and the density distributions for the purely fuzzy parameters  $E_{\perp}(\underline{s})$  and  $G_{||}(\underline{s})$  and the purely stochastic parameter  $\nu(\omega)$ , respectively, remain unchanged according to Figures 11a,d and 14.

According to (13), the PCEs for the (fuzzy-)random variables  $E_{||}(\omega, \underline{s})$  and  $\nu(\omega)$  for  $n_P = 2$  are

$$\begin{aligned} E_{||}(\omega, \underline{s}) &= \widehat{E}_{||0}(\underline{s}) + \widehat{E}_{||1}(\underline{s})\theta_1(\omega) + \widehat{E}_{||2}(\underline{s})\theta_2(\omega), \\ \nu(\omega) &= \widehat{\nu}_0 + \widehat{\nu}_1\theta_1(\omega) + \widehat{\nu}_2\theta_2(\omega). \end{aligned} \quad (56)$$

We assume, further, that  $E_{||}(\omega, \underline{s})$  and  $\nu(\omega)$  are stochastically independent such that (56) renders

$$\begin{aligned} E_{||}(\omega, \underline{s}) &= \widehat{E}_{||0}(\underline{s}) + \widehat{E}_{||1}(\underline{s})\theta_1(\omega), \\ \nu(\omega) &= \widehat{\nu}_0 + \widehat{\nu}_2\theta_2(\omega), \end{aligned} \quad (57)$$

with PC coefficients

$$\begin{aligned} \widehat{E}_{||0}(\underline{s}) &= \mathbb{E}[E_{||}(\underline{s})] = s_1, & \widehat{E}_{||1}(\underline{s}) &= \text{std}[E_{||}(\underline{s})] = s_2, \\ \widehat{\nu}_0 &= \mathbb{E}[\nu] = 0.306, & \widehat{\nu}_2 &= \text{std}[\nu] = 0.0528. \end{aligned} \quad (58)$$

Consequently, the corresponding input matrix in (16) of material parameter PC coefficients becomes

$$\widehat{\underline{k}}(\underline{s}) = \begin{bmatrix} \widehat{E}_{||0}(\underline{s}) & \widehat{E}_{||1}(\underline{s}) & 0 \\ E_{\perp}(\underline{s}) & 0 & 0 \\ G_{||}(\underline{s}) & 0 & 0 \\ G_{\perp} & 0 & 0 \\ \widehat{\nu}_0 & 0 & \widehat{\nu}_2 \end{bmatrix} = \begin{bmatrix} s_1 & s_2 & 0 \\ s_3 & 0 & 0 \\ s_4 & 0 & 0 \\ 3.9286 & 0 & 0 \\ 0.306 & 0 & 0.0528 \end{bmatrix}. \quad (59)$$

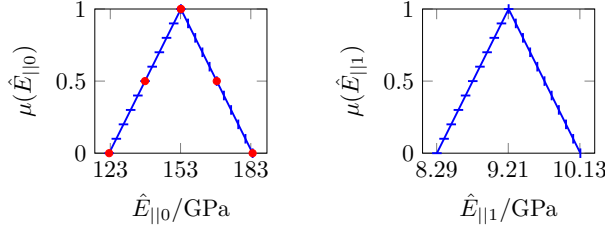


**Figure 20.** Hybrid fuzzy-stochastic analysis: input membership functions for (left) the zeros  $\widehat{E}_{\parallel 0}$  and (right) first  $\widehat{E}_{\parallel 1}$  PC coefficients of  $E_{\parallel}$ .

In this example, the corresponding artificially chosen input membership functions for  $s_1 = \mathbb{E}[E_{\parallel}(\omega, \underline{s})] = \widehat{E}_{\parallel 0}$  and  $s_2 = \text{std}[E_{\parallel}(\omega, \underline{s})] = \widehat{E}_{\parallel 1}$  are shown in Figure 20. Therefore,  $E_{\parallel}(\omega, \underline{s})$  becomes a hybrid fuzzy-stochastic variable, i.e., the CDF of  $E_{\parallel}(\omega, \underline{s})$  is not anymore given by unique function as depicted in Figure 14c. Instead, the CDF is given by left upper bounds  $\overline{F}_{\alpha_k}(E_{\parallel})$  and right lower bounds  $\underline{F}_{\alpha_k}(E_{\parallel})$  at each  $\alpha$ -level. Then, the P-boxes of Young’s modulus  $[\overline{F}_{\alpha_k}(E_{\parallel}), \underline{F}_{\alpha_k}(E_{\parallel})]$  at three  $\alpha$ -levels  $\alpha_1 = 0$ ,  $\alpha_6 = 0.5$ , and  $\alpha_{11} = 1$  are shown in Figure 19. The red dots in Figure 19 indicate the expectation values of left upper bounds  $\overline{F}_{\alpha_k}(E_{\parallel})$  and right lower bounds  $\underline{F}_{\alpha_k}(E_{\parallel})$  at the three  $\alpha$ -levels. The same values are also shown by red dots in Figure 20, left.

The fuzzy and the stochastic analysis are combined to a hybrid fuzzy-stochastic approach. In Figure 21, the resulting output membership functions of the optimization problems in (37) for the three possible realizations of surrogate QoIs presented in (20)–(22) are illustrated. The – and | marks show that from each pair of interval bounds of the design variables  $s_{i,\alpha_k}^L$  and  $s_{i,\alpha_k}^R$  at each  $\alpha$ -level  $\alpha_k$ ,  $k = 1, \dots, 11$ , in (49), the interval bounds of the QoIs  $Q_{\alpha_k}^{\omega L}$  and  $Q_{\alpha_k}^{\omega R}$  are obtained. Therefore, for postprocessing, e.g., calculating the stresses  $\underline{\sigma}(\omega, \underline{s})$  in (38), the left and right interval bounds  $s_{i,\alpha_k}^L$  and  $s_{i,\alpha_k}^R$  at each  $\alpha$ -level  $\alpha_k$ ,  $k = 1, \dots, 11$ , can be used.

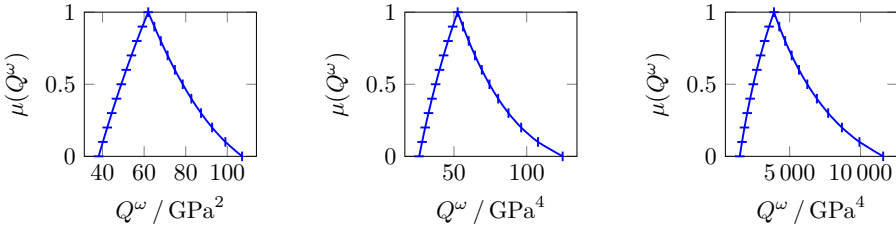


**Figure 21.** Hybrid fuzzy-stochastic analysis: membership function for surrogate QoIs in (20)–(22) according to QoI in (40), (left)  $Q^{\omega} = \mathbb{E}[Q]$ , (center)  $Q^{\omega} = \text{var}[Q]$ , and (right)  $Q^{\omega} = \mathbb{E}[Q^2]$ .

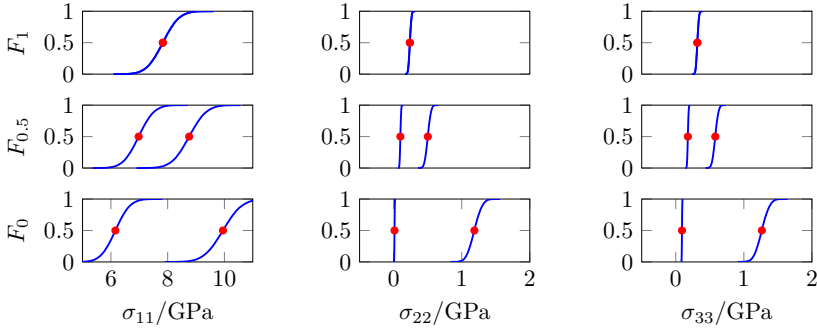


**Figure 22.** Hybrid fuzzy-stochastic analysis: P-boxes at  $\alpha$ -levels  $\alpha_1 = 0$ ,  $\alpha_6 = 0.5$  and  $\alpha_{11} = 1$  for normal stresses  $\sigma_{11}$ ,  $\sigma_{22}$ ,  $\sigma_{33}$ .

The purely fuzzy or deterministic shear stresses remain unchanged compared to the first example in Section 5.1. The P-boxes of the normal stresses  $\sigma_{ii}(\omega, \underline{s})$ , which depend on deterministic  $G_{\perp}$ , fuzzy  $E_{\perp}(\underline{s})$  and  $G_{\parallel}(\underline{s})$ , stochastic  $\nu(\omega)$ , and hybrid fuzzy-stochastic  $E_{\parallel}(\omega, \underline{s})$  parameters, are shown in Figure 22 for three  $\alpha$ -levels. In contrast to the previous example in Section 5.2, wider breadth is obtained between the left upper bounds  $\bar{F}_{\alpha_k}(\sigma_{11})$  and right lower bounds  $\underline{F}_{\alpha_k}(\sigma_{11})$  for each  $\alpha$ -level, whereas the bound distributions for  $\sigma_{22}$  and  $\sigma_{33}$  are narrow, which was to be expected because of the wider input of  $E_{\parallel}$ . In addition, the membership functions for the expectation values and the variances of  $\sigma_{11}$ ,  $\sigma_{22}$ , and  $\sigma_{33}$  are given in Figure 23. The sensitivity of the design variables  $\underline{s}$  can be clearly seen in

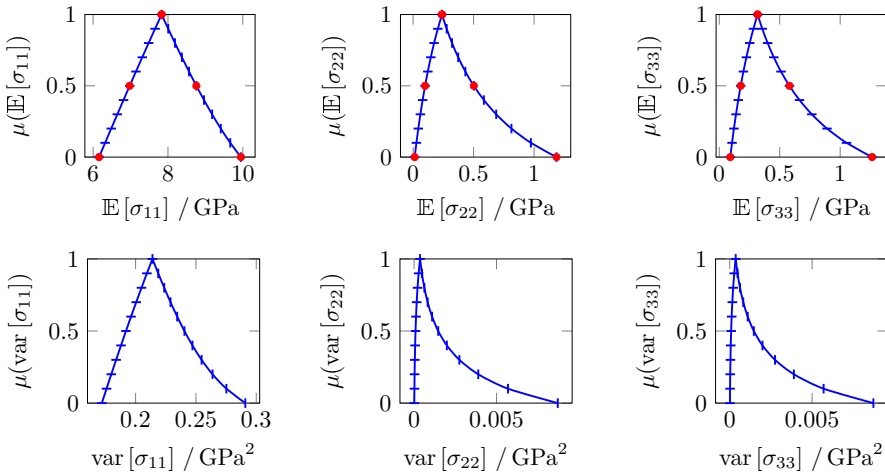


**Figure 23.** Hybrid fuzzy-stochastic analysis: output membership functions for expectation values (top row) and variances (bottom row) of normal stresses.

both figures. Higher values of  $\underline{\delta}$  result in a larger increase in statistical moments than for smaller values of  $\underline{\delta}$ .

## 6. Conclusion and outlook

The objective of this article is to consider polymorphic uncertain material parameters, for unidirectional FRP, in a hybrid fuzzy-stochastic transversely isotropic elastic model. For this purpose, a state and a target problem is formulated as (fuzzy) stochastic equations that take into account PC expanded (fuzzy) random variables, where the PC coefficients are interpreted as fuzzy design variables. To this end, a stochastic Galerkin projection is applied to reduce the (fuzzy) stochastic equation into a system of (fuzzy) equations. Hence, the target problem or the QoI depends only on (fuzzy) PC coefficients. The fuzzy analysis, including  $\alpha$ -level optimization, is used to get representative membership functions for QoIs. Since the QoIs may be random variables, surrogate QoIs based on empirical moments are used to perform the fuzzy optimization. The material parameters for the proposed model are determined based on homogeneous experiments of tensile specimens with different fiber orientations. This is followed by statistic evaluations of material parameters. These results are used for the generation of stochastic distributions or fuzzy membership functions, respectively, and applied as input quantities for the numerical analysis. Representative examples, for fuzzy analysis, fuzzy-stochastic analysis, and hybrid fuzzy-stochastic analysis demonstrate the versatility of the proposed model.

In the future, inhomogeneous experiments will be carried out for validation and compared with the proposed hybrid fuzzy-stochastic transversely isotropic elastic model of unidirectional FRP. Furthermore, a multiscale model should be developed, which takes into account a polymorphic uncertain homogenization method, where the composite material may exhibit polymorphic uncertainties in the constituent material properties.

## Acknowledgements

The support of the research in this work by “DFG Schwerpunktprogramm SPP 1886: Polymorphic uncertainty modeling for the numerical design of structures” is gratefully acknowledged.

## References

- [Acharjee 2006] S. Acharjee, *Stochastic and deterministic techniques for computational design of deformation process*, Ph.D. thesis, Cornell University, 2006.
- [Acharjee and Zabarar 2006] S. Acharjee and N. Zabarar, “Uncertainty propagation in finite deformations: a spectral stochastic Lagrangian approach”, *Comput. Methods Appl. Mech. Engrg.* **195**:19–22 (2006), 2289–2312.

- [Anders and Hori 1999] M. Anders and M. Hori, “Stochastic finite element method for elasto-plastic body”, *Internat. J. Numer. Methods Engrg.* **46**:11 (1999), 1897–1916.
- [Beer 2009] M. Beer, “Fuzzy probability theory”, pp. 4047–4059 in *Encyclopedia of complexity and systems science*, edited by R. A. Meyers, Springer, 2009.
- [Bertsekas 1982] D. P. Bertsekas, “Projected Newton methods for optimization problems with simple constraints”, *SIAM J. Control Optim.* **20**:2 (1982), 221–246.
- [Caffisch 1998] R. E. Caffisch, “Monte Carlo and quasi-Monte Carlo methods”, *Acta Numer.* **7** (1998), 1–49.
- [Caylak et al. 2018] I. Caylak, E. Penner, A. Dridger, and R. Mahnken, “Stochastic hyperelastic modeling considering dependency of material parameters”, *Comput. Mech.* **62**:6 (2018), 1273–1285.
- [Dempster 1967] A. P. Dempster, “Upper and lower probabilities induced by a multivalued mapping”, *Ann. Math. Statist.* **38** (1967), 325–339.
- [Dubois and Prade 2012] D. Dubois and H. Prade, “Possibility theory”, pp. 2240–2252 in *Computational complexity*, edited by R. A. Meyers, Springer, 2012.
- [Ferson et al. 2003] S. Ferson, V. Kreinovich, L. Grinburg, D. Myers, and K. Sentz, “Constructing probability boxes and Dempster–Shafer structures”, tech. report SAND2002-4015, Sandia National Laboratories, 2003, Available at <https://www.osti.gov/biblio/1427258>.
- [Ghanem and Spanos 1991] R. G. Ghanem and P. D. Spanos, *Stochastic finite elements: a spectral approach*, Springer, 1991.
- [Graf et al. 2015] W. Graf, M. Götz, and M. Kaliske, “Analysis of dynamical processes under consideration of polymorphic uncertainty”, *Struct. Safety* **52**:B (2015), 194–201.
- [Gudder 1998] S. Gudder, “Fuzzy probability theory”, *Demonstratio Math.* **31**:1 (1998), 235–254.
- [Hurtado and Barbat 1998] J. E. Hurtado and A. H. Barbat, “Monte Carlo techniques in computational stochastic mechanics”, *Arch. Comput. Methods Engrg.* **5**:1 (1998), 3–29.
- [Jahani et al. 2014] E. Jahani, R. L. Muhanna, M. A. Shayanfar, and M. A. Barkhordari, “Reliability assessment with fuzzy random variables using interval Monte Carlo simulation”, *Comput.-Aid. Civ. Infrastruct. Eng.* **29**:3 (2014), 208–220.
- [Jardak et al. 2002] M. Jardak, C.-H. Su, and G. E. Karniadakis, “Spectral polynomial chaos solutions of the stochastic advection equation”, *J. Sci. Comput.* **17**:1–4 (2002), 319–338.
- [Keese 2004] A. Keese, *Numerical solution of systems with stochastic uncertainties: a general purpose framework for stochastic finite elements*, Ph.D. thesis, Technische Universität Braunschweig, 2004, Available at [https://publikationsserver.tu-braunschweig.de/receive/dbbs\\_mods\\_00001595](https://publikationsserver.tu-braunschweig.de/receive/dbbs_mods_00001595).
- [Le Maître and Knio 2010] O. P. Le Maître and O. M. Knio, *Spectral methods for uncertainty quantification: with applications to computational fluid dynamics*, Springer, 2010.
- [Le Maître et al. 2001] O. P. Le Maître, O. M. Knio, H. N. Najm, and R. G. Ghanem, “A stochastic projection method for fluid flow, I: Basic formulation”, *J. Comput. Phys.* **173**:2 (2001), 481–511.
- [Le Maître et al. 2002] O. P. Le Maître, M. T. Reagan, H. N. Najm, R. G. Ghanem, and O. M. Knio, “A stochastic projection method for fluid flow, II: Random process”, *J. Comput. Phys.* **181**:1 (2002), 9–44.
- [Mahnken 2017] R. Mahnken, “A variational formulation for fuzzy analysis in continuum mechanics”, *Math. Mech. Complex Syst.* **5**:3–4 (2017), 261–298.
- [Möller and Beer 2004] B. Möller and M. Beer, *Fuzzy randomness: uncertainty in civil engineering and computational mechanics*, Springer, 2004.
- [Motamed 2017] M. Motamed, “Fuzzy-stochastic partial differential equations”, preprint, 2017. arXiv

- [Nocedal and Wright 1999] J. Nocedal and S. J. Wright, *Numerical optimization*, Springer, 1999.
- [Reuter et al. 2012] U. Reuter, J.-U. Sickert, W. Graf, and M. Kaliske, “Modeling and processing of uncertainty in civil engineering by means of fuzzy randomness”, pp. 291–306 in *Managing safety of heterogeneous systems*, edited by Y. Ermoliev et al., Lecture Notes in Economics and Mathematical Systems **658**, Springer, 2012.
- [Rosić 2013] B. Rosić, “Variational formulations and functional approximation algorithms in stochastic plasticity of materials”, in *2nd ECCOMAS Young Investigators Conference* (Bordeaux, 2013), ECCOMAS, Barcelona, 2013.
- [Soden et al. 1998] P. D. Soden, M. J. Hinton, and A. S. Kaddour, “Lamina properties, lay-up configurations and loading conditions for a range of fibre-reinforced composite laminates”, *Compos. Sci. Tech.* **58**:7 (1998), 1011–1022.
- [Sullivan 2015] T. J. Sullivan, *Introduction to uncertainty quantification*, Texts in Applied Mathematics **63**, Springer, 2015.
- [Walley 1991] P. Walley, *Statistical reasoning with imprecise probabilities*, Monographs on Statistics and Applied Probability **42**, Chapman and Hall, London, 1991.
- [Wang and Zhang 1992] G. Y. Wang and Y. Zhang, “The theory of fuzzy stochastic processes”, *Fuzzy Sets and Systems* **51**:2 (1992), 161–178.
- [Xiu and Karniadakis 2002] D. Xiu and G. E. Karniadakis, “The Wiener–Askey polynomial chaos for stochastic differential equations”, *SIAM J. Sci. Comput.* **24**:2 (2002), 619–644.
- [Xiu et al. 2001] D. Xiu, C.-H. Lucor, Didier Su, and G. E. Karniadakis, “Stochastic modeling of flow-structure interactions using generalized polynomial chaos”, *J. Fluid. Eng.* **124**:1 (2001), 51–59.
- [Zadeh 1965] L. A. Zadeh, “Fuzzy sets”, *Information and Control* **8** (1965), 338–353.

Received 6 Sep 2018. Revised 9 Jan 2019. Accepted 1 Mar 2019.

EDUARD PENNER: [penner@ltm.upb.de](mailto:penner@ltm.upb.de)

*Faculty of Mechanical Engineering, Paderborn University, Paderborn, Germany*

ISMAIL CAYLAK: [caylak@ltm.upb.de](mailto:caylak@ltm.upb.de)

*Faculty of Mechanical Engineering, Paderborn University, Paderborn, Germany*

ALEX DRIDGER: [dridger@ltm.upb.de](mailto:dridger@ltm.upb.de)

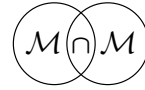
*Faculty of Mechanical Engineering, Paderborn University, Paderborn, Germany*

ROLF MAHNKEN: [rolf.mahnken@ltm.uni-paderborn.de](mailto:rolf.mahnken@ltm.uni-paderborn.de)

*Faculty of Mechanical Engineering, Paderborn University, Paderborn, Germany*







## DYNAMIC BOUNDARY CONDITIONS FOR MEMBRANES WHOSE SURFACE ENERGY DEPENDS ON THE MEAN AND GAUSSIAN CURVATURES

SERGEY GAVRILYUK AND HENRI GOUIN

Membranes are an important subject of study in physical chemistry and biology. They can be considered as material surfaces with a surface energy depending on the curvature tensor. Usually, mathematical models developed in the literature consider the dependence of surface energy only on mean curvature with an added linear term for Gauss curvature. Therefore, for closed surfaces the Gauss curvature term can be eliminated because of the Gauss–Bonnet theorem. Rosso and Virga (*Proc. Roy. Soc. Lond. A* **455**:1992 (1999), 4145–4168) considered the dependence on the mean and Gaussian curvatures in statics and under a restrictive assumption of the membrane inextensibility. The authors derived the shape equation as well as two scalar boundary conditions on the contact line.

In this paper — thanks to the principle of virtual working — the equations of motion and boundary conditions governing the fluid membranes subject to general dynamical bending are derived without the membrane inextensibility assumption. We obtain the dynamic “shape equation” (equation for the membrane surface) and the dynamic conditions on the contact line generalizing the classical Young–Dupré condition.

### 1. Introduction

The study of equilibrium, for small wetting droplets placed on a curved rigid surface, is an old problem of continuum mechanics. When the droplets’ size is of micron range the droplet volume energy can be neglected. The surface energy of the surface  $S$  can be expressed in the form

$$E = \iint_S \sigma \, ds,$$

where  $\sigma$  denotes the energy per unit surface. Two types of surfaces are present in physical problems:

---

**Communicated by Pierre Seppacher.**

*PACS2010*: 45.20.dg, 68.03.Cd, 68.35.Gy, 02.30.Xx.

*MSC2010*: primary 74K15, 76Z99; secondary 92C37.

*Keywords*: surface energy, curvature tensor, dynamic boundary conditions.

- rigid surfaces (only the kinematic boundary condition is imposed) and
- free surfaces (both the kinematic and dynamic boundary conditions are imposed).

We will see the difference between the energy variation in the case of rigid and free surfaces.

The simplest case corresponds to a constant surface energy  $\sigma$ , but in general,  $\sigma$  also depends on physical parameters (temperature, surfactant concentrations, etc. [Gouin 2014a; Rocard 1952; Steigmann and Li 1995]) and geometrical parameters (invariants of curvature tensor). The last case is important in biology and, in particular, in the dynamics of *vesicles* [Alberts et al. 2002; Lipowsky and Sackmann 1995; Seifert 1997]. Vesicles are small liquid droplets with a diameter of a few tens of micrometers, bounded by an impermeable lipid membrane of a few nanometers thick. The membranes are homogeneous down to molecular dimensions. Consequently, it is possible to model the boundary of vesicle as a two-dimensional smooth surface whose energy per unit surface  $\sigma$  is a function both of the sum (denoted by  $H$ ) and product (denoted by  $K$ ) of principal curvatures of the curvature tensor:

$$\sigma = \sigma(H, K).$$

In mathematical description of biological membranes, one often uses the Helfrich energy [1973; Tu 2011]:

$$\sigma(H, K) = \sigma_0 + \frac{\kappa}{2}(H - H_0)^2 + \bar{\kappa}K, \quad (1)$$

where  $\sigma_0$ ,  $H_0$ ,  $\kappa$ , and  $\bar{\kappa}$  are dimensional constants. Another purely mathematical example is the Wilmore energy [1993]:

$$\sigma(H, K) = H^2 - 4K.$$

This energy measures the “roundness” of the free surface. For a given volume, this energy is minimal in case of spheres. One can also propose another surface energy in the form

$$\sigma = \sigma_0 + h_0(H^2 - H_0^2)^2 + k_0(K - K_0)^2,$$

where  $\sigma_0$ ,  $h_0$ ,  $H_0$ ,  $k_0$ , and  $K_0$  are dimensional constants. This kind of energy is invariant under the change of sign of principal curvatures, (i.e., the change of sign yields  $H \rightarrow -H$  and  $K \rightarrow K$ ). It can thus describe the “mirror buckling” phenomenon: a portion of the membrane inverts to form a cap with equal but opposite principal curvatures. It is also a homogeneous function of degree four with respect to principal curvatures.

The equilibrium for membranes (called “shape equation” by Helfrich) is formulated in numerous papers and references herein [Biscari et al. 2004; Capovilla and

Guven 2002; Fournier 2007; Helfrich 1973; Napoli and Vergori 2010; Zhong-can and Helfrich 1989]. The “edge conditions” (boundary conditions at the contact line) are formulated in few papers and only in statics. In particular, in [Rosso and Virga 1999] the shape equation and two boundary conditions are formulated for the general dependence  $\sigma(H, K)$  under the assumption of the membrane inextensibility. However, the boundary conditions obtained do not contain the classical Young–Dupré condition for the constant surface energy. In the case where the energy depends only on  $H$  a static generalization of Young–Dupré condition was derived in [Gouin 2014b].

The aim of our paper is to develop the theory of moving membranes which are in contact with a solid surface. The surface energy of the membrane will be a function both of  $H$  and  $K$ . We obtain a set of boundary conditions on the moving interfaces (membranes) as well as on the moving edges.

The motion of a continuous medium is represented by a diffeomorphism  $\phi$  of a three-dimensional reference configuration  $D_0$  into the physical space. In order to analytically describe the transformation, variables  $\mathbf{X} = (X^1, X^2, X^3)^T$  single out individual particles corresponding to material or Lagrangian coordinates, where superscript “ $T$ ” means the transposition. The transformation representing the motion of a continuous medium occupying the material volume  $D_t$  is

$$\mathbf{x} = \phi(t, \mathbf{X}) \quad \text{or} \quad x^i = \phi^i(t, X^1, X^2, X^3), \quad i = \{1, 2, 3\},$$

where  $t$  denotes the time and  $\mathbf{x} = (x^1, x^2, x^3)^T$  denote the Eulerian coordinates. At  $t$  fixed, the transformation possesses an inverse and has continuous derivatives up to the second order (the dependence of the surface energy on the curvature tensor will regularize the solutions, so the cusps and shocks do not appear).

At equilibrium, the unit normal vector to a static surface  $\varphi_0(\mathbf{x}) = 0$  is the gradient of the so-called *signed distance function* defined as follows. Let

$$d(\mathbf{x}) = \begin{cases} \min|\mathbf{x} - \boldsymbol{\xi}| & \text{if } \varphi_0 > 0, \\ 0 & \text{if } \varphi_0 = 0, \\ -\min|\mathbf{x} - \boldsymbol{\xi}| & \text{if } \varphi_0 < 0, \end{cases} \quad (2)$$

where the minimum is taken over points  $\boldsymbol{\xi}$  at the surface, and  $|\cdot|$  denotes the Euclidean norm. The unit normal vector is

$$\mathbf{n} = \nabla d(\mathbf{x}).$$

In dynamical problems, the main difficulty in formulating boundary conditions comes from the fact that *one cannot assume that for all time  $t$  the unit normal vector to the surface is the gradient of the signed distance function.*

Indeed, if the material surface is moving, i.e., the surface position depends on time  $t$ , the surface points of the continuum medium are also moving and they will

depend implicitly on  $\mathbf{x}$ . Let  $\varphi(t, \mathbf{x}) = 0$  be the position of the material surface at time  $t$ . Its evolution is determined by the equation

$$\varphi_t + \mathbf{u}^T \nabla \varphi = 0, \quad (3)$$

where  $\mathbf{u}$  is the velocity of particles at the surface. Equation (3) is the classical kinematic condition for material moving interfaces. Let us derive the equation for the norm of  $\nabla \varphi$ . Taking the gradient of (3) and multiplying by  $\nabla \varphi$ , one obtains

$$(|\nabla \varphi|)_t + \mathbf{n}^T \nabla (\mathbf{u}^T \nabla \varphi) = 0, \quad (4)$$

where  $\mathbf{n} = \nabla \varphi / |\nabla \varphi|$  is the unit normal vector to surface  $\varphi(t, \mathbf{x}) = 0$ . It follows from (4) that, even if initially  $|\nabla \varphi| = 1$  (i.e., unit normal  $\mathbf{n}$  is defined at  $t = 0$  as the gradient of the signed distance function), this property is not conserved in time.

The following definitions and notations are used in the paper. For any vectors  $\mathbf{a}, \mathbf{b}$ , we write  $\mathbf{a}^T \mathbf{b}$  for their *scalar product* (the line vector is multiplied by the column vector), and  $\mathbf{a} \mathbf{b}^T$  for their *tensor product* (the column vector is multiplied by the line vector). The last product is usually denoted as  $\mathbf{a} \otimes \mathbf{b}$ . The product of a second-order tensor  $\mathbf{A}$  by a vector  $\mathbf{a}$  is denoted by  $\mathbf{A} \mathbf{a}$ . Notation  $\mathbf{b}^T \mathbf{A}$  means the covector  $\mathbf{c}^T$  defined by the rule  $\mathbf{c}^T = (\mathbf{A}^T \mathbf{b})^T$ . The identity tensor is denoted by  $\mathbf{I}$ .

The divergence of  $\mathbf{A}$  is covector  $\text{div } \mathbf{A}$  such that, for any constant vector  $\mathbf{h}$ , one has

$$(\text{div } \mathbf{A}) \mathbf{h} = \text{div}(\mathbf{A} \mathbf{h}),$$

i.e., the divergence of  $\mathbf{A}$  is a row vector, in which each component is the divergence of the corresponding column of  $\mathbf{A}$ . It implies

$$\text{div}(\mathbf{A} \mathbf{v}) = (\text{div } \mathbf{A}) \mathbf{v} + \text{tr} \left( \mathbf{A} \frac{\partial \mathbf{v}}{\partial \mathbf{x}} \right),$$

for any vector field  $\mathbf{v}$ . Here  $\text{tr}$  is the trace operator. If  $f$  is a real scalar function of  $\mathbf{x}$ ,  $\frac{\partial f}{\partial \mathbf{x}}$  is the linear form (line vector) associated with the gradient of  $f$  (column vector):  $\frac{\partial f}{\partial \mathbf{x}} = (\nabla f)^T$ .

If  $\mathbf{n}$  is the unit normal vector to a surface,  $\mathbf{P} = \mathbf{I} - \mathbf{n} \mathbf{n}^T$  is the projector on the surface with the classical properties

$$\mathbf{P}^2 = \mathbf{P}, \quad \mathbf{P}^T = \mathbf{P}, \quad \mathbf{P} \mathbf{n} = \mathbf{0}, \quad \mathbf{n}^T \mathbf{P} = \mathbf{0}.$$

For any scalar field  $f$ , the vector field  $\mathbf{v}$ , and second-order tensor field  $\mathbf{A}$ , the tangential surface gradient, tangential surface divergence, Beltrami–Laplace operator, and tangent tensors are defined as

$$\begin{aligned} \mathbf{v}_{\text{tg}} &= \mathbf{P} \mathbf{v}, & \mathbf{A}_{\text{tg}} &= \mathbf{P} \mathbf{A}, & \nabla_{\text{tg}} f &= \mathbf{P} \nabla f, \\ \text{div}_{\text{tg}} \mathbf{v}_{\text{tg}} &= \text{tr} \left( \mathbf{P} \frac{\partial \mathbf{v}_{\text{tg}}}{\partial \mathbf{x}} \right), & \Delta_{\text{tg}} f &= \text{div}_{\text{tg}} (\nabla_{\text{tg}} f), \end{aligned}$$

and for any constant vector  $\mathbf{h}$ ,

$$\operatorname{div}_{\text{tg}}(\mathbf{A}_{\text{tg}}\mathbf{h}) = \operatorname{div}_{\text{tg}}(\mathbf{A}_{\text{tg}})\mathbf{h}.$$

The following relations between surface operators and classical operators applied to tangential tensors in the sense of previous definitions are valid:

$$\operatorname{div}_{\text{tg}} \mathbf{v}_{\text{tg}} = \operatorname{div} \mathbf{v}_{\text{tg}} + \mathbf{n}^T \left( \frac{\partial \mathbf{n}}{\partial \mathbf{x}} \right)^T \mathbf{v}_{\text{tg}}, \quad (5)$$

$$\operatorname{div}_{\text{tg}} \mathbf{v}_{\text{tg}} = \mathbf{n}^T \operatorname{rot}(\mathbf{n} \times \mathbf{v}_{\text{tg}}), \quad (6)$$

$$\operatorname{div}_{\text{tg}} \mathbf{A}_{\text{tg}} = \operatorname{div} \mathbf{A}_{\text{tg}} + \mathbf{n}^T \left( \frac{\partial \mathbf{n}}{\partial \mathbf{x}} \right)^T \mathbf{A}_{\text{tg}}, \quad (7)$$

$$\operatorname{div}_{\text{tg}}(f \mathbf{v}_{\text{tg}}) = f \operatorname{div}_{\text{tg}} \mathbf{v}_{\text{tg}} + (\nabla_{\text{tg}} f)^T \mathbf{v}_{\text{tg}}, \quad (8)$$

$$\operatorname{div}_{\text{tg}}(f \mathbf{A}_{\text{tg}}) = f \operatorname{div}_{\text{tg}} \mathbf{A}_{\text{tg}} + (\nabla_{\text{tg}} f)^T \mathbf{A}_{\text{tg}}, \quad (9)$$

where  $\operatorname{rot}$  denotes the curl operator. The proof is straightforward. Indeed, since

$$\frac{\partial(\mathbf{n}^T \mathbf{v}_{\text{tg}})}{\partial \mathbf{x}} = \mathbf{n}^T \left( \frac{\partial \mathbf{v}_{\text{tg}}}{\partial \mathbf{x}} \right) + \mathbf{v}_{\text{tg}}^T \left( \frac{\partial \mathbf{n}}{\partial \mathbf{x}} \right) = 0,$$

one has

$$\operatorname{div}_{\text{tg}} \mathbf{v}_{\text{tg}} = \operatorname{tr} \left( \mathbf{P} \frac{\partial \mathbf{v}_{\text{tg}}}{\partial \mathbf{x}} \right) = \operatorname{div} \mathbf{v}_{\text{tg}} - \mathbf{n}^T \left( \frac{\partial \mathbf{v}_{\text{tg}}}{\partial \mathbf{x}} \right) \mathbf{n} = \operatorname{div} \mathbf{v}_{\text{tg}} + \mathbf{n}^T \left( \frac{\partial \mathbf{n}}{\partial \mathbf{x}} \right)^T \mathbf{v}_{\text{tg}},$$

which proves relation (5). To prove relation (6), one uses the following identity valid for any vector fields  $\mathbf{a}$  and  $\mathbf{b}$ :

$$\operatorname{rot}(\mathbf{a} \times \mathbf{b}) = \mathbf{a} \operatorname{div} \mathbf{b} - \mathbf{b} \operatorname{div} \mathbf{a} + \frac{\partial \mathbf{a}}{\partial \mathbf{x}} \mathbf{b} - \frac{\partial \mathbf{b}}{\partial \mathbf{x}} \mathbf{a}.$$

We apply this identity to the vectors  $\mathbf{a} = \mathbf{n}$  and  $\mathbf{b} = \mathbf{v}_{\text{tg}}$ . Multiplying on the left by  $\mathbf{n}^T$ , one obtains relation (6). Relations (7), (8), and (9) are direct consequences of relation (5).

## 2. Curvature tensor

The unit normal vector being prolonged in the surface vicinity, we can directly obtain the expression of its derivative:

$$\frac{\partial \mathbf{n}}{\partial \mathbf{x}} = \mathbf{P} \frac{\varphi''}{|\nabla \varphi|},$$

where  $\varphi''$  is the Hessian matrix of  $\varphi$  with respect to  $\mathbf{x}$ . One obviously has

$$\mathbf{n}^T \frac{\partial \mathbf{n}}{\partial \mathbf{x}} = \mathbf{0}.$$

However, since in dynamics  $\mathbf{n}$  is not the gradient of the signed distance function, we cannot have the property

$$\frac{\partial \mathbf{n}}{\partial \mathbf{x}} \mathbf{n} = \mathbf{0}. \quad (10)$$

The curvature tensor is defined as

$$\mathbf{R} = -\mathbf{P} \frac{\varphi''}{|\nabla \varphi|} \mathbf{P} = -\frac{\partial \mathbf{n}}{\partial \mathbf{x}} \mathbf{P}.$$

Hence, in dynamics

$$\mathbf{R} \neq -\frac{\partial \mathbf{n}}{\partial \mathbf{x}}.$$

Let us note that the derivation of the shape equation and boundary conditions in statics always uses property (10) and the curvature tensor coming from the definition of the signed distance function. In dynamics, we cannot use these properties and new tools should be developed.

Tensor  $\mathbf{R}$  is symmetric and has zero as an eigenvalue:

$$\mathbf{R} = \mathbf{R}^T, \quad \mathbf{R}\mathbf{n} = \mathbf{0}.$$

In the eigenbasis, tensor  $\mathbf{R}$  is diagonal:

$$\mathbf{R} = \begin{pmatrix} c_1 & 0 & 0 \\ 0 & c_2 & 0 \\ 0 & 0 & 0 \end{pmatrix},$$

where  $c_1, c_2$  are the principal curvatures. The two invariants of curvature tensor  $\mathbf{R}$  are

$$H = c_1 + c_2, \quad K = c_1 c_2.$$

Invariant  $H$  is the double mean curvature, and invariant  $K$  is the Gaussian curvature. They can also be expressed in the form

$$H = \operatorname{tr} \mathbf{R} = -\operatorname{tr} \left( \frac{\partial \mathbf{n}}{\partial \mathbf{x}} \right),$$

$$2K = (\operatorname{tr} \mathbf{R})^2 - \operatorname{tr}(\mathbf{R}^2) = \left[ \operatorname{tr} \left( \frac{\partial \mathbf{n}}{\partial \mathbf{x}} \right) \right]^2 - \operatorname{tr} \left[ \left( \frac{\partial \mathbf{n}}{\partial \mathbf{x}} \right)^2 \right].$$

**Lemma 1.** *The following identities are valid:*

$$\begin{aligned} \operatorname{div}_{\text{tg}} \mathbf{P} &= H \mathbf{n}^T, \\ \operatorname{div}_{\text{tg}} \mathbf{R} &= \nabla_{\text{tg}}^T H + (H^2 - 2K) \mathbf{n}^T, \\ \mathbf{R}^2 &= H \mathbf{R} - K \mathbf{P}. \end{aligned}$$

*Proof.* First, let us remark that  $\mathbf{P} = \mathbf{P}_{\text{tg}}$  and  $\mathbf{R} = \mathbf{R}_{\text{tg}}$ . One can apply (7) to obtain

$$\begin{aligned}\operatorname{div}_{\text{tg}} \mathbf{P} &= -\operatorname{div}(\mathbf{n}\mathbf{n}^T) + \mathbf{n}^T \left( \frac{\partial \mathbf{n}}{\partial \mathbf{x}} \right)^T \mathbf{P} \\ &= -(\operatorname{div} \mathbf{n})\mathbf{n}^T - \mathbf{n}^T \left( \frac{\partial \mathbf{n}}{\partial \mathbf{x}} \right)^T + \mathbf{n}^T \left( \frac{\partial \mathbf{n}}{\partial \mathbf{x}} \right)^T (\mathbf{I} - \mathbf{n}\mathbf{n}^T) \\ &= -(\operatorname{div} \mathbf{n})\mathbf{n}^T,\end{aligned}$$

which proves the first relation. The proof of the second relation is as follows:

$$\begin{aligned}\operatorname{div} \mathbf{R} &= -\operatorname{div} \left( \frac{\partial \mathbf{n}}{\partial \mathbf{x}} \right) + \operatorname{div} \left( \frac{\partial \mathbf{n}}{\partial \mathbf{x}} \mathbf{n}\mathbf{n}^T \right) \\ &= -\frac{\partial(\operatorname{div} \mathbf{n})}{\partial \mathbf{x}} + \operatorname{div} \left( \frac{\partial \mathbf{n}}{\partial \mathbf{x}} \right) \mathbf{n}^T + \mathbf{n}^T \left( \left( \frac{\partial \mathbf{n}}{\partial \mathbf{x}} \right)^2 \right)^T \\ &= -\frac{\partial(\operatorname{div} \mathbf{n})}{\partial \mathbf{x}} + \operatorname{div} \left( \frac{\partial \mathbf{n}}{\partial \mathbf{x}} \right) \mathbf{n}\mathbf{n}^T + \operatorname{tr} \left( \left( \frac{\partial \mathbf{n}}{\partial \mathbf{x}} \right)^2 \right) \mathbf{n}^T + \mathbf{n}^T \left( \left( \frac{\partial \mathbf{n}}{\partial \mathbf{x}} \right)^2 \right)^T \\ &= \frac{\partial H}{\partial \mathbf{x}} \mathbf{P} + \operatorname{tr} \left( \left( \frac{\partial \mathbf{n}}{\partial \mathbf{x}} \right)^2 \right) \mathbf{n}^T - \mathbf{n}^T \left( \frac{\partial \mathbf{n}}{\partial \mathbf{x}} \right)^T \mathbf{R}.\end{aligned}$$

Consequently,

$$\operatorname{div}_{\text{tg}} \mathbf{R} = \frac{\partial H}{\partial \mathbf{x}} \mathbf{P} + \operatorname{tr} \left( \left( \frac{\partial \mathbf{n}}{\partial \mathbf{x}} \right)^2 \right) \mathbf{n}^T.$$

Using  $\operatorname{tr} \left( \left( \frac{\partial \mathbf{n}}{\partial \mathbf{x}} \right)^2 \right) = \operatorname{tr}(\mathbf{R}^2) = H^2 - 2K$ , we obtain the second relation of the lemma.

Now, the curvature tensor satisfies the Cayley–Hamilton theorem:

$$\mathbf{R}^3 - H\mathbf{R}^2 + K\mathbf{R} = 0.$$

The minimal polynomial is

$$\mathbf{R}^2 - H\mathbf{R} + K\mathbf{P} = 0,$$

which proves the third relation.  $\square$

### 3. Virtual motion

Define a one-parameter family of *virtual motions*

$$\mathbf{x} = \mathbf{\Phi}(t, \mathbf{X}, \lambda)$$

with scalar  $\lambda \in O$ , where  $O$  is an open real interval containing zero and such that  $\mathbf{\Phi}(t, \mathbf{X}, 0) = \mathbf{\phi}(t, \mathbf{X})$  (the motion of the continuous medium is obtained for  $\lambda = 0$ ).

The *virtual displacement* of particle  $X$  is defined as [Gavrilyuk 2011; Serrin 1959]

$$\delta \mathbf{x}(t, \mathbf{X}) = \left. \frac{\partial \Phi(t, \mathbf{X}, \lambda)}{\partial \lambda} \right|_{\lambda=0}.$$

In the following, the symbol  $\delta$  means the derivative with respect to  $\lambda$  at fixed Lagrangian coordinates  $\mathbf{X}$  and  $t$ , for  $\lambda = 0$ . We will also denote by  $\boldsymbol{\zeta}(t, \mathbf{x})$  the virtual displacement expressed as a function of Eulerian coordinates:

$$\boldsymbol{\zeta}(t, \mathbf{x}) = \boldsymbol{\zeta}(t, \boldsymbol{\phi}(t, \mathbf{X})) = \delta \mathbf{x}(t, \mathbf{X}).$$

#### 4. Variational tools

We assume that  $D_t$  has a smooth boundary  $S_t$  with edge  $C_t$ . We respectively denote by  $D_0$ ,  $S_0$ , and  $C_0$  the images of  $D_t$ ,  $S_t$ , and  $C_t$  in the reference space (of Lagrangian coordinates). The unit vector  $\mathbf{n}$  and its image  $\mathbf{n}_0$  are the oriented normal vectors to  $S_t$  and  $S_0$ ; the vector  $\mathbf{t}$  is the oriented unit tangent vector to  $C_t$  and  $\mathbf{n}' = \mathbf{t} \times \mathbf{n}$  is the unit binormal vector (see Figure 1).  $\mathbf{F} = \frac{\partial \boldsymbol{\phi}(t, \mathbf{X})}{\partial \mathbf{X}} \equiv \frac{\partial \mathbf{x}}{\partial \mathbf{X}}$  is the deformation gradient. For the sake of simplicity, we will use the same notations for quantities as  $\mathbf{F}$ ,  $\mathbf{n}$ , etc., both in Eulerian and Lagrangian coordinates.

**Lemma 2.** *We have the relations*

$$\delta \det \mathbf{F} = \det \mathbf{F} \operatorname{div} \boldsymbol{\zeta}, \quad (11)$$

$$\delta \mathbf{n} = -\mathbf{P} \left( \frac{\partial \boldsymbol{\zeta}}{\partial \mathbf{x}} \right)^T \mathbf{n}, \quad (12)$$

$$\delta(\mathbf{F}^{-1} \mathbf{n}) = -\mathbf{F}^{-1} \frac{\partial \boldsymbol{\zeta}}{\partial \mathbf{x}} \mathbf{n} + \mathbf{F}^{-1} \delta \mathbf{n}, \quad (13)$$

$$\delta \left( \frac{\partial \mathbf{n}}{\partial \mathbf{x}} \right) = \frac{\partial \delta \mathbf{n}}{\partial \mathbf{x}} - \frac{\partial \mathbf{n}}{\partial \mathbf{x}} \frac{\partial \boldsymbol{\zeta}}{\partial \mathbf{x}}. \quad (14)$$

*Proof of relation (11).* The Jacobi formula for the determinant is

$$\delta(\det \mathbf{F}) = \det \mathbf{F} \operatorname{tr}(\mathbf{F}^{-1} \delta \mathbf{F}).$$

Also,

$$\delta \mathbf{F} = \delta \left( \frac{\partial \mathbf{x}}{\partial \mathbf{X}} \right) = \frac{\partial \delta \mathbf{x}}{\partial \mathbf{X}}.$$

Then

$$\operatorname{tr}(\mathbf{F}^{-1} \delta \mathbf{F}) = \operatorname{tr} \left( \frac{\partial \mathbf{X}}{\partial \mathbf{x}} \frac{\partial \delta \mathbf{x}}{\partial \mathbf{X}} \right) = \operatorname{tr} \left( \frac{\partial \delta \mathbf{x}}{\partial \mathbf{X}} \frac{\partial \mathbf{X}}{\partial \mathbf{x}} \right) = \operatorname{tr} \left( \frac{\partial \boldsymbol{\zeta}}{\partial \mathbf{x}} \right) = \operatorname{div} \boldsymbol{\zeta}. \quad \square$$

*Proof of relation (12).* Surface  $\varphi(t, \mathbf{x}) = 0$  is a material surface. It can be represented in the Lagrangian coordinates as  $\varphi(t, \mathbf{x}) = \varphi_0(\mathbf{X})$ , which implies that  $\delta \varphi = 0$ .

Also,

$$\delta\left(\frac{\partial\varphi}{\partial\mathbf{x}}\right) = \delta\left(\frac{\partial\varphi}{\partial\mathbf{X}}\mathbf{F}^{-1}\right) = \frac{\partial\delta\varphi}{\partial\mathbf{x}} - \frac{\partial\varphi}{\partial\mathbf{x}}\frac{\partial\boldsymbol{\zeta}}{\partial\mathbf{x}} = -\frac{\partial\varphi}{\partial\mathbf{x}}\frac{\partial\boldsymbol{\zeta}}{\partial\mathbf{x}}.$$

Here we used the following expression for the variation of  $\mathbf{F}^{-1}$  coming from the relation  $\mathbf{F}^{-1}\mathbf{F} = \mathbf{I}$ :

$$\delta\mathbf{F}^{-1} = -\mathbf{F}^{-1}\frac{\partial\boldsymbol{\zeta}}{\partial\mathbf{x}}.$$

One also has

$$\delta|\nabla\varphi| = \frac{(\nabla\varphi)^T\delta\nabla\varphi}{|\nabla\varphi|}.$$

Finally, taking the variation of  $\mathbf{n} = \nabla\varphi/|\nabla\varphi|$ , one can obtain

$$\delta\mathbf{n} = (\mathbf{n}^T\mathbf{n} - \mathbf{I})\left(\frac{\partial\boldsymbol{\zeta}}{\partial\mathbf{x}}\right)^T\mathbf{n} = -\mathbf{P}\left(\frac{\partial\boldsymbol{\zeta}}{\partial\mathbf{x}}\right)^T\mathbf{n}. \quad \square$$

*Proof of relation (13).*

$$\delta(\mathbf{F}^{-1}\mathbf{n}) = \delta(\mathbf{F}^{-1})\mathbf{n} + \mathbf{F}^{-1}\delta\mathbf{n} = -\mathbf{F}^{-1}\frac{\partial\boldsymbol{\zeta}}{\partial\mathbf{x}}\mathbf{n} + \mathbf{F}^{-1}\delta\mathbf{n}. \quad \square$$

*Proof of relation (14).*

$$\delta\left(\frac{\partial\mathbf{n}}{\partial\mathbf{x}}\right) = \delta\left(\frac{\partial\mathbf{n}}{\partial\mathbf{X}}\mathbf{F}^{-1}\right) = \frac{\partial\delta\mathbf{n}}{\partial\mathbf{X}}\mathbf{F}^{-1} + \frac{\partial\mathbf{n}}{\partial\mathbf{X}}\delta\mathbf{F}^{-1} = \frac{\partial\delta\mathbf{n}}{\partial\mathbf{x}} - \frac{\partial\mathbf{n}}{\partial\mathbf{x}}\frac{\partial\boldsymbol{\zeta}}{\partial\mathbf{x}}. \quad \square$$

We denote by  $\sigma$  the energy per unit area of surface  $S_t$ . The variation of  $\sigma$  is  $\delta\sigma$ . This variation depends on the physical problem through the dependence of  $\sigma$  on geometrical and thermodynamical parameters. For now, we do not need to know this variation in explicit form; the variation will be given further. The next lemma gives the variation of the surface potential energy [Gouin 2014a; 2014b].

**Lemma 3.** *Let us consider a material surface  $S_t$  of boundary edge  $C_t$ . The variation of surface energy*

$$E = \iint_{S_t} \sigma \, ds$$

is

$$\delta E = \iint_{S_t} [\delta\sigma - (\nabla_{\text{tg}}^T\sigma + \sigma H\mathbf{n}^T)\boldsymbol{\zeta}] \, ds + \int_{C_t} \sigma\mathbf{n}'^T\boldsymbol{\zeta} \, dl,$$

where  $ds, dl$  are the surface and line measures, respectively.<sup>1</sup>

<sup>1</sup>It is interesting to remark that the combination  $\hat{\delta}\sigma = \delta\sigma - (\nabla_{\text{tg}}^T\sigma)\boldsymbol{\zeta}$  is the variation of  $\sigma$  at fixed Eulerian coordinates. Indeed, since the symbol  $\delta$  means the variation at fixed Lagrangian coordinates, and  $\hat{\delta}$  is the variation at fixed Eulerian coordinates, this formula is a natural general relation between two types of variations [Gavrilyuk and Gouin 1999; Gavrilyuk 2011].

*Proof.* We suppose that the unit normal vector field is locally extended in the vicinity of  $S_t$ . For any vector field  $\mathbf{w}$  one has

$$\operatorname{rot}(\mathbf{n} \times \mathbf{w}) = \mathbf{n} \operatorname{div} \mathbf{w} - \mathbf{w} \operatorname{div} \mathbf{n} + \frac{\partial \mathbf{n}}{\partial \mathbf{x}} \mathbf{w} - \frac{\partial \mathbf{w}}{\partial \mathbf{x}} \mathbf{n}.$$

From relation  $\mathbf{n}^T \mathbf{n} = 1$ , we obtain  $\mathbf{n}^T \frac{\partial \mathbf{n}}{\partial \mathbf{x}} = 0$ . Using the definition of  $H$  (that is,  $H = -\operatorname{div} \mathbf{n}$ ), we deduce on  $S_t$

$$\mathbf{n}^T \operatorname{rot}(\mathbf{n} \times \mathbf{w}) = \operatorname{div} \mathbf{w} + H \mathbf{n}^T \mathbf{w} - \mathbf{n}^T \frac{\partial \mathbf{w}}{\partial \mathbf{x}} \mathbf{n}. \quad (15)$$

The surface energy is given by

$$E = \iint_{S_t} \sigma |d_1 \mathbf{x} \wedge d_2 \mathbf{x}|,$$

where  $d_i \mathbf{x} = \frac{\partial \mathbf{x}}{\partial s_i} ds_i$  ( $i = 1, 2$ ) and  $s_i$  are curvilinear coordinates on  $S_t$ . This integral can also be written as

$$E = \iint_{S_t} \sigma \det(\mathbf{n}, d_1 \mathbf{x}, d_2 \mathbf{x}) = \iint_{S_0} \sigma \det(\mathbf{F} \mathbf{F}^{-1} \mathbf{n}, \mathbf{F} d_{10} \mathbf{X}, \mathbf{F} d_{20} \mathbf{X}).$$

Here  $d_{i0} \mathbf{X} = \frac{\partial \mathbf{X}}{\partial s_{i0}} ds_{i0}$  and  $s_{i0}$  are the corresponding curvilinear coordinates on  $S_0$ . Finally,

$$E = \iint_{S_0} \sigma (\det \mathbf{F}) \det(\mathbf{F}^{-1} \mathbf{n}, d_{10} \mathbf{X}, d_{20} \mathbf{X}) = \iint_{S_0} \sigma \det((\det \mathbf{F}) \mathbf{F}^{-1} \mathbf{n}, d_{10} \mathbf{X}, d_{20} \mathbf{X}).$$

Let us remark that  $(\det \mathbf{F}) \mathbf{F}^{-1} \mathbf{n}$  is the image of  $\mathbf{n}$  and is not the normal vector to  $S_0$  because  $\mathbf{F}$  is not an orthogonal transformation.

One has

$$\delta E = \iint_{S_0} \delta \sigma \det \mathbf{F} \det(\mathbf{F}^{-1} \mathbf{n}, d_{10} \mathbf{X}, d_{20} \mathbf{X}) + \iint_{S_0} \sigma \delta (\det \mathbf{F} \det(\mathbf{F}^{-1} \mathbf{n}, d_{10} \mathbf{X}, d_{20} \mathbf{X})).$$

Using Lemma 2, one gets

$$\begin{aligned} & \iint_{S_0} \sigma \delta (\det \mathbf{F} \det(\mathbf{F}^{-1} \mathbf{n}, d_{10} \mathbf{X}, d_{20} \mathbf{X})) \\ &= \iint_{S_t} \sigma \operatorname{div} \boldsymbol{\zeta} \det(\mathbf{n}, d_1 \mathbf{x}, d_2 \mathbf{x}) + \sigma \det(\delta \mathbf{n}, d_1 \mathbf{x}, d_2 \mathbf{x}) - \sigma \det\left(\frac{\partial \boldsymbol{\zeta}}{\partial \mathbf{x}} \mathbf{n}, d_1 \mathbf{x}, d_2 \mathbf{x}\right) \\ &= \iint_{S_t} \left( \operatorname{div}(\sigma \boldsymbol{\zeta}) - (\nabla^T \sigma) \boldsymbol{\zeta} - \sigma \mathbf{n}^T \frac{\partial \boldsymbol{\zeta}}{\partial \mathbf{x}} \mathbf{n} \right) ds. \end{aligned}$$

Relation (15) yields

$$\operatorname{div}(\sigma \boldsymbol{\zeta}) + \sigma H \mathbf{n}^T \boldsymbol{\zeta} - \mathbf{n}^T \frac{\partial(\sigma \boldsymbol{\zeta})}{\partial \mathbf{x}} \mathbf{n} = \mathbf{n}^T \operatorname{rot}(\sigma \mathbf{n} \times \boldsymbol{\zeta}).$$

It implies

$$\begin{aligned} \iint_{S_0} \sigma \delta(\det \mathbf{F} \det(\mathbf{F}^{-1} \mathbf{n}, d_{10} \mathbf{X}, d_{20} \mathbf{X})) \\ = \iint_{S_t} -(\sigma H \mathbf{n}^T + (\nabla^T \sigma) \mathbf{P}) \boldsymbol{\zeta} ds + \iint_{S_t} \mathbf{n}^T \operatorname{rot}(\sigma \mathbf{n} \times \boldsymbol{\zeta}) ds. \end{aligned}$$

Since  $\mathbf{P} \nabla \sigma \equiv \nabla_{\text{tg}} \sigma$ , one has

$$\iint_{S_t} \mathbf{n}^T \operatorname{rot}(\sigma \mathbf{n} \times \boldsymbol{\zeta}) ds = \int_{C_t} \det(\mathbf{t}, \sigma \mathbf{n}, \boldsymbol{\zeta}) dl = \int_{C_t} \sigma \mathbf{n}'^T \boldsymbol{\zeta} dl,$$

and we obtain Lemma 3.  $\square$

**Lemma 4.** *Let  $\sigma$  be a function of curvature tensor  $\mathbf{R}$ , or equivalently, a function of  $H$  and  $K$ . Then,*

$$\frac{\partial \sigma}{\partial \mathbf{R}} = a \mathbf{I} + b \mathbf{R} \quad \text{with } a = \frac{\partial \sigma}{\partial H} + H \frac{\partial \sigma}{\partial K} \text{ and } b = -\frac{\partial \sigma}{\partial K}, \quad (16)$$

where for the sake of simplicity, we indifferently write  $\sigma(\mathbf{R})$  or  $\sigma(H, K)$ . In particular, this implies

$$\mathbf{n}^T \frac{\partial \sigma}{\partial \mathbf{R}} \frac{\partial \mathbf{n}}{\partial \mathbf{x}} = \mathbf{0}. \quad (17)$$

*Proof.* Since  $H = \operatorname{tr} \mathbf{R}$ ,  $2K = (\operatorname{tr} \mathbf{R})^2 - \operatorname{tr}(\mathbf{R}^2)$ , and

$$\frac{\partial \operatorname{tr}(\mathbf{R}^k)}{\partial \mathbf{R}} = k \mathbf{R}^{k-1},$$

one gets

$$\frac{\partial \sigma}{\partial \mathbf{R}} = \left( \frac{\partial \sigma}{\partial H} + H \frac{\partial \sigma}{\partial K} \right) \mathbf{I} - \frac{\partial \sigma}{\partial K} \mathbf{R}.$$

Since

$$\mathbf{R} = -\frac{\partial \mathbf{n}}{\partial \mathbf{x}} \mathbf{P} \quad \text{and} \quad \frac{\partial \sigma}{\partial \mathbf{R}} = a \mathbf{I} + b \mathbf{R}, \quad (18)$$

we obtain

$$\mathbf{n}^T \frac{\partial \sigma}{\partial \mathbf{R}} \frac{\partial \mathbf{n}}{\partial \mathbf{x}} = a \mathbf{n}^T \frac{\partial \mathbf{n}}{\partial \mathbf{x}} - b \mathbf{n}^T \left( \frac{\partial \mathbf{n}}{\partial \mathbf{x}} \right)^2 = \mathbf{0}. \quad \square$$

## 5. Variation of $\sigma$

This is a key part of the paper. The variation of the surface energy per unit area is obtained in the general case  $\sigma = \sigma(H, K)$ . The membrane is determined by a surface  $S_t$  having a closed contact line  $C_t$  on a rigid surface  $\mathcal{S} = S_1 \cup S_2$  (see Figure 1). The dependence on other parameters such as concentrations of surfactants on the membranes can further be taken into account as in [Gouin 2014a; Steigmann and Li 1995].

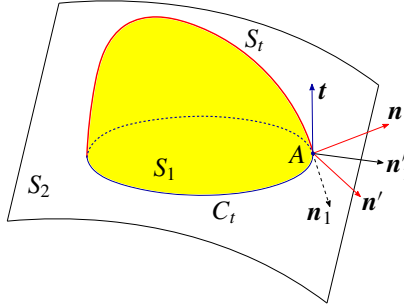


**Figure 1.** A drop lies on solid surface  $\mathcal{S} = S_1 \cup S_2$ ;  $S_t$  is a free surface;  $\mathbf{n}_1$  and  $\mathbf{n}$  are the external unit normal vectors to  $S_1$  and  $S_t$ , respectively. Contact line  $C_t$  separates  $S_1$  and  $S_2$ ,  $\mathbf{t}$  is the unit tangent vector to  $C_t$  on  $\mathcal{S}$ . Vectors  $\mathbf{n}'_1 = \mathbf{n}_1 \times \mathbf{t}$  and  $\mathbf{n}' = \mathbf{t} \times \mathbf{n}$  are the binormals to  $C_t$  relative to  $\mathcal{S}$  and  $S_t$  at point  $A$  of  $C_t$ , respectively.

**Lemma 5.** *The variation of surface energy  $\sigma(\mathbf{R})$  is given by the relation*

$$\delta\sigma = -\operatorname{div}_{\text{tg}}\left(\frac{\partial\sigma}{\partial\mathbf{R}}\mathbf{R}\zeta + \mathbf{P}\frac{\partial\sigma}{\partial\mathbf{R}}\delta\mathbf{n}\right) + \operatorname{div}_{\text{tg}}\left(\frac{\partial\sigma}{\partial\mathbf{R}}\mathbf{R}\right)\zeta + \operatorname{div}_{\text{tg}}\left(\mathbf{P}\frac{\partial\sigma}{\partial\mathbf{R}}\right)\delta\mathbf{n}. \quad (19)$$

*Proof.* Using Lemma 2, we have

$$\delta\mathbf{R} = -\delta\left(\frac{\partial\mathbf{n}}{\partial\mathbf{x}}\mathbf{P}\right) = -\left(\frac{\partial\delta\mathbf{n}}{\partial\mathbf{x}} - \frac{\partial\mathbf{n}}{\partial\mathbf{x}}\frac{\partial\zeta}{\partial\mathbf{x}}\right)\mathbf{P} + \frac{\partial\mathbf{n}}{\partial\mathbf{x}}\delta(\mathbf{nn}^T).$$

By taking account of (12) and  $\delta(\mathbf{nn}^T) = \delta\mathbf{nn}^T + \mathbf{n}\delta\mathbf{n}^T$ , we get

$$\delta\mathbf{R} = -\frac{\partial\delta\mathbf{n}}{\partial\mathbf{x}}\mathbf{P} + \frac{\partial\mathbf{n}}{\partial\mathbf{x}}\frac{\partial\zeta}{\partial\mathbf{x}}\mathbf{P} - \frac{\partial\mathbf{n}}{\partial\mathbf{x}}\mathbf{P}\left(\frac{\partial\zeta}{\partial\mathbf{x}}\right)^T\mathbf{nn}^T - \frac{\partial\mathbf{n}}{\partial\mathbf{x}}\mathbf{nn}^T\frac{\partial\zeta}{\partial\mathbf{x}}\mathbf{P}.$$

We deduce

$$\begin{aligned} \delta\sigma &= \operatorname{tr}\left(\frac{\partial\sigma}{\partial\mathbf{R}}\delta\mathbf{R}\right) \\ &= \operatorname{tr}\left[\frac{\partial\sigma}{\partial\mathbf{R}}\left(-\frac{\partial\delta\mathbf{n}}{\partial\mathbf{x}}\mathbf{P} + \frac{\partial\mathbf{n}}{\partial\mathbf{x}}\frac{\partial\zeta}{\partial\mathbf{x}}\mathbf{P} - \frac{\partial\mathbf{n}}{\partial\mathbf{x}}\mathbf{P}\left(\frac{\partial\zeta}{\partial\mathbf{x}}\right)^T\mathbf{nn}^T - \frac{\partial\mathbf{n}}{\partial\mathbf{x}}\mathbf{nn}^T\frac{\partial\zeta}{\partial\mathbf{x}}\mathbf{P}\right)\right]. \end{aligned}$$

From (17), we get  $\mathbf{nn}^T\frac{\partial\sigma}{\partial\mathbf{R}}\frac{\partial\mathbf{n}}{\partial\mathbf{x}}\frac{\partial\zeta}{\partial\mathbf{x}} = 0$  and  $\mathbf{nn}^T\frac{\partial\sigma}{\partial\mathbf{R}}\frac{\partial\mathbf{n}}{\partial\mathbf{x}}\mathbf{nn}^T\frac{\partial\zeta}{\partial\mathbf{x}} = 0$ .

Consequently,  $\frac{\partial\sigma}{\partial\mathbf{R}}\frac{\partial\mathbf{n}}{\partial\mathbf{x}}\mathbf{P}\frac{\partial\zeta}{\partial\mathbf{x}} = -\frac{\partial\sigma}{\partial\mathbf{R}}\mathbf{R}\frac{\partial\zeta}{\partial\mathbf{x}}$ , which implies

$$\begin{aligned} \delta\sigma &= -\operatorname{tr}\left[\mathbf{P}\frac{\partial\sigma}{\partial\mathbf{R}}\frac{\partial\delta\mathbf{n}}{\partial\mathbf{x}} + \frac{\partial\sigma}{\partial\mathbf{R}}\mathbf{R}\frac{\partial\zeta}{\partial\mathbf{x}}\right] \\ &= -\operatorname{div}\left(\mathbf{P}\frac{\partial\sigma}{\partial\mathbf{R}}\delta\mathbf{n}\right) + \operatorname{div}\left(\mathbf{P}\frac{\partial\sigma}{\partial\mathbf{R}}\right)\delta\mathbf{n} - \operatorname{div}\left(\frac{\partial\sigma}{\partial\mathbf{R}}\mathbf{R}\zeta\right) + \operatorname{div}\left(\frac{\partial\sigma}{\partial\mathbf{R}}\mathbf{R}\right)\zeta. \end{aligned}$$

By taking account of (5), we get

$$\delta\sigma = -\operatorname{div}_{\text{tg}}\left(\mathbf{P}\frac{\partial\sigma}{\partial\mathbf{R}}\delta\mathbf{n}\right) + \operatorname{div}_{\text{tg}}\left(\mathbf{P}\frac{\partial\sigma}{\partial\mathbf{R}}\right)\delta\mathbf{n} - \operatorname{div}_{\text{tg}}\left(\frac{\partial\sigma}{\partial\mathbf{R}}\mathbf{R}\zeta\right) + \operatorname{div}_{\text{tg}}\left(\frac{\partial\sigma}{\partial\mathbf{R}}\mathbf{R}\right)\zeta,$$

and relation (19) is proven.  $\square$

Now, we have to study term  $\operatorname{div}_{\text{tg}}\left(\mathbf{P}\frac{\partial\sigma}{\partial\mathbf{R}}\right)\delta\mathbf{n}$ .

**Lemma 6.** 
$$\operatorname{div}_{\text{tg}}\left(\mathbf{P}\frac{\partial\sigma}{\partial\mathbf{R}}\right)\delta\mathbf{n} = -\operatorname{div}_{\text{tg}}\left[\mathbf{P}\operatorname{div}_{\text{tg}}^T\left(\mathbf{P}\frac{\partial\sigma}{\partial\mathbf{R}}\right)\mathbf{n}^T\zeta\right] \\ + \operatorname{div}_{\text{tg}}\left[\mathbf{P}\operatorname{div}_{\text{tg}}^T\left(\mathbf{P}\frac{\partial\sigma}{\partial\mathbf{R}}\right)\right]\mathbf{n}^T\zeta - \operatorname{div}_{\text{tg}}\left(\mathbf{P}\frac{\partial\sigma}{\partial\mathbf{R}}\right)\mathbf{R}\zeta.$$

*Proof.* Using relation (12), one obtains

$$\begin{aligned} \operatorname{div}_{\text{tg}}\left(\mathbf{P}\frac{\partial\sigma}{\partial\mathbf{R}}\right)\delta\mathbf{n} &= -\operatorname{div}_{\text{tg}}\left(\mathbf{P}\frac{\partial\sigma}{\partial\mathbf{R}}\right)\mathbf{P}\left(\frac{\partial\zeta}{\partial\mathbf{x}}\right)^T\mathbf{n} \\ &= -\operatorname{div}_{\text{tg}}\left(\mathbf{P}\frac{\partial\sigma}{\partial\mathbf{R}}\right)\mathbf{P}\left[\left(\frac{\partial(\mathbf{n}^T\zeta)}{\partial\mathbf{x}}\right)^T - \left(\frac{\partial\mathbf{n}}{\partial\mathbf{x}}\right)^T\zeta\right] \\ &= -\operatorname{div}_{\text{tg}}\left(\mathbf{P}\frac{\partial\sigma}{\partial\mathbf{R}}\right)\nabla_{\text{tg}}(\mathbf{n}^T\zeta) - \operatorname{div}_{\text{tg}}\left(\mathbf{P}\frac{\partial\sigma}{\partial\mathbf{R}}\right)\mathbf{R}\zeta \\ &= \operatorname{div}_{\text{tg}}\left[\mathbf{P}\operatorname{div}_{\text{tg}}^T\left(\mathbf{P}\frac{\partial\sigma}{\partial\mathbf{R}}\right)\right]\mathbf{n}^T\zeta - \operatorname{div}_{\text{tg}}\left(\mathbf{P}\frac{\partial\sigma}{\partial\mathbf{R}}\right)\mathbf{R}\zeta \\ &\quad - \operatorname{div}_{\text{tg}}\left[\mathbf{P}\operatorname{div}_{\text{tg}}^T\left(\mathbf{P}\frac{\partial\sigma}{\partial\mathbf{R}}\right)\mathbf{n}^T\zeta\right]. \quad \square \end{aligned}$$

Now, from Lemma 3 and (19), we obtain the following fundamental lemma.

**Lemma 7.** *The variation of surface energy  $E = \iint_{S_t} \sigma ds$ , where  $S_t$  has an oriented boundary line  $C_t$  with tangent unit vector  $\mathbf{t}$  and binormal unit vector  $\mathbf{n}' = \mathbf{t} \times \mathbf{n}$ , is given by the relation*

$$\begin{aligned} \delta E &= \iint_{S_t} \left[ \operatorname{div}_{\text{tg}}\left(\frac{\partial\sigma}{\partial\mathbf{R}}\mathbf{R}\right) - \operatorname{div}_{\text{tg}}\left(\mathbf{P}\frac{\partial\sigma}{\partial\mathbf{R}}\right)\mathbf{R} + \operatorname{div}_{\text{tg}}\left(\mathbf{P}\operatorname{div}_{\text{tg}}^T\left(\mathbf{P}\frac{\partial\sigma}{\partial\mathbf{R}}\right)\right)\mathbf{n}^T \right. \\ &\quad \left. - \sigma H\mathbf{n}^T - \nabla_{\text{tg}}^T\sigma \right] \zeta ds \\ &\quad + \int_{C_t} \mathbf{n}'^T \left\{ \left[ \sigma\mathbf{I} - \frac{\partial\sigma}{\partial\mathbf{R}}\mathbf{R} - \operatorname{div}_{\text{tg}}^T\left(\mathbf{P}\frac{\partial\sigma}{\partial\mathbf{R}}\right)\mathbf{n}^T \right] \zeta + \frac{\partial\sigma}{\partial\mathbf{R}}\mathbf{P}\left(\frac{\partial\zeta}{\partial\mathbf{x}}\right)^T\mathbf{n} \right\} dl. \end{aligned}$$

*Proof.* By taking account of Lemmas 5 and 6, we get

$$\begin{aligned} \delta\sigma &= -\operatorname{div}_{\text{tg}}\left[\frac{\partial\sigma}{\partial\mathbf{R}}\mathbf{R}\zeta + \mathbf{P}\frac{\partial\sigma}{\partial\mathbf{R}}\delta\mathbf{n} + \mathbf{P}\operatorname{div}_{\text{tg}}^T\left(\mathbf{P}\frac{\partial\sigma}{\partial\mathbf{R}}\right)\mathbf{n}^T\zeta\right] \\ &\quad + \left[ \operatorname{div}_{\text{tg}}\left(\frac{\partial\sigma}{\partial\mathbf{R}}\mathbf{R}\right) - \operatorname{div}_{\text{tg}}\left(\mathbf{P}\frac{\partial\sigma}{\partial\mathbf{R}}\right)\mathbf{R} + \operatorname{div}_{\text{tg}}\left(\mathbf{P}\operatorname{div}_{\text{tg}}^T\left(\mathbf{P}\frac{\partial\sigma}{\partial\mathbf{R}}\right)\right)\mathbf{n}^T \right] \zeta. \end{aligned}$$

By using (6) and Lemma 3 associated with the Stokes formula, and property  $\mathbf{n}'^T \mathbf{P} = \mathbf{n}^T$ , we obtain

$$\begin{aligned} \delta E = \iint_{S_t} & \left[ \operatorname{div}_{\operatorname{tg}} \left( \frac{\partial \sigma}{\partial \mathbf{R}} \mathbf{R} \right) - \operatorname{div}_{\operatorname{tg}} \left( \mathbf{P} \frac{\partial \sigma}{\partial \mathbf{R}} \right) \mathbf{R} + \operatorname{div}_{\operatorname{tg}} \left( \mathbf{P} \operatorname{div}_{\operatorname{tg}}^T \left( \mathbf{P} \frac{\partial \sigma}{\partial \mathbf{R}} \right) \right) \mathbf{n}^T \right. \\ & \left. - \sigma H \mathbf{n}^T - \nabla_{\operatorname{tg}}^T \sigma \right] \boldsymbol{\zeta} ds \\ & + \int_{C_t} \mathbf{n}^T \left\{ \left[ \sigma \mathbf{I} - \frac{\partial \sigma}{\partial \mathbf{R}} \mathbf{R} - \operatorname{div}_{\operatorname{tg}}^T \left( \mathbf{P} \frac{\partial \sigma}{\partial \mathbf{R}} \right) \mathbf{n}^T \right] \boldsymbol{\zeta} - \frac{\partial \sigma}{\partial \mathbf{R}} \delta \mathbf{n} \right\} dl. \end{aligned}$$

From Lemma 2 we deduce

$$-\mathbf{n}'^T \frac{\partial \sigma}{\partial \mathbf{R}} \delta \mathbf{n} = \mathbf{n}'^T \frac{\partial \sigma}{\partial \mathbf{R}} \mathbf{P} \left( \frac{\partial \boldsymbol{\zeta}}{\partial \mathbf{x}} \right)^T \mathbf{n},$$

which proves Lemma 7.  $\square$

## 6. Equations of motion and shape equation

The vesicle occupies domain  $D_t$  with a free boundary  $S_t$  which is the membrane surface, and  $S_1$  which belongs to the rigid surface  $\mathcal{S} = S_1 \cup S_2$ .  $S_1$  denotes the footprint of  $D_t$  on  $\mathcal{S}$ , and  $C_t$  is the closed edge (contact line) between  $S_1$  and  $S_2$  (see Figure 1).

We denote by  $\mathbf{n}_1$  the external unit normal to  $S_1$  along contact line  $C_t$ . Then denoting  $\mathbf{t}_1 = -\mathbf{t}$ , one has

$$\mathbf{n}'_1 = \mathbf{t}_1 \times \mathbf{n}_1 = \mathbf{n}_1 \times \mathbf{t}.$$

The surface energy of membrane  $S_t$  is denoted  $\sigma$ . Solid surfaces  $S_1$  and  $S_2$  have constant surface energies denoted  $\sigma_1$  and  $\sigma_2$ . The geometrical notations are shown in Figure 1.

One can formulate the virtual work principle in the form [Germain 1973; Gouin 2007]

$$\delta \mathcal{A}_e + \delta \mathcal{A}_i - \delta \mathcal{E} = 0,$$

where  $\delta \mathcal{A}_e$  is the virtual work of external forces,  $\delta \mathcal{A}_i$  is the virtual work of inertial forces, and  $\delta \mathcal{E}$  is the variation of the total energy. The energy  $\mathcal{E}$  is taken in the form

$$\mathcal{E} = \iiint_{D_t} \rho \varepsilon dv + \iint_{S_t} \sigma ds + \iint_{S_1} \sigma_1 ds,$$

where specific internal energy  $\varepsilon$  is a function of density  $\rho$ . As we mentioned before, one can also include in this dependence several scalar quantities which are transported by the flow (specific entropy, mass fractions of surfactants, etc.). From

Lemma 2, (11), and the mass conservation law

$$\rho \det \mathbf{F} = \rho_0(\mathbf{X}),$$

we obtain the variation of the specific energy and density at fixed Lagrangian coordinates in the form

$$\delta \varepsilon = \frac{p}{\rho^2} \delta \rho \quad \text{with } \delta \rho = -\rho \operatorname{div} \boldsymbol{\zeta},$$

where  $p$  is the thermodynamical pressure. Consequently, the variation of the first term is [Berdichevsky 2009; Gavrilyuk 2011; Serrin 1959]

$$\begin{aligned} \delta \iiint_{D_t} \rho \varepsilon \, dv &= \delta \iiint_{D_0} \rho_0 \varepsilon \, dv_0 = \iiint_{D_0} \rho_0 \delta \varepsilon \, dv_0 \\ &= \iiint_{D_t} \rho \delta \varepsilon \, dv = - \iiint_{D_t} p \operatorname{div} \boldsymbol{\zeta} \, dv. \end{aligned}$$

The variation of the surface energy is given in Lemma 3. The third term is the surface energy of  $S_1$  with energy  $\sigma_1$  per unit surface. The virtual work of the external forces is given in the form

$$\delta \mathcal{A}_e = \iiint_{D_t} \rho \mathbf{f}^T \boldsymbol{\zeta} \, dv + \iint_{S_t} \mathbf{T}^T \boldsymbol{\zeta} \, ds + \int_{C_t} \sigma_2 \mathbf{n}'^T \boldsymbol{\zeta} \, ds,$$

where  $\rho \mathbf{f}$  is the volume external force in  $D_t$ ,  $\mathbf{T}$  is the external stress vector at the free surface  $S_t$ , and  $\sigma_2 \mathbf{n}'_1$  is the line tension vector exerted on  $C_t$ . The last term on the right-hand side comes from Lemma 3 which can be also applied for rigid surfaces. Finally,

$$\delta \mathcal{A}_i = - \iiint_{D_t} \rho \mathbf{a}^T \boldsymbol{\zeta} \, dv$$

is the virtual work of inertial force, where  $\mathbf{a}$  is the acceleration. The virtual work of forces  $\delta \mathcal{T}$  applied to the material volume  $D_t$  is defined as

$$\begin{aligned} \delta \mathcal{T} &= \iiint_{D_t} (-\rho \mathbf{a}^T + \rho \mathbf{f}^T - \nabla^T p) \boldsymbol{\zeta} \, dv + \iint_{S_1} (p + H_1 \sigma_1) \mathbf{n}'_1{}^T \boldsymbol{\zeta} \, ds \\ &\quad + \iint_{S_t} \left[ -\operatorname{div}_{\text{tg}} \left( \frac{\partial \sigma}{\partial \mathbf{R}} \mathbf{R} \right) + \operatorname{div}_{\text{tg}} \left( \mathbf{P} \frac{\partial \sigma}{\partial \mathbf{R}} \right) \mathbf{R} \right. \\ &\quad \quad \left. - \operatorname{div}_{\text{tg}} \left( \mathbf{P} \operatorname{div}_{\text{tg}}^T \left( \mathbf{P} \frac{\partial \sigma}{\partial \mathbf{R}} \right) \right) \mathbf{n}^T + (p + H \sigma) \mathbf{n}^T + \nabla_{\text{tg}}^T \sigma + \mathbf{T}^T \right] \boldsymbol{\zeta} \, ds \\ &\quad - \int_{C_t} \left\{ \left[ (\sigma_1 - \sigma_2) \mathbf{n}'_1{}^T + \sigma \mathbf{n}'^T - \mathbf{n}'^T \operatorname{div}_{\text{tg}}^T \left( \mathbf{P} \frac{\partial \sigma}{\partial \mathbf{R}} \right) \mathbf{n}^T - \mathbf{n}'^T \frac{\partial \sigma}{\partial \mathbf{R}} \mathbf{R} \right] \boldsymbol{\zeta} \right. \\ &\quad \quad \left. + \mathbf{n}'^T \frac{\partial \sigma}{\partial \mathbf{R}} \mathbf{P} \left( \frac{\partial \boldsymbol{\zeta}}{\partial \mathbf{x}} \right)^T \mathbf{n} \right\} dl. \end{aligned} \tag{20}$$

As usual,  $H_1$  and  $H$  are the sum of principle curvatures of surfaces  $S_1$  and  $S_t$ , respectively. Terms on  $D_t$ ,  $S_1$ ,  $S_t$  are in separable form with respect to the field  $\boldsymbol{\zeta}$ . Expression (20) implies the equation of motion in  $D_t$  and boundary conditions on surfaces  $S_1$ ,  $S_t$  [Schwartz 1966, Chapitre 3]. Virtual displacement  $\boldsymbol{\zeta}$  must be compatible with conditions of the problem; for example,  $S_1$  is an external surface to domain  $D_t$  and consequently  $\boldsymbol{\zeta}$  must be tangent to  $S_1$ . This notion is developed in [Berdichevsky 2009]. They are presented below.

**6.1. Equation of motion.** We consider virtual displacements  $\boldsymbol{\zeta}$  which vanish on the boundary of  $D_t$ . The fundamental lemma of virtual displacements yields

$$\rho \mathbf{a} + \nabla p = \rho \mathbf{f}, \quad (21)$$

which is the classical Newton law in continuum mechanics.

**6.2. Condition on surface  $S_1$ .** Due to the fact that the surface  $S_1$  is — a priori — given, the virtual displacements must be compatible with the geometry of  $S_1$ . This means that the nonpenetration condition (slip condition) is verified:

$$\mathbf{n}_1^T \boldsymbol{\zeta} = 0. \quad (22)$$

Constraint (22) is equivalent to the introduction of a Lagrange multiplier  $\mathcal{P}_1$  into (20) where  $\boldsymbol{\zeta}$  is now a virtual displacement without constraint. The corresponding term on  $S_1$  will be modified into

$$\iint_{S_1} (p + H_1 \sigma_1 - \mathcal{P}_1) \mathbf{n}_1^T \boldsymbol{\zeta} \, ds.$$

Since the variation of  $\boldsymbol{\zeta}$  on  $S_1$  is independent, (20) implies

$$\mathcal{P}_1 = p + H_1 \sigma_1. \quad (23)$$

This is the classical Laplace condition allowing us to obtain the normal stress component  $\mathcal{P}_1 \mathbf{n}_1$  exerted by surface  $S_1$ .

**6.3. Extended shape equation.** Taking account of (21) and (23), for all displacement  $\boldsymbol{\zeta}$  on moving membrane  $S_t$ , one has from (20)

$$\iint_{S_t} \left[ -\operatorname{div}_{\text{tg}} \left( \frac{\partial \sigma}{\partial \mathbf{R}} \mathbf{R} \right) + \operatorname{div}_{\text{tg}} \left( \mathbf{P} \frac{\partial \sigma}{\partial \mathbf{R}} \right) \mathbf{R} - \operatorname{div}_{\text{tg}} \left( \mathbf{P} \operatorname{div}_{\text{tg}}^T \left( \mathbf{P} \frac{\partial \sigma}{\partial \mathbf{R}} \right) \right) \mathbf{n}^T + (p + H \sigma) \mathbf{n}^T + \nabla_{\text{tg}}^T \sigma + \mathbf{T}^T \right] \boldsymbol{\zeta} \, ds = 0.$$

It implies

$$\left\{ p + H\sigma - \operatorname{div}_{\text{tg}} \left[ \mathbf{P} \operatorname{div}_{\text{tg}}^T \left( \mathbf{P} \frac{\partial \sigma}{\partial \mathbf{R}} \right) \right] \right\} \mathbf{n} \\ + \nabla_{\text{tg}} \sigma - \operatorname{div}_{\text{tg}}^T \left( \frac{\partial \sigma}{\partial \mathbf{R}} \mathbf{R} \right) + \mathbf{R} \operatorname{div}_{\text{tg}}^T \left( \mathbf{P} \frac{\partial \sigma}{\partial \mathbf{R}} \right) + \mathbf{T} = 0. \quad (24)$$

Equation (24) is the most general form of the dynamical boundary condition on  $S_t$ . Due to the fact that surface energy  $\sigma$  must be an isotropic function of curvature tensor  $\mathbf{R}$ , i.e., a function of two invariants  $H$  and  $K$ , we obtain (for proof, see the Appendix) that the vector

$$\nabla_{\text{tg}} \sigma - \operatorname{div}_{\text{tg}}^T \left( \frac{\partial \sigma}{\partial \mathbf{R}} \mathbf{R} \right) + \mathbf{R} \operatorname{div}_{\text{tg}}^T \left( \mathbf{P} \frac{\partial \sigma}{\partial \mathbf{R}} \right)$$

is normal to  $S_t$  and consequently  $\mathbf{T}$  can be written in the form

$$\mathbf{T} = -\mathcal{P} \mathbf{n}.$$

Here scalar  $\mathcal{P}$  has the dimension of pressure.

One obtains from (44) (see the Appendix)

$$H\sigma - \Delta_{\text{tg}} a - b \Delta_{\text{tg}} H - \nabla_{\text{tg}}^T b \nabla_{\text{tg}} H - \operatorname{div}_{\text{tg}} (\mathbf{R} \nabla_{\text{tg}} b) \\ + (2K - H^2) \frac{\partial \sigma}{\partial H} - HK \frac{\partial \sigma}{\partial K} = \mathcal{P} - p. \quad (25)$$

Relation (25) is the normal component of (24).

It is important to underline that (24) is only expressed in the normal direction to  $S_t$ . This is not the case when surface energy  $\sigma$  also depends on physicochemical characteristics of  $S_t$ , such as temperature or surfactants. In this last case, Marangoni effects can appear producing additive tangential terms to  $S_t$ .

Using Lemma 1 (second equation) and expressions of scalars  $a$  and  $b$  given by (16), we get the *extended shape equation*:

$$H \left( \sigma - K \frac{\partial \sigma}{\partial K} \right) + (2K - H^2) \frac{\partial \sigma}{\partial H} - \Delta_{\text{tg}} \frac{\partial \sigma}{\partial H} - H \Delta_{\text{tg}} \frac{\partial \sigma}{\partial K} \\ - \nabla_{\text{tg}}^T H \nabla_{\text{tg}} \frac{\partial \sigma}{\partial K} + \operatorname{div}_{\text{tg}} \left( \mathbf{R} \nabla_{\text{tg}} \frac{\partial \sigma}{\partial K} \right) = \mathcal{P} - p. \quad (26)$$

Equation (26) was also derived in [Rosso and Virga 1999] under the hypothesis (10) and the assumption of inextensibility of the membrane. Our derivation does not use these hypotheses. For example, the inextensibility property is not natural even in the case of incompressible fluids (at fixed volume, the surface of a three-dimensional body may vary).

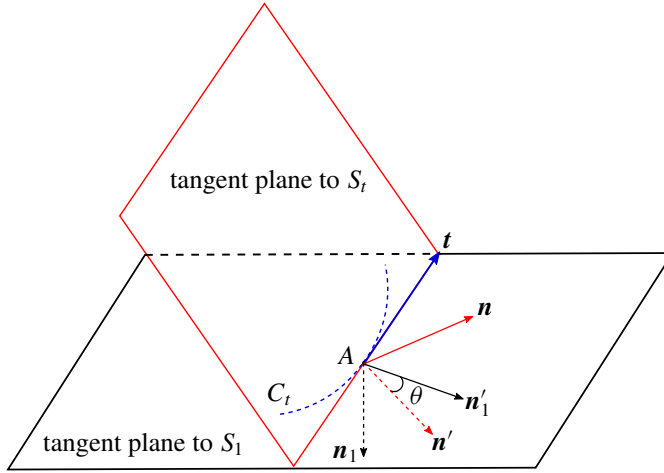


**Figure 2.** Tangent planes to membrane  $S_t$  and solid surface  $S_1$ :  $\mathbf{n}_1$  and  $\mathbf{n}$  are the unit normal vectors to  $\mathcal{S}$  and  $S_t$ , external to the domain of the vesicle; contact line  $C_t$  is shared between  $\mathcal{S}$  and  $S_t$  and  $\mathbf{t}$  is the unit tangent vector to  $C_t$  relative to  $\mathbf{n}$ ;  $\mathbf{n}'_1 = \mathbf{n}_1 \times \mathbf{t}$  and  $\mathbf{n}' = \mathbf{t} \times \mathbf{n}$  are binormals to  $C_t$  relative to  $\mathcal{S}$  and  $S_t$  at point  $A$ , respectively. Angle  $\theta = \langle \mathbf{n}', \mathbf{n}'_1 \rangle$ . The normal plane to  $C_t$  at  $A$  contains vectors  $\mathbf{n}, \mathbf{n}', \mathbf{n}_1, \mathbf{n}'_1$ .

**6.4. Helfrich's shape equation.** The Helfrich energy is given by (1). The shape equation (26) can immediately be written in the form

$$\sigma_0 H + \frac{\kappa}{2} (H - H_0) [4K - H(H + H_0)] - \kappa \Delta_{\text{tg}} H = \mathcal{P} - p, \quad (27)$$

which is the classical form obtained by Helfrich.<sup>2</sup>

### 7. Extended Young–Dupré condition on contact line $C_t$

Let us denote by  $\theta = \langle \mathbf{n}', \mathbf{n}'_1 \rangle = \pi + \langle \mathbf{n}, \mathbf{n}_1 \rangle \pmod{2\pi}$  the Young angle between  $S_1$  and  $S_t$  (see Figure 2).

Due to the fact that  $C_t$  belongs to  $S_1$ , the virtual displacement on  $C_t$  is in the form

$$\boldsymbol{\zeta} = \alpha \mathbf{t} + \beta \mathbf{n}'_1, \quad (28)$$

<sup>2</sup>Let us note that Helfrich considered the vesicle as an incompressible fluid. He also assumed that the membrane has a total constant area. Then, the virtual work can be expressed as

$$\delta \mathcal{T} = \iiint_D \rho \mathbf{f}^T \boldsymbol{\zeta} \, dv + \iint_S \mathbf{T}^T \boldsymbol{\zeta} \, ds - \delta \iint_S \sigma \, ds + \lambda_0 \delta \iint_S ds + \delta \iiint_D p \operatorname{div} \boldsymbol{\zeta} \, dv,$$

where the scalar  $\lambda_0$  is a constant Lagrange multiplier and  $p$  is a distributed Lagrange multiplier. The “shape equation” is similar to (27).

where  $\alpha$  and  $\beta$  are two scalar fields defined on  $S_1$ . Let us remark that condition (28) expresses the nonpenetration condition (22) on  $S_1$ . Moreover, since  $\mathbf{n}$ ,  $\mathbf{n}_1$ ,  $\mathbf{n}'_1$  belong to the normal plane to  $C_i$  at  $A$  (see Figure 2), one has

$$\mathbf{n} = \mathbf{n}'_1 \sin \theta - \mathbf{n}_1 \cos \theta. \quad (29)$$

But relation  $\boldsymbol{\zeta}^T \mathbf{n}_1 = 0$  implies

$$\mathbf{P} \left( \frac{\partial \boldsymbol{\zeta}}{\partial \mathbf{x}} \right)^T \mathbf{n}_1 + \mathbf{P} \left( \frac{\partial \mathbf{n}_1}{\partial \mathbf{x}} \right)^T \boldsymbol{\zeta} = 0.$$

Replacing (29) into (20) one has

$$\begin{aligned} \delta \mathcal{F} &= - \int_{C_i} \left\{ \left[ (\sigma_1 - \sigma_2) \mathbf{n}'_1{}^T + \sigma \mathbf{n}'^T - \mathbf{n}'^T \operatorname{div}_{\text{tg}}^T \left( \mathbf{P} \frac{\partial \sigma}{\partial \mathbf{R}} \right) \mathbf{n}^T - \mathbf{n}'^T \frac{\partial \sigma}{\partial \mathbf{R}} \mathbf{R} \right] \boldsymbol{\zeta} \right. \\ &\quad \left. + \mathbf{n}'^T \frac{\partial \sigma}{\partial \mathbf{R}} \mathbf{P} \left( \frac{\partial \boldsymbol{\zeta}}{\partial \mathbf{x}} \right)^T \mathbf{n} \right\} dl \\ &= - \int_{C_i} \left\{ \left[ (\sigma_1 - \sigma_2) \mathbf{n}'_1{}^T + \sigma \mathbf{n}'^T - \mathbf{n}'^T \operatorname{div}_{\text{tg}}^T \left( \mathbf{P} \frac{\partial \sigma}{\partial \mathbf{R}} \right) \mathbf{n}^T - \mathbf{n}'^T \frac{\partial \sigma}{\partial \mathbf{R}} \mathbf{R} \right. \right. \\ &\quad \left. \left. + \cos \theta \mathbf{n}'^T \frac{\partial \sigma}{\partial \mathbf{R}} \mathbf{P} \left( \frac{\partial \mathbf{n}_1}{\partial \mathbf{x}} \right)^T \right] \boldsymbol{\zeta} \right. \\ &\quad \left. + \sin \theta \mathbf{n}'^T \frac{\partial \sigma}{\partial \mathbf{R}} \mathbf{P} \left( \frac{\partial \boldsymbol{\zeta}}{\partial \mathbf{x}} \right)^T \mathbf{n}'_1 \right\} dl = 0. \end{aligned} \quad (30)$$

We choose now the virtual displacement in the form  $\boldsymbol{\zeta} = \beta \mathbf{n}'_1$ . One has

$$\frac{\partial \boldsymbol{\zeta}}{\partial \mathbf{x}} = \mathbf{n}'_1 (\nabla \beta)^T + \beta \frac{\partial \mathbf{n}'_1}{\partial \mathbf{x}}, \quad \left( \frac{\partial \boldsymbol{\zeta}}{\partial \mathbf{x}} \right)^T = \nabla \beta \mathbf{n}'_1{}^T + \beta \left( \frac{\partial \mathbf{n}'_1}{\partial \mathbf{x}} \right)^T.$$

Since  $\left( \frac{\partial \mathbf{n}'_1}{\partial \mathbf{x}} \right)^T \mathbf{n}'_1 = 0$ , it implies

$$\left( \frac{\partial \boldsymbol{\zeta}}{\partial \mathbf{x}} \right)^T \mathbf{n}'_1 = \nabla \beta.$$

The integral (30) becomes

$$\begin{aligned} \int_{C_i} \left\{ \left[ (\sigma_1 - \sigma_2) \mathbf{n}'_1{}^T + \sigma \mathbf{n}'^T - \mathbf{n}'^T \operatorname{div}_{\text{tg}}^T \left( \mathbf{P} \frac{\partial \sigma}{\partial \mathbf{R}} \right) \mathbf{n}^T - \mathbf{n}'^T \frac{\partial \sigma}{\partial \mathbf{R}} \mathbf{R} \right. \right. \\ \left. \left. + \cos \theta \mathbf{n}'^T \frac{\partial \sigma}{\partial \mathbf{R}} \mathbf{P} \left( \frac{\partial \mathbf{n}_1}{\partial \mathbf{x}} \right)^T \right] \mathbf{n}'_1 \beta + \sin \theta \mathbf{n}'^T \frac{\partial \sigma}{\partial \mathbf{R}} \mathbf{P} \nabla \beta \right\} dl = 0. \end{aligned} \quad (31)$$

Since  $\beta$  and the components of  $\nabla\beta$  can be chosen as independent, relation (31) implies two boundary conditions. The first condition on line  $C_t$  is

$$\sin\theta \mathbf{n}'^T \frac{\partial\sigma}{\partial\mathbf{R}} \mathbf{P} = 0. \quad (32)$$

The second condition is

$$\left[ (\sigma_1 - \sigma_2) \mathbf{n}'_1{}^T + \sigma \mathbf{n}'^T - \mathbf{n}'^T \operatorname{div}_{\operatorname{tg}}^T \left( \mathbf{P} \frac{\partial\sigma}{\partial\mathbf{R}} \right) \mathbf{n}^T - \mathbf{n}'^T \frac{\partial\sigma}{\partial\mathbf{R}} \mathbf{R} + \cos\theta \mathbf{n}'^T \frac{\partial\sigma}{\partial\mathbf{R}} \mathbf{P} \left( \frac{\partial\mathbf{n}_1}{\partial\mathbf{x}} \right)^T \right] \mathbf{n}'_1 = 0. \quad (33)$$

The case  $\sin\theta = 0$  all along  $C_t$  is degenerate. If  $\theta = 0$ , this corresponds to a hydrophobic surface (the contact line is absent). If  $\theta = \pi$ , this corresponds to a complete wetting. In the last case  $\mathbf{n}'_1 = -\mathbf{n}'$ ,  $\mathbf{n}_1 = \mathbf{n}$ , and the condition (33) becomes trivial:  $\sigma_1 - \sigma_2 - \sigma = 0$ .

The general case corresponds to the partial wetting ( $\sin\theta \neq 0$ ). Due to (18),

$$\mathbf{n}'^T \frac{\partial\sigma}{\partial\mathbf{R}} \mathbf{P} \equiv \mathbf{n}'^T (a\mathbf{I} + b\mathbf{R}) \mathbf{P} \equiv a\mathbf{n}'^T + b\mathbf{n}'^T \mathbf{R} \equiv \mathbf{n}'^T \frac{\partial\sigma}{\partial\mathbf{R}}.$$

Hence, (32) yields

$$\mathbf{n}'^T \frac{\partial\sigma}{\partial\mathbf{R}} = 0. \quad (34)$$

Equation (34) implies (see Lemma 4)

$$\mathbf{n}'^T \left[ \left( \frac{\partial\sigma}{\partial H} + H \frac{\partial\sigma}{\partial K} \right) \mathbf{I} - \frac{\partial\sigma}{\partial K} \mathbf{R} \right] = 0.$$

Consequently,  $\mathbf{n}'$  is an eigenvector of  $\mathbf{R}$ . We denote by  $c_{n'}$  the associated eigenvalue  $c_2$ . Then

$$\frac{\partial\sigma}{\partial H} + H \frac{\partial\sigma}{\partial K} = c_{n'} \frac{\partial\sigma}{\partial K}. \quad (35)$$

Due to the fact that  $\mathbf{t}$  is also an eigenvector of  $\mathbf{R}$  with eigenvalue  $c_t = c_1$  ( $\mathbf{t}$  and  $\mathbf{n}'$  form the eigenbasis of  $\mathbf{R}$  along  $C_t$ ), we get  $H = c_t + c_{n'}$  and the equivalent to the boundary condition (35) in the form

$$\frac{\partial\sigma}{\partial H} + c_t \frac{\partial\sigma}{\partial K} = 0. \quad (36)$$

From Lemma 4, (16), we immediately deduce

$$\operatorname{div}_{\operatorname{tg}} \left( \mathbf{P} \frac{\partial\sigma}{\partial\mathbf{R}} \right) = \nabla_{\operatorname{tg}}^T a + (aH + bH^2 - 2bK) \mathbf{n}^T + \nabla_{\operatorname{tg}}^T b \mathbf{R} + b \nabla_{\operatorname{tg}}^T H. \quad (37)$$

Due to the fact that  $\mathbf{n}'^T \mathbf{n} = 0$ , we obtain

$$\mathbf{n}'^T \operatorname{div}_{\operatorname{tg}}^T \left( \mathbf{P} \frac{\partial \sigma}{\partial \mathbf{R}} \right) = \mathbf{n}'^T [\nabla_{\operatorname{tg}} a + \mathbf{R} \nabla_{\operatorname{tg}} b + b \nabla_{\operatorname{tg}} H] = \mathbf{n}'^T [\nabla a + \mathbf{R} \nabla b + b \nabla H].$$

Consequently, one obtains the second condition on  $C_t$  in the form

$$\sigma_1 - \sigma_2 + \sigma \cos \theta - \sin \theta \mathbf{n}'^T (\nabla a + b \nabla H + \mathbf{R} \nabla b) = 0. \quad (38)$$

This is *the extended Young–Dupré condition* along contact line  $C_t$  between membrane  $S_t$  and solid surface  $\mathcal{S}$ .<sup>3</sup>

In the case of Helfrich’s energy given by relation (1), we obtain the extended Young–Dupré condition (38) in the form:

$$\sigma_1 - \sigma_2 + \sigma \cos \theta - \kappa \sin \theta \mathbf{n}'^T \nabla H = 0. \quad (39)$$

This last condition was previously obtained in [Gouin 2014b].

## 8. Surfaces of revolution

**8.1. Shape equation for the surfaces of revolution.** Along a revolution surface, the invariants of the curvature tensor depend only on  $s$ , which is the curvilinear abscissa of meridian curve denoted by  $\Gamma$  [Aleksandrov and Zalgaller 1967]:

$$H = H(s), \quad K = K(s).$$

<sup>3</sup>The virtual displacement taken in the most general form (28) does not produce new boundary conditions. Due to the linearity of the virtual work, to prove this property it is sufficient to take  $\xi = \alpha t$ . We obtain

$$\frac{\partial \xi}{\partial \mathbf{x}} = t(\nabla \alpha)^T + \alpha \frac{\partial t}{\partial \mathbf{x}}, \quad \left( \frac{\partial \xi}{\partial \mathbf{x}} \right)^T \mathbf{n}'_1 = \alpha \left( \frac{\partial t}{\partial \mathbf{x}} \right)^T \mathbf{n}'_1.$$

Since

$$\frac{\partial t}{\partial \mathbf{x}} = c N t^T,$$

where  $N$  is the principal unit normal and  $c$  is the curvature along  $C_t$ , one obtains

$$\left( \frac{\partial \xi}{\partial \mathbf{x}} \right)^T \mathbf{n}'_1 = \alpha c t N^T \mathbf{n}'_1$$

and

$$\sin \theta \mathbf{n}'^T \frac{\partial \sigma}{\partial \mathbf{R}} \mathbf{P} \left( \frac{\partial \xi}{\partial \mathbf{x}} \right)^T \mathbf{n}'_1 = \alpha c \sin \theta \mathbf{n}'^T \frac{\partial \sigma}{\partial \mathbf{R}} t N^T \mathbf{n}'_1,$$

which is equal to zero thanks to (34).

Moreover, thanks to (34), we immediately obtain that term

$$\left[ (\sigma_1 - \sigma_2) \mathbf{n}'^T + \sigma \mathbf{n}'^T - \mathbf{n}'^T \operatorname{div}_{\operatorname{tg}}^T \left( \mathbf{P} \frac{\partial \sigma}{\partial \mathbf{R}} \right) \mathbf{n}^T - \mathbf{n}'^T \frac{\partial \sigma}{\partial \mathbf{R}} \mathbf{R} + \cos \theta \mathbf{n}'^T \frac{\partial \sigma}{\partial \mathbf{R}} \mathbf{P} \left( \frac{\partial \mathbf{n}_1}{\partial \mathbf{x}} \right)^T \right] t \alpha$$

is vanishing. Hence, new boundary conditions do not appear on  $C_t$ .

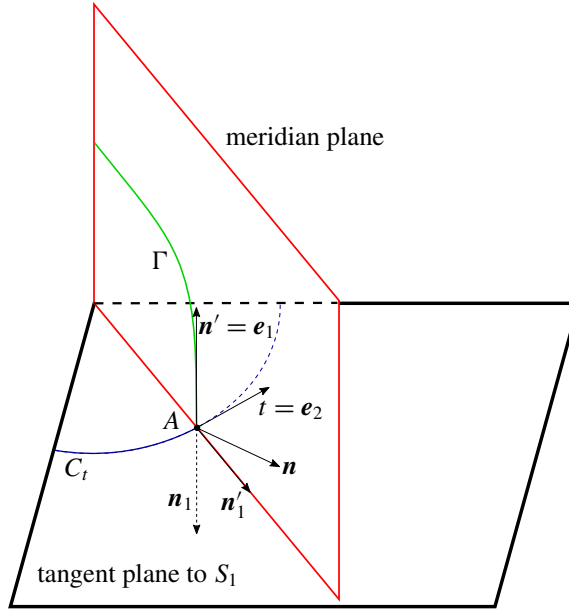


**Figure 3.** The case of a revolution domain. The line  $C_t$  (contact edge between  $S_t$  and  $S_1$ ) is a circle with an axis which is the revolution axis collinear to  $\mathbf{n}_1$ . The meridian curve is denoted  $\Gamma$ ; normal vector  $\mathbf{n}$  and binormal vector  $\mathbf{n}'$  are in the meridian plane of revolution surface  $S_t$ . We have  $\mathbf{n}' = \mathbf{e}_1$  and  $\mathbf{t} = \mathbf{e}_2$ , corresponding to the eigenvectors of the curvature tensor  $\mathbf{R}$  at  $A$ .

One of the eigenvectors, denoted  $\mathbf{e}_1$ , of the curvature tensor  $\mathbf{R}$  is tangent to meridian curve  $\Gamma$  (see Figure 3). Let us remark that for any function  $f(s)$ , one has

$$\nabla_{\text{tg}} f = \frac{df}{ds} \mathbf{e}_1, \quad \Delta_{\text{tg}} f = \frac{d^2 f}{ds^2}.$$

Indeed, the first equation is the definition of the tangential gradient. The second equality is obtained as follows:

$$\begin{aligned} \text{div}_{\text{tg}} \left( \frac{df}{ds} \mathbf{e}_1 \right) &= \text{tr} \left( \mathbf{P} \frac{\partial}{\partial \mathbf{x}} \left( \frac{df}{ds} \mathbf{e}_1 \right) \right) = \text{tr} \left( \mathbf{P} \frac{d}{ds} \left( \frac{df}{ds} \mathbf{e}_1 \right) \otimes \mathbf{e}_1 \right) \\ &= \text{tr} \left( \frac{d^2 f}{ds^2} \mathbf{P} \mathbf{e}_1 \otimes \mathbf{e}_1 + c_1(s) \frac{df}{ds} \mathbf{n} \otimes \mathbf{e}_1 \right) = \frac{d^2 f}{ds^2}. \end{aligned}$$

The Frénet formula was used here:

$$\frac{d\mathbf{e}_1}{ds} = c_1 \mathbf{n}.$$

Also,

$$\operatorname{div}_{\text{tg}}(\mathbf{R}\nabla_{\text{tg}}f) = \operatorname{div}_{\text{tg}}\left(\frac{df}{ds}\mathbf{R}\mathbf{e}_1\right) = \operatorname{div}_{\text{tg}}\left(\frac{df}{ds}c_1\mathbf{e}_1\right) = \frac{d}{ds}\left(c_1\frac{df}{ds}\right).$$

For surfaces of revolution the shape equation (26) becomes

$$\begin{aligned} H\left(\sigma - K\frac{\partial\sigma}{\partial K}\right) + (2K - H^2)\frac{\partial\sigma}{\partial H} - \frac{d^2}{ds^2}\left(\frac{\partial\sigma}{\partial H}\right) - H\frac{d^2}{ds^2}\left(\frac{\partial\sigma}{\partial K}\right) \\ - \frac{dH}{ds}\frac{d}{ds}\left(\frac{\partial\sigma}{\partial K}\right) + \frac{d}{ds}\left(c_1\frac{d}{ds}\left(\frac{\partial\sigma}{\partial K}\right)\right) = \mathcal{P} - p. \end{aligned}$$

**8.2. Extended Young–Dupré condition for surfaces of revolution.** One has along  $C_t$ ,  $\mathbf{t} = \mathbf{e}_2$  and  $\mathbf{n}' = \mathbf{e}_1$ . It implies  $\mathbf{n}'^T \mathbf{R} \mathbf{t} = 0$ . Also, one has

$$\mathbf{n}'^T (\nabla a + b\nabla H + \mathbf{R}\nabla b) = \frac{da}{ds} + b\frac{dH}{ds} + c_1\frac{db}{ds}.$$

The Young–Dupré condition (38) becomes

$$\sigma_1 - \sigma_2 \cos \theta - \sin \theta \left( \frac{da}{ds} + b\frac{dH}{ds} + c_1\frac{db}{ds} \right) = 0.$$

Since

$$a = \frac{\partial\sigma}{\partial H} + H\frac{\partial\sigma}{\partial K}, \quad b = -\frac{\partial\sigma}{\partial K},$$

one finally obtains

$$\sigma_1 - \sigma_2 \cos \theta - \sin \theta \left[ \frac{d}{ds}\left(\frac{\partial\sigma}{\partial H}\right) + c_{n'}\frac{d}{ds}\left(\frac{\partial\sigma}{\partial K}\right) \right] = 0.$$

For the Helfrich energy (1) this expression yields

$$\sigma_1 - \sigma_2 \cos \theta - \kappa \frac{dH}{ds} \sin \theta = 0.$$

## 9. Conclusion

Membranes can be considered as material surfaces endowed with a surface energy density depending on the invariants of the curvature tensor:  $\sigma = \sigma(H, K)$ . By using the principle of virtual working, we derived the boundary conditions on the moving membranes (“shape equation”) as well as two boundary conditions on the contact line. In limit cases, we recover classical boundary conditions. The “shape equation” and the boundary conditions are summarized below in the nondegenerate case (see (26), (36), and (38)) as the following:

- *The equation for the moving surface  $S_t$ :*

$$H \left( \sigma - K \frac{\partial \sigma}{\partial K} \right) + (2K - H^2) \frac{\partial \sigma}{\partial H} - \Delta_{\text{tg}} \frac{\partial \sigma}{\partial H} - H \Delta_{\text{tg}} \frac{\partial \sigma}{\partial K} - \nabla_{\text{tg}}^T H \nabla_{\text{tg}} \frac{\partial \sigma}{\partial K} + \text{div}_{\text{tg}} \left( \mathbf{R} \nabla_{\text{tg}} \frac{\partial \sigma}{\partial K} \right) = \mathcal{P} - p.$$

- *The clamping condition on the moving line  $C_t$ :*

$$\frac{\partial \sigma}{\partial H} + c_t \frac{\partial \sigma}{\partial K} = 0.$$

Also,  $(\mathbf{t}, \mathbf{n}, \mathbf{n}')$  — which is the *Darboux frame* — are the eigenvectors of curvature tensor  $\mathbf{R}$ .

- *Dynamic generalization of the Young–Dupré condition on  $C_t$ :*

$$\sigma_1 - \sigma_2 + \sigma \cos \theta - \sin \theta \mathbf{n}'^T \left( \nabla_{\text{tg}} \left( \frac{\partial \sigma}{\partial H} \right) + (H \mathbf{P} - \mathbf{R}) \nabla_{\text{tg}} \left( \frac{\partial \sigma}{\partial K} \right) \right) = 0.$$

In the case of Helfrich’s energy the generalization of the Young–Dupré condition is reduced to (39):

$$\sigma_1 - \sigma_2 + \sigma \cos \theta - \kappa \sin \theta \mathbf{n}'^T \nabla_{\text{tg}} H = 0.$$

The last term, corresponding to the variation of the mean curvature of  $S_t$  in the binormal direction at the contact line, can dominate the other terms. It could be interpreted as a line tension term usually added in the models with constant surface energy [Babak 2004]. It should also be noted that the droplet volume has no effect in the classical Young–Dupré condition. This is not the case for the generalized Young–Dupré condition since the curvatures can become very large for very small droplets (they are inversely proportional to the droplet size). The clamping condition for the Helfrich energy fixes the value of  $H$  on the contact line:

$$H = H_0 - c_t \frac{\bar{\kappa}}{\kappa}.$$

The new shape equation and boundary conditions can be used for solving dynamic problems. This could be, for example, the study of the “fingering” phenomenon appearing as a result of the nonlinear instability of a moving contact line. This complicated problem will be studied in the future.

## Appendix

Since  $\sigma = \sigma(H, K)$ , we get

$$\nabla_{\text{tg}} \sigma = \frac{\partial \sigma}{\partial H} \nabla_{\text{tg}} H + \frac{\partial \sigma}{\partial K} \nabla_{\text{tg}} K. \quad (40)$$

From (16), we obtain

$$\operatorname{div}_{\operatorname{tg}}\left(\mathbf{P}\frac{\partial\sigma}{\partial\mathbf{R}}\right) = \nabla_{\operatorname{tg}}^T a + (aH + bH^2 - 2bK)\mathbf{n}^T + \nabla_{\operatorname{tg}}^T b\mathbf{R} + b\nabla_{\operatorname{tg}}^T H. \quad (41)$$

Also, one has

$$\operatorname{div}_{\operatorname{tg}}\left(\frac{\partial\sigma}{\partial\mathbf{R}}\mathbf{R}\right) = \operatorname{div}_{\operatorname{tg}}(a\mathbf{R}) + \operatorname{div}_{\operatorname{tg}}(b\mathbf{R}^2).$$

Due to (9), one has

$$\begin{aligned} \operatorname{div}_{\operatorname{tg}}(a\mathbf{R}) &= (\nabla_{\operatorname{tg}}^T a)\mathbf{R} + a\nabla_{\operatorname{tg}}^T H + a(H^2 - 2K)\mathbf{n}^T, \\ \operatorname{div}_{\operatorname{tg}}(b\mathbf{R}^2) &= \operatorname{div}_{\operatorname{tg}}[b(H\mathbf{R} - K\mathbf{P})] \\ &= \nabla_{\operatorname{tg}}^T(bH)\mathbf{R} + bH[\nabla_{\operatorname{tg}}^T H + (H^2 - 2K)\mathbf{n}^T] - \nabla_{\operatorname{tg}}^T(bK) - bKH\mathbf{n}^T. \end{aligned}$$

Consequently,

$$\begin{aligned} \operatorname{div}_{\operatorname{tg}}\left(\frac{\partial\sigma}{\partial\mathbf{R}}\mathbf{R}\right) &= (\nabla_{\operatorname{tg}}^T(a + bH))\mathbf{R} \\ &\quad + (a + bH)\nabla_{\operatorname{tg}}^T H - \nabla_{\operatorname{tg}}^T(bK) + (aH^2 + bH^3 - 2aK - 3bHK)\mathbf{n}^T. \end{aligned} \quad (42)$$

From relations (40), (41), and (42), we deduce

$$\nabla_{\operatorname{tg}}\sigma - \operatorname{div}_{\operatorname{tg}}^T\left(\frac{\partial\sigma}{\partial\mathbf{R}}\mathbf{R}\right) + \mathbf{R}\operatorname{div}_{\operatorname{tg}}^T\left(\mathbf{P}\frac{\partial\sigma}{\partial\mathbf{R}}\right) = (2aK + 3bHK - aH^2 - bH^3)\mathbf{n}.$$

Using (41), one obtains

$$\mathbf{P}\operatorname{div}_{\operatorname{tg}}^T\left(\mathbf{P}\frac{\partial\sigma}{\partial\mathbf{R}}\right) = \nabla_{\operatorname{tg}} a + \mathbf{R}\nabla_{\operatorname{tg}} b + b\nabla_{\operatorname{tg}} H.$$

One deduces

$$\operatorname{div}_{\operatorname{tg}}\left[\mathbf{P}\operatorname{div}_{\operatorname{tg}}^T\left(\mathbf{P}\frac{\partial\sigma}{\partial\mathbf{R}}\right)\right] = \Delta_{\operatorname{tg}} a + \operatorname{div}_{\operatorname{tg}}(\mathbf{R}\nabla_{\operatorname{tg}} b) + b\Delta_{\operatorname{tg}} H + \nabla_{\operatorname{tg}}^T b\nabla_{\operatorname{tg}} H. \quad (43)$$

From relations (40), (41), and (42), we deduce

$$\begin{aligned} \nabla_{\operatorname{tg}}\sigma - \operatorname{div}_{\operatorname{tg}}^T\left(\frac{\partial\sigma}{\partial\mathbf{R}}\mathbf{R}\right) + \mathbf{R}\operatorname{div}_{\operatorname{tg}}^T\left(\mathbf{P}\frac{\partial\sigma}{\partial\mathbf{R}}\right) &= (2aK + 3bHK - aH^2 - bH^3)\mathbf{n} + \frac{\partial\sigma}{\partial H}\nabla_{\operatorname{tg}} H + \frac{\partial\sigma}{\partial K}\nabla_{\operatorname{tg}} K \\ &\quad - \mathbf{R}\nabla_{\operatorname{tg}}(a + bH) - (a + bH)\nabla_{\operatorname{tg}} H + \nabla_{\operatorname{tg}}(bK) + \mathbf{R}\nabla_{\operatorname{tg}} a \\ &\quad + (aH + bH^2 - 2bK)\mathbf{R}\mathbf{n} + \mathbf{R}^2\nabla_{\operatorname{tg}} b + b\mathbf{R}\nabla_{\operatorname{tg}} H + \mathbf{T} \\ &= \mathbf{0}. \end{aligned}$$

Using relations  $\mathbf{Rn} = \mathbf{0}$ , Lemma 1 (identity 3) and expressions of  $a$  and  $b$  given by (16), we obtain

$$\begin{aligned} \frac{\partial \sigma}{\partial H} \nabla_{\text{tg}} H + \frac{\partial \sigma}{\partial K} \nabla_{\text{tg}} K - \mathbf{R} \nabla_{\text{tg}}(a + bH) - (a + bH) \nabla_{\text{tg}} H + \nabla_{\text{tg}}(bK) \\ + \mathbf{R} \nabla_{\text{tg}} a + (aH + bH^2 - 2bK) \mathbf{Rn} + \mathbf{R}^2 \nabla_{\text{tg}} b + b \mathbf{R} \nabla_{\text{tg}} H = \mathbf{0}. \end{aligned}$$

Consequently,

$$\nabla_{\text{tg}} \sigma - \text{div}_{\text{tg}}^T \left( \frac{\partial \sigma}{\partial \mathbf{R}} \mathbf{R} \right) + \mathbf{R} \text{div}_{\text{tg}}^T \left( \mathbf{P} \frac{\partial \sigma}{\partial \mathbf{R}} \right) = (2aK + 3bHK - aH^2 - bH^3) \mathbf{n}.$$

Finally, using (43), one obtains

$$\begin{aligned} [p + H\sigma - \Delta_{\text{tg}} a - b \Delta_{\text{tg}} H - \nabla_{\text{tg}}^T b \nabla_{\text{tg}} H - \text{div}_{\text{tg}}(\mathbf{R} \nabla_{\text{tg}} b) \\ + (2aK + 3bHK - aH^2 - bH^3)] \mathbf{n} + \mathbf{T} = \mathbf{0}, \quad (44) \end{aligned}$$

where all tangential terms disappear in the boundary condition on  $S_t$ .

### Acknowledgments

The authors thank the anonymous referees for their noteworthy and helpful remarks that greatly contributed to improve the final version of the paper.

### References

- [Alberts et al. 2002] B. Alberts, A. Johnson, J. Lewis, M. Raff, K. Roberts, and P. Walter, *Molecular biology of the cell*, 4th ed., Garland Science, New York, 2002.
- [Aleksandrov and Zalgaller 1967] A. D. Aleksandrov and V. A. Zalgaller, *Intrinsic geometry of surfaces*, Translations of Mathematical Monographs **15**, American Mathematical Society, Providence, R.I., 1967.
- [Babak 2004] V. G. Babak, “Stability of the lenslike liquid thickening (the drop) on a solid substrate”, *J. Adhesion* **80**:8 (2004), 685–703.
- [Berdichevsky 2009] V. L. Berdichevsky, *Variational principles of continuum mechanics, I: Fundamentals*, Springer, 2009.
- [Biscari et al. 2004] P. Biscari, S. M. Canevese, and G. Napoli, “Impermeability effects in three-dimensional vesicles”, *J. Phys. A* **37**:27 (2004), 6859–6874.
- [Capovilla and Guven 2002] R. Capovilla and J. Guven, “Stresses in lipid membranes”, *J. Phys. A* **35**:30 (2002), 6233–6247.
- [Fournier 2007] J.-B. Fournier, “On the stress and torque tensors in fluid membranes”, *Soft Matter* **3** (2007), 883–888.
- [Gavrilyuk 2011] S. Gavrilyuk, “Multiphase flow modeling via Hamilton’s principle”, pp. 163–210 in *Variational models and methods in solid and fluid mechanics*, edited by F. dell’Isola and S. Gavrilyuk, CISM Courses and Lect. **535**, Springer, 2011.
- [Gavrilyuk and Gouin 1999] S. Gavrilyuk and H. Gouin, “A new form of governing equations of fluids arising from Hamilton’s principle”, *Internat. J. Engrg. Sci.* **37**:12 (1999), 1495–1520.

- [Germain 1973] P. Germain, “The method of virtual power in continuum mechanics, 2: Microstructure”, *SIAM J. Appl. Math.* **25**:3 (1973), 556–575.
- [Gouin 2007] H. Gouin, “The d’Alembert–Lagrange principle for gradient theories and boundary conditions”, pp. 79–95 in *Asymptotic methods in nonlinear wave phenomena*, edited by T. Ruggeri and M. Sammartino, World Scientific, 2007.
- [Gouin 2014a] H. Gouin, “Interfaces endowed with nonconstant surface energies revisited with the d’Alembert–Lagrange principle”, *Math. Mech. Complex Syst.* **2**:1 (2014), 23–43.
- [Gouin 2014b] H. Gouin, “Vesicle model with bending energy revisited”, *Acta Appl. Math.* **132** (2014), 347–358.
- [Helfrich 1973] W. Helfrich, “Elastic properties of lipid bilayers: theory and possible experiments”, *Z. Naturforsch. C.* **28**:11–12 (1973), 693–703.
- [Lipowsky and Sackmann 1995] R. Lipowsky and E. Sackmann (editors), *Structure and dynamics of membranes: from cells to vesicles*, Handbook of Biological Physics **1**, Elsevier, Amsterdam, 1995.
- [Napoli and Vergori 2010] G. Napoli and L. Vergori, “Equilibrium of nematic vesicles”, *J. Phys. A* **43**:44 (2010), 445207.
- [Rocard 1952] Y. Rocard, *Thermodynamique*, Masson, Paris, 1952.
- [Rosso and Virga 1999] R. Rosso and E. G. Virga, “Adhesive borders of lipid membranes”, *Proc. Roy. Soc. Lond. A* **455**:1992 (1999), 4145–4168.
- [Schwartz 1966] L. Schwartz, *Théorie des distributions*, Publications de l’Institut de Mathématique de l’Université de Strasbourg **9–10**, Hermann, 1966.
- [Seifert 1997] U. Seifert, “Configurations of fluid membranes and vesicles”, *Adv. Phys.* **46**:1 (1997), 13–137.
- [Serrin 1959] J. Serrin, “Mathematical principles of classical fluid mechanics”, pp. 125–263 in *Handbuch der Physik*, vol. 8/1: Strömungsmechanik I, edited by S. Flügge, Springer, 1959.
- [Steigmann and Li 1995] D. J. Steigmann and D. Li, “Energy-minimizing states of capillary systems with bulk, surface, and line phases”, *IMA J. Appl. Math.* **55**:1 (1995), 1–17.
- [Tu 2011] Z. Tu, “Geometry of membranes”, *J. Geom. Symmetry Phys.* **24** (2011), 45–75.
- [Willmore 1993] T. J. Willmore, *Riemannian geometry*, Clarendon, New York, 1993.
- [Zhong-can and Helfrich 1989] O.-Y. Zhong-can and W. Helfrich, “Bending energy of vesicle membranes: general expressions for the first, second, and third variation of the shape energy and applications to spheres and cylinders”, *Phys. Rev. A* **39**:10 (1989), 5280–5288.

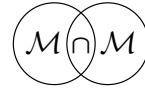
Received 12 Oct 2018. Revised 20 Feb 2019. Accepted 2 Apr 2019.

SERGEY GAVRILYUK: [sergey.gavrilyuk@univ-amu.fr](mailto:sergey.gavrilyuk@univ-amu.fr)  
Aix Marseille Univ, CNRS, IUSTI, UMR 7343, Marseille, France

HENRI GOUIN: [henri.gouin@univ-amu.fr](mailto:henri.gouin@univ-amu.fr), [henri.gouin@yahoo.fr](mailto:henri.gouin@yahoo.fr)  
Aix Marseille Univ, CNRS, IUSTI, UMR 7343, Marseille, France







# ENERGY-BASED TRAJECTORY TRACKING AND VIBRATION CONTROL FOR MULTILINK HIGHLY FLEXIBLE MANIPULATORS

IVAN GIORGIO AND DIONISIO DEL VESCOVO

*“I accept nothing on authority. A hypothesis must be backed by reason, or else it is worthless.”*  
— Isaac Asimov, “Reason”, *I, Robot* (1950)

In this paper, a discrete model is adopted, as proposed by Hencky for elastica based on rigid bars and lumped rotational springs, to design the control of a lightweight planar manipulator with multiple highly flexible links. This model is particularly suited to deal with nonlinear equations of motion as those associated with multilink robot arms, because it does not include any simplification due to linearization, as in the assumed modes method. The aim of the control is to track a trajectory of the end effector of the robot arm, without the onset of vibrations. To this end, an energy-based method is proposed. Numerical simulations show the effectiveness of the presented approach.

## 1. Introduction

Discrete formulations for continuous systems, usually, are required to avoid the difficulty associated with solving partial differential equations and with satisfying their boundary conditions. In order to eliminate the spatial dependence from the problem and, thus, to deal with a set of ordinary differential equations which approximates the distributed-parameter system, a proper discretization can be made. The adopted techniques for this purpose can be grouped into two main categories: procedures based on the approximation of the solution by means of a finite series of given functions and approaches resulting in lumped parameter systems. In particular, to model multilink flexible arms, many authors employed the assumed modes method [Bellezza et al. 1990; Khorrami et al. 1991; De Luca and Siciliano 1991] and the finite element formulation [Ramachandran et al. 1992; Sharf 1996], both of which belong to the first group; other authors prefer the lumped-parameter approach [Rubinstein 1999; Dupac and Noroozi 2014; Giorgio and Del Vescovo 2018] for ease of use.

---

**Communicated by Francesco dell’Isola.**

*MSC2010:* primary 70E60; secondary 70E55, 70KXX, 74KXX, 74SXX.

*Keywords:* nonlinear elastica, discrete modeling, flexible robot arms, energy-based control.

In the assumed modes method, the solution representing the transverse deflection of the flexible beams is expanded into a finite summation of space-dependent functions satisfying the geometric boundary conditions (i.e., admissible functions) with time-dependent coefficients, i.e., the generalized coordinates. In this method, the set of admissible functions is much larger than the set of eigenfunctions (i.e., normal modes); thus, the solution is affected by an error related to the choice of the admissible functions. This error increases with the eigenfrequencies, and to reduce it, a relatively large number of the terms of the truncated series is advisable to be employed. Although this method has been widely used in the literature, it is only applicable to discretize linear systems. Nevertheless, the equations related to a multilink manipulator are strongly nonlinear. To overcome this issue, a simplified assumption should be made considering that the motion could be characterized by two distinct time scales: one “slower” for the overall motion and one “faster” for the superimposed vibration. Therefore, the key idea is to linearize the nonlinear equations around any configuration reached during the motion, or in other words it is possible to assume that, in a reasonably small time interval, the overall motion is sufficiently slow and the current configuration is almost time-constant when compared to the vibration. In view of these considerations, the problem of the time dependence of the frequency equation for planar multilink flexible arms [De Luca and Siciliano 1991] could be solved by keeping constant the boundary conditions due to mass terms for a fixed arm configuration. But in this way, many admissible functions for the transverse displacement discretization are required, which increases the number of discrete Lagrange equations obtained. An alternative way, to keep the number of final ordinary equations lower, consists of updating the values of the mass and inertia coefficients which appear in the boundary conditions at each time step, thinking of them, in view of the two time scales, as constant parameters and, hence, having a suitable approximation for the admissible functions (see, e.g., [Giorgio et al. 2019]).

The finite element formulation has the same basic idea as the assumed modes method; the main difference between the two approaches lies in the nature of the admissible functions. In the assumed modes method, the trial functions are defined on the entire domain; in the finite element method, they are functions defined on compact subdomains of the system, namely, the “finite elements”. This particular subdivision of the entire domain allows one to use simpler admissible functions, typically low-degree polynomials (i.e., interpolating functions). Unfortunately, the greater flexibility of this method entails more degrees of freedom and, ultimately, a greater number of discrete equations than those required by the assumed modes method. Besides, analogously to the previous method, the natural frequencies computed with the finite element analysis are overestimated. However, from a computational point of view, this method requires fewer mathematical operations;

therefore, it is particularly suited for dynamic model-based online controller implementations [Theodore and Ghosal 1995]. Although the finite element method can be identified as a different version of the assumed modes method, it can be generalized to be used in a wider context, in particular, when nonlinear effects arise as for a multilink manipulator [Sharf 1996; Eugster et al. 2014; Luongo and D'Annibale 2013]. To address some issues related to failures in convergence that are occasionally experienced, some authors have proposed a mixed formulation, based on both stress and displacement degrees of freedom, which appears very promising in this respect [Hodges 1990; Garcea et al. 1998]. However, this reformulation of the problem involves a greater complexity of modeling. An alternative approach is based on the isogeometric formulation proposed by [Hughes et al. 2005] and further developed by many other research groups (see, e.g., [Greco and Cuomo 2013; Balobanov et al. 2016; Cazzani et al. 2016; Weeger et al. 2013] and more recently [Greco et al. 2017; Yildizdag et al. 2018]). The key concept of the isogeometric analysis consists of using B-splines or NURBS curves both for representing the geometry of the system and as interpolating functions in the finite element method. Some examples in which such a method has been adopted within the framework of nonlinear structural vibration analysis produced very promising results. In addition, this formulation allows one to use fewer elements than the classical polynomial-based finite element analysis without losing accuracy.

Lumped parameter models, applied to a beam-like structure, simplify the description of the behavior of one-dimensional continuum systems into an articulated chain consisting of a discrete number of rigid bodies that approximate the behavior of the distributed system under the assumption that all interactions between the rigid segments take place via frictionless hinges with elastic rotational spring and possibly dampers [Wang et al. 2015; Kocsis et al. 2017; Turco et al. 2016]. Therefore, the lumped-parameter approach is the only method born naturally nonlinear. The first author, to our knowledge, to propose the replacement of the continuum structure with a discrete one was Hencky in 1920, who studied the buckling of a beam. To solve dynamical problems, also the distributions of the mass should be discretized, sometimes by taking into account the inertial properties of the rigid segments [Rubinstein 1999] and other times by considering lumped masses in the fictitious joints [Feliu et al. 1992]. In order to improve performances of trajectory tracking for the end effector of a multilink manipulator, in this paper, for its simplicity and nonlinear character, the latter method is adopted. Indeed, improving performances means decreasing the overall time of the motion for the task; this makes the hypothesis of linearization characterizing the assumed modes method no longer satisfied in many applications. In any case, all the methods described have advantages and disadvantages. Therefore, the wise judgment of the researcher should be the guide in a case-by-case choice, depending on the particular application.

The aim of the work concerns the modeling and control of flexible planar multilink arms. Many researchers have been recently paying attention to this kind of system because of its increasing importance within the applications of so-called soft robots. In addition, it is conceivable to use the present formulation to model polymeric chains as well as some highly flexible structures in the space applications. Thus, the considered model may find applications from nano- until macroscales. The key point of the paper is using flexible hinges and their description using finite rotations within the discrete modeling of the multilink arm. In particular, an energy-based method is proposed to control the trajectory of the robot arm end effector, without the onset of vibrations. The paper is organized as follows. First, Section 2 gives the kinematic description for the introduced discrete method applied to planar multilink flexible arms in a recursive form and, accordingly to a Lagrangian approach, the equations of motion. Section 3 is devoted to describing the proposed control strategy using a trajectory planning described in Section 3.1. Section 4 reports simulation results for a two-link flexible arm. Conclusions are presented in the final section.

## 2. Modeling

A planar articulated kinematic chain of  $n_\ell$  flexible links of length  $\ell_i$  — connected by revolute joints — is considered. The  $i$ -th flexible link is studied as a lumped parameter system consisting of  $n_e$  successive rigid rods of length  $\eta_j$  (with  $j = 1, \dots, n_e$ ) and connected by torsional springs. For the sake of simplicity, it is assumed that the rods are arranged along a straight line in the undeformed configuration. Lumped masses are placed at the boundaries of each rigid segment. As a result, each link is a system of  $n_e$  massless rigid rods and  $n_e + 1$  point masses. The flexural stiffness of links is given by torsional springs. Finally, actuators and payload are modeled as rigid bodies. The center of mass of each actuator is located at the joint point of the link, while the payload barycenter is located at the tip of the whole system.

In order to describe motions of the multilink arm,  $n_\ell$  moving reference frames are introduced, i.e., one for each flexible link in the spirit of the Denavit–Hartenberg convention. The  $x$ -axis (abscissa) of the  $i$ -th link is oriented as its first rigid segment and its origin, whose position vector expressed in the global frame is denoted by  $\mathbf{r}_i$ , coincides with the position of the actuated joint. Therefore, such moving reference frames can be referred to as “pseudoclamped” frames (see Figure 1).

The following two Lagrangian coordinates are introduced for the multilink arm. First is the joint angle,  $\vartheta_i(t)$ , i.e., the relative rotation between the first segment of the  $i$ -th link and the last segment of the preceding link, which meet in the  $i$ -th joint. The angle  $\vartheta_1(t)$  is evaluated with respect to the  $X_0$ -axis of the global reference

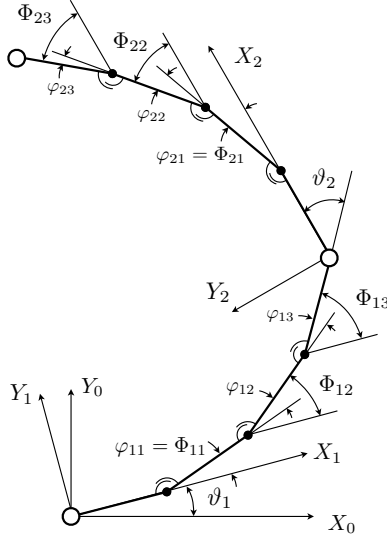


**Figure 1.** Discrete system corresponding to a planar two-link flexible arm.

frame. Second is  $\Phi_{ij}(t)$ , with  $i = 1, \dots, n_\ell$  and  $j = 1, \dots, n_e$ , the relative angle of the  $j$ -th segment with respect to the  $x$ -axis of  $i$ -th reference frame.

The relative angles between adjacent segments are defined as  $\varphi_{ij}(t) = \Phi_{ij}(t) - \Phi_{i,j-1}(t)$ , with  $\varphi_{i1}(t) = \Phi_{i1}(t)$ . Within the local reference frame related to link  $i$ , the position vector of any end point of rigid segments is denoted as  ${}^i\mathbf{p}_{ij}(t)$ . Therefore, within the same  $i$ -th frame, the relation  ${}^i\mathbf{r}_{i+1}(t) = {}^i\mathbf{p}_{in_e}(t)$  is valid owing to the hinge constraint requiring the origin of the  $(i+1)$ -th frame and the end point of the  $i$ -th link to have the same position in space. By introducing the rotation matrices

$$R_i = \begin{bmatrix} \cos \vartheta_i & -\sin \vartheta_i \\ \sin \vartheta_i & \cos \vartheta_i \end{bmatrix}, \quad \widehat{R}_{ij} = \begin{bmatrix} \cos \Phi_{ij} & -\sin \Phi_{ij} \\ \sin \Phi_{ij} & \cos \Phi_{ij} \end{bmatrix} \quad (1)$$

the position of the generic point of the kinematic chain can be written in the local reference frame using the recursive formula

$${}^i\mathbf{p}_{ij} = {}^i\mathbf{p}_{i,j-1} + \widehat{R}_{i,j-1}(\Phi_{i,j-1}){}^i\mathbf{p}_{i1}, \quad {}^i\mathbf{p}_{i1} \equiv [\eta_i, 0]^T, \quad (2)$$

and in the global reference frame as

$$\mathbf{p}_{ij} = \mathbf{r}_i + Q_i^i \mathbf{p}_{ij} \quad (3)$$

where the global transformation operator  $Q_i$  (with  $i = \{1, \dots, n_\ell\}$ ) is obtained by the recursive equation

$$Q_i = \widehat{Q}_{i-1} R_i(\vartheta_i), \quad \begin{cases} \widehat{Q}_0 = I, \\ \widehat{Q}_i = Q_i \widehat{R}_{i n_e}(\Phi_{i n_e}), \end{cases} \quad (4)$$

$I$  being the identity operator. Similarly, the following expression is fulfilled by the origins of the local reference frames:

$$\mathbf{r}_{i+1} = \mathbf{r}_i + Q_i^i \mathbf{r}_{i+1}. \quad (5)$$

The angular velocity of the  $i$ -th reference frame reads as

$$\dot{\alpha}_i(t) = \sum_{j=1}^i \dot{\vartheta}_j(t) + \sum_{k=1}^{i-1} \dot{\Phi}_{k n_e}(t) \quad (6)$$

while the angular velocity of the payload can be evaluated as  $\dot{\alpha}_p(t) = \dot{\alpha}_{n_\ell}(t) + \dot{\Phi}_{n_\ell n_e}$  and, finally, the velocity vector of any point of the kinematic chain is easy to compute as

$$\dot{\mathbf{p}}_i = \dot{\mathbf{r}}_i + \dot{Q}_i^i \mathbf{p}_i + Q_i^i \dot{\mathbf{p}}_i. \quad (7)$$

The total kinetic energy of the mechanical system stemming from the above assumptions is

$$\mathfrak{K} = \sum_{i=1}^{n_\ell} (\mathfrak{K}_{hi} + \mathfrak{K}_{li}) + \mathfrak{K}_p \quad (8)$$

where the following terms can be recognized:

- (1) the kinetic energy of the actuator located at the  $i$ -th joint and characterized by mass  $m_{hi}$  and moment of inertia  $J_{hi}$ ,

$$\mathfrak{K}_{hi} = \frac{1}{2} m_{hi} \dot{\mathbf{r}}_i^T \dot{\mathbf{r}}_i + \frac{1}{2} J_{hi} \dot{\alpha}_i^2,$$

- (2) the kinetic energy of each link with lumped mass  $m_{ij}$ ,

$$\mathfrak{K}_{li} = \frac{1}{2} \sum_{j=1}^{n_e} m_{ij} \dot{\mathbf{p}}_{ij}^T \dot{\mathbf{p}}_{ij},$$

- (3) and the kinetic energy of the payload with mass  $m_p$  and moment of inertia  $J_p$ ,

$$\mathfrak{K}_p = \frac{1}{2} m_p \dot{\mathbf{p}}_{n_\ell n_e}^T \dot{\mathbf{p}}_{n_\ell n_e} + \frac{1}{2} J_p \dot{\alpha}_p^2.$$

The elastic potential energy is assumed to be

$$\mathfrak{U} = \sum_{i=1}^{n_\ell} \sum_{j=1}^{n_e} b_i [1 - \cos \varphi_{ij}] \quad (9)$$

where  $b_i = Y_i j_i / \eta_i$  is the lumped bending stiffness of the introduced torsional springs,  $Y_i$  is the Young modulus of constituting material, and  $j_i$  is the second moment of area of the link's cross-section. We remark that this model is able to take into account also nonlinear elastic behaviors of the system; indeed, it has been shown [dell'Isola et al. 2016] that such a model, in the homogenized limit, converges to that of a nonlinear beam [Turco 2018; Pietraszkiewicz and Eremeyev 2009; Spagnuolo and Andreaus 2019] being shear undeformable, suitable for the description of problems involving large displacements and large deformations (see [Rosi et al. 2018; Placidi et al. 2017; Baroudi et al. 2019] for more details on methods for obtaining material parameters), and whose deformation energy density depends only upon the exact curvature. Note that the linearized form of (9) is simply a quadratic form in the relative angle  $\varphi_{ij}$ . Here, the general expression (9) of the strain energy is considered, because we are dealing with situations in which the kinetic energy contains nonnegligible nonquadratic terms. It would not be coherent to consider a quadratic approximation only for the elastic energy (while not for the kinetic energy) and, in any case, it would not lead to any significant simplification. Besides, the linearization of corresponding equation is a mathematical trick which aims to obtain solutions more easily, but it is not always possible.

It is worth noting that the choice of  $\Phi_{ij}$  variables implies a simpler expression for the kinetic energy, while the choice of  $\varphi_{ij}$  variables implies a simpler expression for the elastic energy; therefore, since the kinetic energy represents the more complex term in the Lagrangian, the first set of variables is used.

The equations of motion obeyed by the considered planar  $n_\ell$ -link flexible arm can be derived by introducing the Lagrangian:

$$\mathcal{L} = \mathcal{K} - \mathcal{U}. \quad (10)$$

Possibly, some viscous dissipation can also be introduced by means of a Rayleigh potential as

$$\mathcal{D} = \sum_{i=1}^{n_\ell} \sum_{j=1}^{n_e} \frac{1}{2} c_i \dot{\varphi}_{ij}^2. \quad (11)$$

By differentiating  $\mathcal{D}$  with respect to the velocities  $\dot{\varphi}_{ij}$  and multiplying the result by the virtual angular displacements  $\delta\varphi_{ij}$ , the work done by dissipative moments  $\sum_{i=1}^{n_\ell} \sum_{j=1}^{n_e} c_i \dot{\varphi}_{ij} \delta\varphi_{ij}$  can be evaluated. This work becomes

$$\sum_{i=1}^{n_\ell} \sum_{j=1}^{n_e} c_i (\dot{\Phi}_{ij} - \dot{\Phi}_{i,j-1}) \delta(\Phi_{ij} - \Phi_{i,j-1})$$

when it is expressed in terms of the chosen Lagrangian coordinates and, hence, the dissipative terms to be added to the equations of motion are easily obtained.

In order to model friction which may occur within the joints, a Lund–Grenoble model is employed. The reason for such a choice lies in the fact that it is able to take into account the predominant nonlinear effects involved in such phenomena like presliding displacement, stick-slip motion, the Stribeck effect, and so forth [Canudas de Wit et al. 1995]. Since this formulation is based on a *dynamic model*, the friction torque evolves according to a differential equation conceived to match experimental measures. A simple evolution rule for the friction torques  $\tau_{ji}$  can be assumed as

$$\frac{d\tau_{ji}}{dt} = k_i \dot{\vartheta}_i \left( 1 - \frac{\tau_{ji}}{\tau_L(\dot{\vartheta}_i)} \text{sign } \dot{\vartheta}_i \right) \quad (12)$$

where  $\tau_L(\dot{\vartheta}_i) = \tau_C + (\tau_S - \tau_C) \exp[-(\dot{\vartheta}_i/v_s)^2]$  is the limit torque related to the Stribeck effect. The quantity  $\tau_S$  is the static friction torque,  $\tau_C$  is the Coulomb friction torque, and  $v_s$  represents the Stribeck velocity.

### 3. Control strategy

In this section, an energy-based control approach is proposed to solve a trajectory-tracking and vibration control problem. In particular, given a family of desired trajectories for the tip of each link,  $\mathbf{x}_{des i}(t)$ , we propose to implement a strategy of control based on the potential energy

$$U(\vartheta_i, \varphi_{ij}) = \sum_{i=1}^{n_\ell} \frac{1}{2} K_{c i} \|\mathbf{p}_{i n_e}(\vartheta_i, \varphi_{ij}) - \mathbf{x}_{des i}(t)\|^2 \quad (13)$$

where  $K_{c i}$  are positive constant control parameters. The virtual work related to that “control action” can be easily expressed as

$$\delta U = \sum_{i=1}^{n_\ell} \frac{\partial U}{\partial \vartheta_i} \delta \vartheta_i + \sum_{i=1}^{n_\ell} \sum_{j=1}^{n_e} \frac{\partial U}{\partial \varphi_{ij}} \delta \varphi_{ij} \quad (14)$$

where the negative gradient of the potential  $U$ , whose components are  $-\partial U/\partial \vartheta_i$  and  $-\partial U/\partial \varphi_{ij}$ , is the generalized conservative action which does work on the Lagrangian coordinates  $\vartheta_i$  and  $\varphi_{ij}$ . Indeed, these actions can be interpreted as joint torques and lumped moments which bend the link in correspondence of the connections between adjacent rigid segments. Therefore, measuring the variables  $\vartheta_i$  and  $\varphi_{ij}$ , it is possible to compute these generalized actions and to feed them back to the multilink in order to mimic the above mentioned potential  $U$ . Regarding the design phase of the control, both the measurements of variables  $\varphi_{ij}$  and the feeding of applied moments  $\partial U/\partial \varphi_{ij}$  can be implemented by means of piezoelectric patches located on the ends of the segments in which the system has been discretized. We briefly recall, indeed, that piezoelectric transducers are simultaneously able to be employed as both sensors and actuators [Alessandroni et al.

2005; Lumentut and Howard 2015; Chróścielewski et al. 2019; Lossouarn et al. 2015] and they can nowadays exert forces up to 70 kN [Aminzahed et al. 2017]. Thus, they are particularly suited for this kind of control, which results in being colocated in the sense of [Cannon 1984]. In addition, the present technique can be classified in the framework of a virtual passive approach. As it is characterized by a passive constitutive law, it exhibits with respect to a purely active approach the main advantage of being unconditionally stable [Juang and Phan 1992].

To improve the performance of the control, we can also introduce a dissipative control action by means of the Rayleigh function

$$D(\vartheta_i, \varphi_{ij}, \dot{\vartheta}_i, \dot{\varphi}_{ij}) = \sum_{i=1}^{n_\ell} \frac{1}{2} C_{ci} \|\dot{\mathbf{p}}_{i n_e} - \dot{\mathbf{x}}_{des i}(t)\|^2 \quad (15)$$

expressed in terms of the relative velocities between the moving ends of each link and the desired points of the trajectory. The quantities  $C_{ci}$  are positive constant control parameters related to the introduced damping. Analogously to what has been done above, the virtual work done by the dissipative control action is

$$\delta D = \sum_{i=1}^{n_\ell} \frac{\partial D}{\partial \dot{\vartheta}_i} \delta \vartheta_i + \sum_{i=1}^{n_\ell} \sum_{j=1}^{n_e} \frac{\partial D}{\partial \dot{\varphi}_{ij}} \delta \varphi_{ij}, \quad (16)$$

the quantities  $-\partial D/\partial \dot{\vartheta}_i$  and  $-\partial D/\partial \dot{\varphi}_{ij}$  being the new generalized actions to be added to the previous ones. In order to implement this additional contribution, however, it is necessary to employ further velocity sensors for  $\dot{\vartheta}_i$  and  $\dot{\varphi}_{ij}$ .

**3.1. Trajectory planning.** In this section, in order to analyze the capabilities of the proposed control law, a two-link arm is considered and two geometric paths to be followed by the end effector  $\mathbf{x}_{des n_\ell} = \mathbf{x}_{des n_\ell}(u)$  are introduced, defined by means of a parametrization in terms of the scalar  $u$ : a rectilinear and a closed loop path. Each geometric path is tracked according to the motion law  $u = u(t)$ . In particular, a polynomial function, whose coefficients have been determined in order to satisfy proper boundary conditions, i.e., null values up to the time derivative of the jerk, is employed as

$$u_{des}(t) = u_0 + A_{des} [126(t/T_s)^5 - 420(t/T_s)^6 + 540(t/T_s)^7 - 315(t/T_s)^8 + 70(t/T_s)^9] \quad (17)$$

where  $u_0$  is the value at the initial instant,  $A_{des}$  is the amplitude, and  $T_s$  is the time of the task.

Once the trajectory is assigned to the end effector, the trajectories for the intermediate joint points are obtained by assuming a rigid motion for the corresponding links.

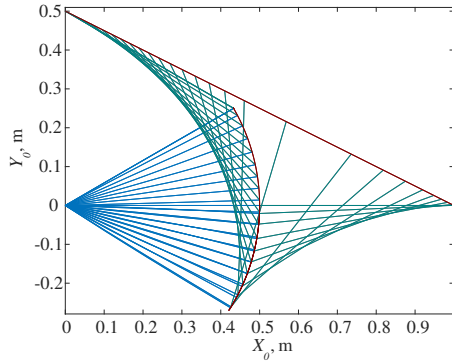


**Figure 2.** Straight trajectory.

*Rectilinear trajectory.* The considered rectilinear trajectory is defined as

$$\begin{cases} x_{\text{des}2} = \ell_1 + \ell_2 - u_{\text{des}} \cos \alpha, \\ y_{\text{des}2} = u_{\text{des}} \sin \alpha \end{cases} \quad (18)$$

where  $u_0 = 0$  and  $A_{\text{des}} = \sqrt{\ell_1^2 + (\ell_1 + \ell_2)^2}$ . The parameter  $u_{\text{des}}$  ranges from 0 to  $A_{\text{des}}$  (achieved at time  $T_s$ ); this means that initially the manipulator is arranged along the axis  $X_0$ , and finally the end effector reaches the  $Y_0$  axis at the point  $(0, \ell_1)$ . Hence,  $\alpha = \text{atan}[\ell_1/(\ell_1 + \ell_2)]$ .

*Closed loop trajectory.* The closed loop trajectory is defined as

$$\begin{cases} x_{\text{des}2} = \frac{1}{8} \left[ \cos u_{\text{des}} + \sqrt{3 + 2 \sin u_{\text{des}} - \sin(u_{\text{des}})^2} \right], \\ y_{\text{des}2} = \frac{1}{4} (1 + \sin u_{\text{des}}) + \ell_1/5 \end{cases} \quad (19)$$

where  $u_0 = 3/2\pi$  and  $A_{\text{des}} = 2\pi$ . The parameter  $u_{\text{des}}$  ranges from  $u_0$  to  $u_0 + A_{\text{des}}$ . These values are chosen so as to have the end effector initially on the  $Y_0$  axis — at the point  $(0, \ell_1/5)$  — and returning to the same position at the end of the motion.

#### 4. Numerical simulations

In performing numerical simulations we have considered the links in the two-link planar manipulator having length  $\ell_1 = \ell_2 = 0.5$  m and having a rectangular cross-section of size  $2 \times 50$  mm; the discretization of each link is made by dividing it into four segments. The Young modulus of the material constituting the link is  $Y_b = 200$  GPa, and thus, the bending stiffnesses are  $b_1 = b_2 = 53.3$  N m; the lumped masses are assumed to be  $m_{ij} = 0.0981$  kg for the inner points and half of this value for the outermost points; the payload mass and moment of inertia are  $m_p = 0.1$  kg and  $J_p = 0.005$  kg m<sup>2</sup>, respectively; the hub mass and moment of inertia are  $m_{h1} = m_{h2} = 1$  kg and  $J_{h1} = J_{h2} = 0.1$  kg m<sup>2</sup>, respectively. The considered dissipation

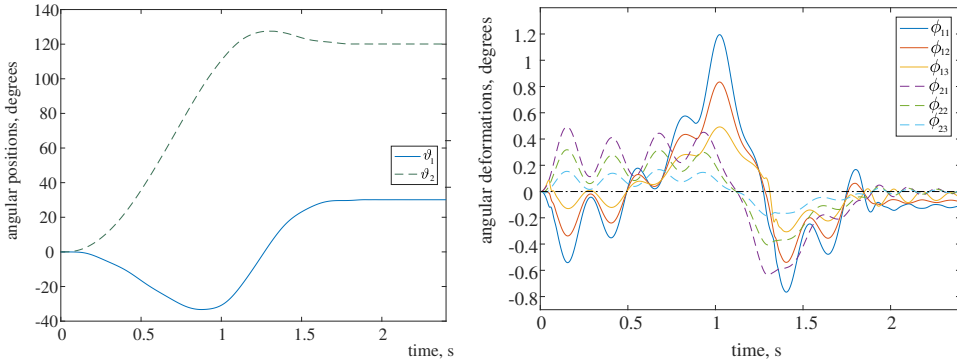


**Figure 3.** Straight trajectory: angular joint positions (left), and angular link deformations (right).

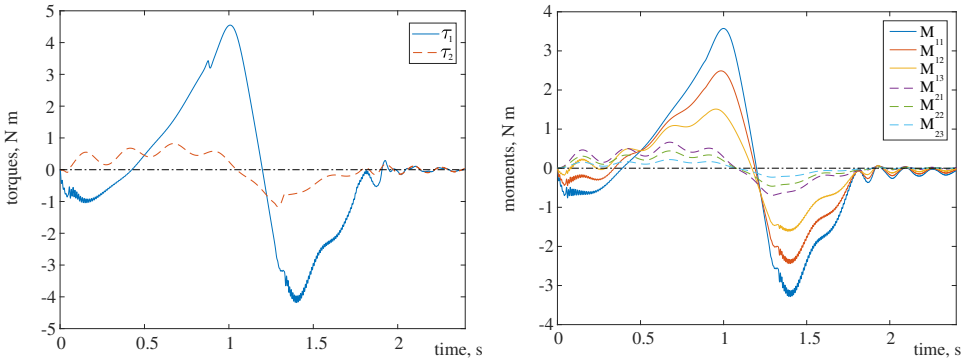


**Figure 4.** Straight trajectory: joint torques (left), and lumped moments applied to  $\varphi_{ij}$  (right).

coefficients are  $c_1 = c_2 = 0.15 \text{ N m s}$ . The parameters related to friction actions are assumed to be the same for the two joints, and specifically they are: the static friction torque  $\tau_S = 0.2 \text{ N m}$ , the Coulomb friction torque  $\tau_C = 0.1 \text{ N m}$ , the Stribeck velocity  $v_s = 0.1 \text{ rad/s}$ , and the friction coefficients  $k_1 = k_2 = 10^3 \text{ N m}$ .

As a first example, we consider the case in which the trajectory of the end effector is rectilinear, as shown by stroboscopic moving pictures in Figure 2, and lasts for 2 s. The control action consists only of torques and moments deriving from (14). The control parameters should be positive for stability reasons, and are set to be  $K_{c1} = K_{c2} = 4 \times 10^5 \text{ N/m}$ . In Figure 2 the trajectories of the link tips are highlighted in dark red for the actual motion. In particular, in Figure 3, the trajectories of the joint angles  $\vartheta_i$  and the angular deformations  $\varphi_{ij}$  are reported. We note that the angular deformations are very small for the considered trajectory

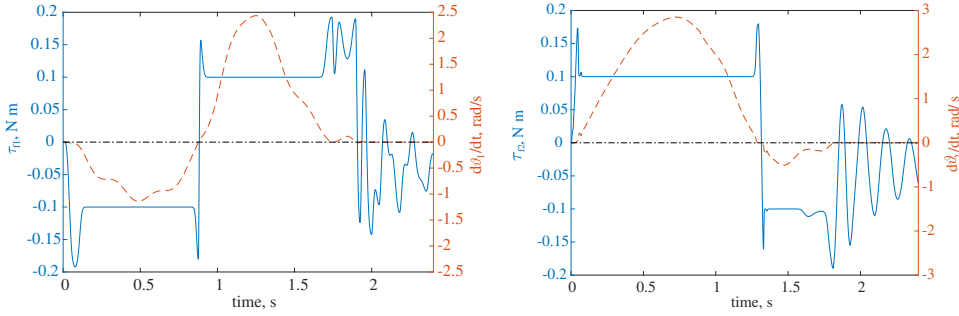


**Figure 5.** Straight trajectory: friction torque  $\tau_{f1}$  and  $\dot{\vartheta}_1$  (left), and friction torque  $\tau_{f2}$  and  $\dot{\vartheta}_2$  (right).

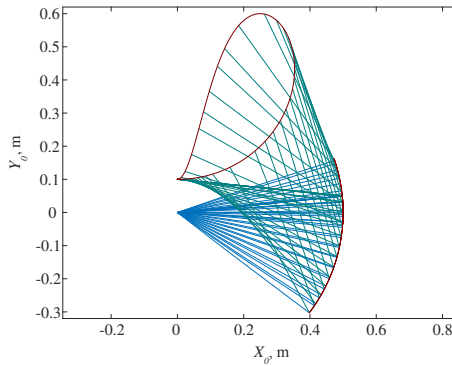


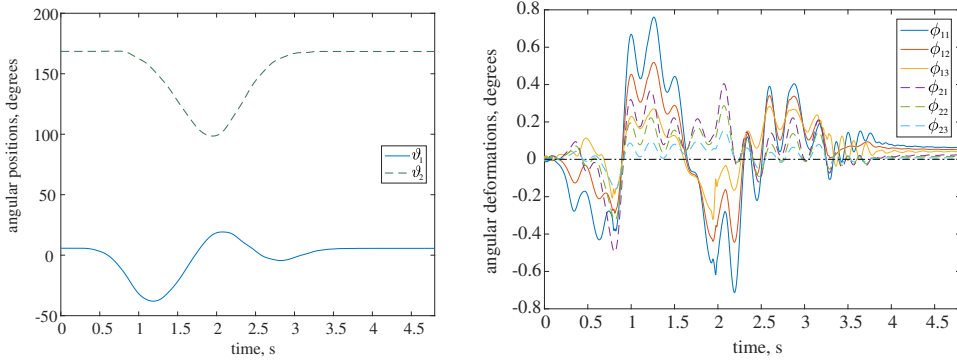
**Figure 6.** Closed loop trajectory.

planning; indeed, the maximum angular deformation associated to the variable  $\varphi_{11}$  is at most 1.2 degrees. The positioning error is not shown since it is negligible.

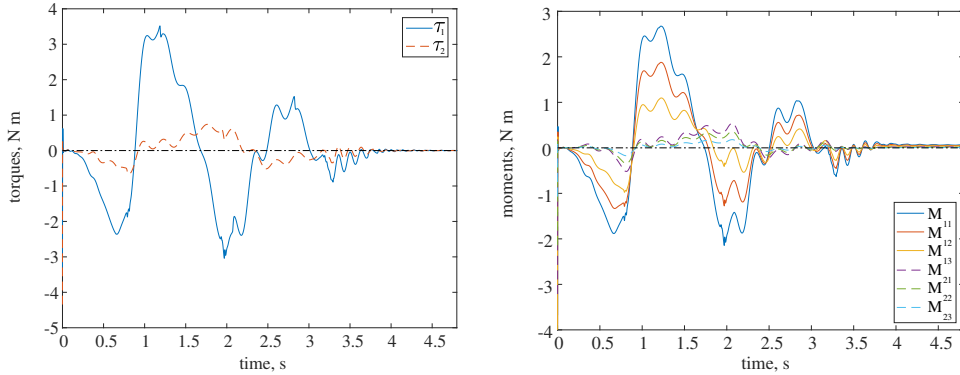
Figure 4 shows the plots of applied joint torques and the lumped moments on  $\varphi_{ij}$ , respectively. The nominal trajectory has a settling time of 2 s in order that from a technological point of view it is possible to consider motors and actuators which are reasonably powerful but not too big. Indeed, the moments required by piezoelectric actuators are easily obtained by exploiting the potentiality provided by the latest technologies.

Figure 5 shows, for the first and second joints, respectively, a comparison between the friction torques and the joint speeds. From this figure it is easy to recognize nonlinear effects such as stick-slip motion and Stribeck effect.

Finally, the case of the closed loop trajectory is considered, as shown in Figure 6. Here, the task time is set to 4 s. Regarding the control action, the control law of the previous case is improved by adding a further damping action; see (16). With this term, possible oscillations of the control actions which can cause some troubles in the real implementation, especially at the beginning, can be avoided. The damping



**Figure 7.** Closed loop trajectory: angular joint positions (left), and angular link deformations (right).



**Figure 8.** Closed loop trajectory: joint torques (left), and lumped moments (right).

control parameters are set to be  $C_{c1} = C_{c2} = 1 \times 10^3$  N s/m.

Figure 7 shows the joint angles  $\vartheta_i$  and the angular deformations  $\varphi_{ij}$  for the new case. Again, the angular deformations are very small and the maximum angular deformation associated to the variable  $\varphi_{11}$  is at most 0.8 degrees. In Figure 8, the applied joint torques and the lumped moments on  $\varphi_{ij}$  are plotted.

## 5. Conclusions

In this paper, a planar multilink robot manipulator made up of flexible beams has been modeled by means of a discrete Hencky bar-chain model. An energy-based control has been proposed and validated by numerical simulations.

The use of a Hencky bar-chain approach for space discretization has been motivated in order to consider cases in which the linearization at the basis of the assumed modes method is not feasible. Indeed, the linearization underlying the

assumed modes method would entail that the motion would be characterized by two distinct time scales: one “slower” for the overall motion and one “faster” for the superimposed vibration. Clearly, this is not possible when dealing with nonlinear systems, as the two time scales are very close and, thus, not neatly distinct.

The finite element method could potentially be suitable for solving such nonlinear problems. Nevertheless, commercial codes which are currently available are still lacking in this respect. Therefore, a homemade code would be needed. The Hencky bar-chain model, for its simplicity and accuracy, has been preferred. Indeed, increasing the number of rigid bars in the discretization results in the Hencky model converging to the nonlinear “elastica” theory. Remarkably, in the case of the proposed control, using a nonlinear model does not entail an excessive computational burden as when employing the computed torque approach which, differently from the energy-based control applied herein to the Hencky bar-chain model, requires the online solution of the whole model.

## References

- [Alessandroni et al. 2005] S. Alessandroni, U. Andreaus, F. dell’Isola, and M. Porfiri, “A passive electric controller for multimodal vibrations of thin plates”, *Comput. Struct.* **83**:15–16 (2005), 1236–1250.
- [Aminzahed et al. 2017] I. Aminzahed, M. M. Mashhadi, and M. R. V. Sereshk, “Influence of drawn radius in micro deep drawing process of rectangular work pieces via size dependent analysis using piezoelectric actuator”, *Int. J. Interact. Des. Manuf.* **11**:4 (2017), 893–902.
- [Balobanov et al. 2016] V. Balobanov, S. Khakalo, and J. Niiranen, “Isogeometric analysis of gradient-elastic 1D and 2D problems”, pp. 37–45 in *Generalized continua as models for classical and advanced materials*, edited by H. Altenbach and S. Forest, *Adv. Struct. Mater.* **42**, Springer, 2016.
- [Baroudi et al. 2019] D. Baroudi, I. Giorgio, A. Battista, E. Turco, and L. A. Igumnov, “Nonlinear dynamics of uniformly loaded *Elastica*: experimental and numerical evidence of motion around curled stable equilibrium configurations”, *Z. Angew. Math. Mech.* (online publication April 2019).
- [Bellezza et al. 1990] F. Bellezza, L. Lanari, and G. Ulivi, “Exact modeling of the flexible slewing link”, pp. 734–739 in *Proceedings of the 1990 IEEE International Conference on Robotics and Automation* (Cincinnati, OH, 1990), vol. 1, IEEE Computer Society, Los Alamitos, CA, 1990.
- [Cannon 1984] R. H. Cannon, Jr., “Initial experiments on the end-point control of a flexible one-link robot”, *Int. J. Robotics Res.* **3**:3 (1984), 62–75.
- [Cazzani et al. 2016] A. Cazzani, M. Malagù, and E. Turco, “Isogeometric analysis of plane-curved beams”, *Math. Mech. Solids* **21**:5 (2016), 562–577.
- [Chróścielewski et al. 2019] J. Chróścielewski, R. Schmidt, and V. A. Eremeyev, “Nonlinear finite element modeling of vibration control of plane rod-type structural members with integrated piezoelectric patches”, *Contin. Mech. Thermodyn.* **31**:1 (2019), 147–188.
- [De Luca and Siciliano 1991] A. De Luca and B. Siciliano, “Closed-form dynamic model of planar multilink lightweight robots”, *IEEE Trans. Systems Man Cybernet.* **21**:4 (1991), 826–839.
- [dell’Isola et al. 2016] F. dell’Isola, I. Giorgio, M. Pawlikowski, and N. L. Rizzi, “Large deformations of planar extensible beams and pantographic lattices: heuristic homogenization, experimental and numerical examples of equilibrium”, *P. Roy. Soc. London A* **472**:2185 (2016), 20150790.

- [Dupac and Noroozi 2014] M. Dupac and S. Noroozi, “Dynamic modeling and simulation of a rotating single link flexible robotic manipulator subject to quick stops”, *Stroj. vestn. J. Mech. Eng.* **60**:7–8 (2014), 475–482.
- [Eugster et al. 2014] S. R. Eugster, C. Hesch, P. Betsch, and C. Glocker, “Director-based beam finite elements relying on the geometrically exact beam theory formulated in skew coordinates”, *Int. J. Numer. Methods Eng.* **97**:2 (2014), 111–129.
- [Feliu et al. 1992] V. Feliu, K. S. Rattan, and H. B. Brown, “Modeling and control of single-link flexible arms with lumped masses”, *ASME J. Dyn. Sys. Measure. Cont.* **114**:1 (1992), 59–69.
- [Garcea et al. 1998] G. Garcea, G. A. Trunfio, and R. Casciaro, “Mixed formulation and locking in path-following nonlinear analysis”, *Comput. Methods Appl. Mech. Eng.* **165**:1–4 (1998), 247–272.
- [Giorgio and Del Vescovo 2018] I. Giorgio and D. Del Vescovo, “Non-linear lumped-parameter modeling of planar multi-link manipulators with highly flexible arms”, *Robotics* **7**:4 (2018), 60.
- [Giorgio et al. 2019] I. Giorgio, A. Della Corte, and D. Del Vescovo, “Modelling flexible multi-link robots for vibration control: numerical simulations and real-time experiments”, *Math. Mech. Solids* **24**:1 (2019), 52–71.
- [Greco and Cuomo 2013] L. Greco and M. Cuomo, “B-spline interpolation of Kirchhoff–Love space rods”, *Comput. Methods Appl. Mech. Eng.* **256** (2013), 251–269.
- [Greco et al. 2017] L. Greco, M. Cuomo, L. Contrafatto, and S. Gazzo, “An efficient blended mixed B-spline formulation for removing membrane locking in plane curved Kirchhoff rods”, *Comput. Methods Appl. Mech. Eng.* **324** (2017), 476–511.
- [Hodges 1990] D. H. Hodges, “A mixed variational formulation based on exact intrinsic equations for dynamics of moving beams”, *Int. J. Solids Struct.* **26**:11 (1990), 1253–1273.
- [Hughes et al. 2005] T. J. R. Hughes, J. A. Cottrell, and Y. Bazilevs, “Isogeometric analysis: CAD, finite elements, NURBS, exact geometry and mesh refinement”, *Comput. Methods Appl. Mech. Eng.* **194**:39–41 (2005), 4135–4195.
- [Juang and Phan 1992] J.-N. Juang and M. Phan, “Robust controller designs for second-order dynamic systems: a virtual passive approach”, *J. Guid. Control Dynam.* **15**:5 (1992), 1192–1198.
- [Khorrami et al. 1991] F. Khorrami, S. Jain, W. Grossman, A. Tzes, and W. Blessner, “Nonlinear control with input preshaping for flexible-link manipulators”, pp. 96–101 in *Fifth International Conference on Advanced Robotics: Robots in unstructured environments* (Pisa, Italy, 1991), vol. 1, IEEE, Piscataway, NJ, 1991.
- [Kocsis et al. 2017] A. Kocsis, N. Challamel, and G. Károlyi, “Discrete and nonlocal models of Engesser and Haringx elastica”, *Int. J. Mech. Sci.* **130** (2017), 571–585.
- [Lossouarn et al. 2015] B. Lossouarn, J. F. Deü, and M. Aucejo, “Multimodal vibration damping of a beam with a periodic array of piezoelectric patches connected to a passive electrical network”, *Smart. Mater. Struct.* **24**:11 (2015), 115037.
- [Lumentut and Howard 2015] M. F. Lumentut and I. M. Howard, “Effect of shunted piezoelectric control for tuning piezoelectric power harvesting system responses—analytical techniques”, *Smart. Mater. Struct.* **24**:10 (2015), 105029.
- [Luongo and D’Annibale 2013] A. Luongo and F. D’Annibale, “Double zero bifurcation of non-linear viscoelastic beams under conservative and non-conservative loads”, *Int. J. Non-Linear Mech.* **55** (2013), 128–139.
- [Pietraszkiewicz and Eremeyev 2009] W. Pietraszkiewicz and V. A. Eremeyev, “On vectorially parameterized natural strain measures of the non-linear Cosserat continuum”, *Int. J. Solids Struct.* **46**:11–12 (2009), 2477–2480.

- [Placidi et al. 2017] L. Placidi, E. Barchiesi, and A. Battista, “An inverse method to get further analytical solutions for a class of metamaterials aimed to validate numerical integrations”, pp. 193–210 in *Mathematical modelling in solid mechanics*, edited by F. dell’Isola et al., Adv. Struct. Mater. **69**, Springer, 2017.
- [Ramachandran et al. 1992] S. Ramachandran, T. Nagarajan, and N. Siva Prasad, “A finite element approach to the design and dynamic analysis of platform type robot manipulators”, *Finite Elem. Anal. Des.* **10**:4 (1992), 335–350.
- [Rosi et al. 2018] G. Rosi, L. Placidi, and N. Auffray, “On the validity range of strain-gradient elasticity: a mixed static–dynamic identification procedure”, *Eur. J. Mech. A Solids* **69** (2018), 179–191.
- [Rubinstein 1999] D. Rubinstein, “Dynamics of a flexible beam and a system of rigid rods, with fully inverse (one-sided) boundary conditions”, *Comput. Methods Appl. Mech. Eng.* **175**:1–2 (1999), 87–97.
- [Sharf 1996] I. Sharf, “Geometrically non-linear beam element for dynamics simulation of multi-body systems”, *Int. J. Numer. Methods Eng.* **39**:5 (1996), 763–786.
- [Spagnuolo and Andreus 2019] M. Spagnuolo and U. Andreus, “A targeted review on large deformations of planar elastic beams: extensibility, distributed loads, buckling and post-buckling”, *Math. Mech. Solids* **24**:1 (2019), 258–280.
- [Theodore and Ghosal 1995] R. J. Theodore and A. Ghosal, “Comparison of the assumed modes and finite element models for flexible multilink manipulators”, *Int. J. Rob. Res.* **14**:2 (1995), 91–111.
- [Turco 2018] E. Turco, “Discrete is it enough? The revival of Piola–Hencky keynotes to analyze three-dimensional *elastica*”, *Contin. Mech. Thermodyn.* **30**:5 (2018), 1039–1057.
- [Turco et al. 2016] E. Turco, F. dell’Isola, A. Cazzani, and N. L. Rizzi, “Hencky-type discrete model for pantographic structures: numerical comparison with second gradient continuum models”, *Z. Angew. Math. Phys.* **67**:4 (2016), 85.
- [Wang et al. 2015] C. M. Wang, H. Zhang, R. P. Gao, W. H. Duan, and N. Challamel, “Hencky bar-chain model for buckling and vibration of beams with elastic end restraints”, *Int. J. Struct. Stab. Dyn.* **15**:7 (2015), 1540007.
- [Weeger et al. 2013] O. Weeger, U. Wever, and B. Simeon, “Isogeometric analysis of nonlinear Euler–Bernoulli beam vibrations”, *Nonlinear Dynam.* **72**:4 (2013), 813–835.
- [Canudas de Wit et al. 1995] C. Canudas de Wit, H. Olsson, K. J. Åström, and P. Lischinsky, “A new model for control of systems with friction”, *IEEE Trans. Automat. Control* **40**:3 (1995), 419–425.
- [Yildizdag et al. 2018] M. E. Yildizdag, M. Demirtas, and A. Ergin, “Multipatch discontinuous Galerkin isogeometric analysis of composite laminates”, *Contin. Mech. Thermodyn.* (online publication July 2018).

Received 27 Dec 2018. Revised 17 Feb 2019. Accepted 20 Mar 2019.

IVAN GIORGIO: [ivan.giorgio@uniroma1.it](mailto:ivan.giorgio@uniroma1.it)

Department of Mechanical and Aerospace Engineering, Università di Roma “La Sapienza”, Italy

and

International Research Center on Mathematics and Mechanics of Complex Systems,  
Università degli studi dell’Aquila, Italy

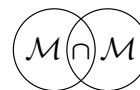
DIONISIO DEL VESCOVO: [dionisio.delvescovo@uniroma1.it](mailto:dionisio.delvescovo@uniroma1.it)

Department of Mechanical and Aerospace Engineering, Università di Roma “La Sapienza”, Italy

and

International Research Center on Mathematics and Mechanics of Complex Systems,  
Università degli studi dell’Aquila, Italy





## A MODEL OF THE PROPPANT FLOWBACK SETUP OF THE THEORETICAL FRAMEWORK

KSENIA P. FROLOVA,  
POLINA M. GRIGOREVA, KONSTANTIN E. LEZHNEV  
AND GRIGORIY V. PADERIN

Proppant flowback control is one of the main issues in hydraulic fracture modeling since the propping agent maintains the crack in an open state and therefore provides oil inflow to the wellbore. The main objective of this paper is to determine the conditions that can lead to proppant flowback during the direct operation of the well. The main outcome of this paper is an evolution criterion for proppant flowback occurrence, which takes the external pressures affecting the proppant particles, the proppant properties, and the crack opening width into account. We propose a two-component continuum model consisting of the proppant and the oil to find the stress-strain state of the proppant and thereby to obtain the stress components in the evolution criterion. We solve both a stationary problem for estimating the probability of the proppant flowback occurrence under regular conditions as well as a transient problem for taking the possibility of fast changing external conditions into account.

### 1. Introduction

Proppant flowback is a process of producing a propping agent from a hydraulically created cleavage fracture during extraction of the hydrocarbons or treatment of the wellbore. This process can significantly increase well operation costs due to decreases in the crack permeability when the proppant pack used for keeping it open is removed leading to its closure. Moreover, the entrained proppant moves with the fluid to the wellbore and increases the risk of mechanical damage of the wellbore equipment.

Proppant flowback and its mechanisms were extensively studied over the last 30 years due to the importance of its control. One of the first lab experiments used for studying the stability of a proppant pack is described in [Milton-Taylor et al. 1992]. It was shown that the fracture width, the closure stress, the pressure

---

**Communicated by Francesco dell’Isola.**

*MSC2010:* 70E50, 70E55, 74B15, 74F10, 76S05.

*Keywords:* proppant flowback, breakdown criterion, two-component continua, hydraulic fracture, pack stability, linear-elastic solid, rational mechanics approach.

drawdown, and the proppant properties are key parameters affecting the proppant pack stability. Then a distinct-element model (DEM) of the proppant pack was conceived, which provided numerical results proving the laboratory data [Asgian et al. 1995]. Calculations performed for interacting cohesionless, unbonded proppant grains subjected to a drag force showed that the pack becomes unstable when a crucial ratio of mean grain diameter to the fracture width is reached. This numerical modeling also revealed the mechanism of proppant pack instability. At widths less than a critical value, a stable proppant arch is formed at the proppant pack face. This arch suffers deformations from compressive strains, resists extrusive stresses, and keeps the rest of the proppant grains inside the crack. If the drag forces are sufficiently high to make the arch fail, proppant production is started.

Some experiments on proppant flowback for proppants of different properties and a very simple mathematical model can also be found in [McLennan et al. 2015]. This model offers a phenomenological dependence of pressure in a proppant pack on oil production rate. In [Andrews and Kj rholt 1998] a phenomenological proppant pack stability criterion was suggested. It describes the proppant pack behavior in terms of a proppant free wedge concept, which states that in a three-dimensional space with axes of closure stresses, pressure drawdown, and fracture width there is a shell, the points inside of which are points of proppant pack stability. According to this concept, the maximum stable fracture function was chosen in a polynomial form when fitting the experiment results. However, this choice shows that this criterion is incorrect for the case of critical condition values. In later work (e.g., in [Canon et al. 2003]) the criterion was corrected, but as it was based on measurement results that cannot be determined perfectly, such phenomenological criteria could give only an approximate probability for the start of proppant flowback. A model taking the ability of proppant flowback to stop with the closure of the crack or a decrease of the drag force into account should be more complex and preferably include time dependence and cumulative effects.

Some complex models for proppant flowback were already developed in [Aidagulov et al. 2007]. They include plastic flow of the proppant after pack stability loss and changes in porosity. These are significant when calculating the crack permeability. Nevertheless, the criterion for the beginning of proppant flowback is still determined phenomenologically: it is based on a Mohr–Coulomb failure criterion, which does not describe the mechanism of proppant arch crushing, and therefore can give only approximate results.

In summary, we can say that the development of the criteria of the proppant flowback is still of interest in science and industry. The criteria developed in this paper and the corresponding model will not only predict the beginning of the proppant flowback but also determine “safe” regimes of hydrocarbon production and wellbore treatment.

## 2. Flowback criterion

Presently there exists no widely known criterion for proppant pack stability loss that takes all the main factors into account that, according to experimental studies, primarily affect the flowback, namely the ratio of the width of the crack opening to the diameter of the proppant grains, as well as the type and coating of the proppant. The phenomenological dependencies that were proposed in the literature acknowledge only the influence of a few specific factors. Flowback criteria proposed in continuum models do not consider the effects of the discreteness of the proppant pack. Discrete models are not based on criteria that consider the stress state of the whole modeling area. In the proposed model an attempt is made to take the most important conditions affecting proppant flowback into account and to describe more accurately the process that occurs when proppant pack stability is lost.

The purpose of this paper is to determine conditions under which the proppant is produced during the direct treatment of the wellbore. Generally, the main reasons for the flowback are

- low stresses acting on the fracture walls, which cannot keep the proppant in the crack,
- a huge force of hydrodynamic resistance, acting on proppant particles, which leads to a loss of stability of the proppant pack, and
- accumulation of internal stresses and deformations during long-term operation of the well and its cyclic use.

In addition to the above-listed reasons of flowback following from the experimental results presented in literature [Vo et al. 2014; Lu et al. 2016], the form and coating of the proppant grains affecting the internal friction forces between individual proppant particles have a significant effect on the removal process, which in turn affects the stability of the proppant pack. Furthermore, from experimental data and from results when modeling the proppant removal process by the distinct element method, it follows that the packing becomes unstable, starting with a certain ratio of the average grain diameter to the width of the crack opening.

We consider the known mechanism of the stability loss when the proppant flowback starts after the failure of the arch formed by proppant particles [Asgian et al. 1995]. Within the framework of our model, the compressive stresses holding the proppant particles in the arch are the principal stresses in the proppant acting along the axis directed perpendicular to the axis of the crack. Drag forces lead to the main stresses in the proppant, which are directed along the axis of the crack. We assume that a Coulomb dry friction force acts between the proppant particles. The corresponding friction coefficient depends on the surface roughness of the proppant,

its coating, and other cohesive properties. This takes one of the important factors influencing the proppant transport into account.

As mentioned above, the main reasons affecting the proppant transport are the closure stress, the flow rate of the fluid through the proppant pack, and the ratio of the proppant grain diameter to the crack opening width. The influence of the closing stress and the flow rate on the stability of proppant pack can be taken into account mechanically, whereas the effect of the mentioned ratio is described mostly empirically. The experiments show that a proppant pack with one or two proppant particles in the arch is stable even at the low closure stresses and high fluid rates. However, if the crack width is too big, namely starting from 6–10 proppant grains (depending on the type of proppant; see, e.g., [Andrews and Kj rholm 1998; Barree and Conway 2001]), the flowback occurs at most of the treatment regimes. That means that starting with some value the discreteness of the arch plays a role no more. Concluding all the mentioned reasons, we suggest the flowback criterion

$$\mu_p T_{pzz} < T_{pxx} k \left[ 1 - \exp\left(\frac{d - z_0}{z_0}\right) \right], \quad (1)$$

where  $\mu_p$  is the coefficient of dynamic viscosity of proppant,  $T_{pzz}$  and  $T_{pxx}$  are the components of the stress tensor of proppant acting in the directions of the crack opening and the crack length, respectively,  $k$  is the correction factor,  $d$  is the diameter of the proppant grain, and  $z_0 = z_2 - z_1$  is the fracture width, where  $z_1$  and  $z_2$  are the coordinates of the crack edges. The exponential expression is motivated by a three-parameter Weibull distribution characterizing, for example, the statistical variation of bending strength in brittle materials, such as glass or ceramics. In this context, the parameter  $z_0$  in the numerator and in the denominator would, in general, be different. The  $z_0$  in the numerator would be a characteristic threshold stress under which no failure can occur, whereas the  $z_0$  in the denominator is simply a suitable normalization stress (see [Manderscheid and Gyekenyesi 1987] for details, especially the discussion around (1)). Here, obviously, both have been taken as equal for simplicity.

If we want the criterion not to be fulfilled such that, consequently, no flowback occurs, it is necessary for the closure stress to be large enough to exceed the stress tending to push the proppant particle out of the arch with some factor increasing with increasing crack opening width. In order to make the flowback criterion meaningful, this parameter  $k$  should be chosen such that, at a critical ratio of the diameter of the proppant particle to the width of the crack opening, the multiplier is approximately equal to 1. The value of the parameter  $k$  differs with the value of the critical ratio: for  $z_0/d \approx 5.5$  [Andrews and Kj rholm 1998]  $k$  is equal to 1.79 and for  $z_0/d \approx 10$  [Barree and Conway 2001]  $k$  is equal to 1.67.

In addition, it should be taken into account that (1) is a local criterion, which can be violated at several points inside of the proppant pack. Then flowback would still not happen. Thus, this criterion is a “lower estimate” for the critical values of the production conditions at which the proppant will not be taken out. For a more accurate assessment, one can introduce an integral criterion, which will take the number of violations of this criterion throughout the entire volume of the proppant pack into account.

It should also be noted that in this paper the proppant removal process itself is not modeled. This process can be described by using proppant transport models based on multiphase medium mechanics models, which are widely used when describing proppant placement processes in a crack.

### 3. Physicomathematical model

According to the proppant flowback criterion presented in the previous section, it is necessary to know the values of the stress tensor components  $T_{pzz}$  and  $T_{pxx}$  apart from the proppant properties and the fracture geometry in order to estimate as to whether proppant flowback occurs. In this spirit, we present a model, which allows one to obtain the stress-strain state of a propping agent under loading.

The proppant behavior under loading can be described within different approaches, namely discrete, continuum, and crossbred ones. In this paper, we follow the continuum approach. This is motivated primarily by the fact that discrete models mostly describe the proppant flowback mechanism, but do not allow one to estimate the propping agent properties before and after the start of the flowback. Moreover, calculations based on the continuum model will take much less time than those involved in a discrete model.

We model a single transverse crack initiated in a horizontal well filled with a tightly packed proppant and oil flowing through. As has been already mentioned in the section devoted to the flowback criterion, we do not model the proppant removal process. In this respect, we solve a quasistatic problem for the proppant. We consider the deformation of the propping agent affected by the oil flow and take the possibility of occurring vacancies into account.

For a more accurate prediction of the proppant behavior, both stationary and nonstationary laminar oil flows are considered. The stationary flow of oil through a packed proppant allows one to investigate the influence of various physical and mechanical proppant properties on its behavior. Considering a transient flow of oil allows one to take a changing borehole pressure, changes in the rate of the oil flow, a pause and subsequent resumption of the well treatment, etc., into account.

To find the stress-strain state of the proppant, we consider a two-component continuum consisting of proppant and oil. We assume that at each point of space both

fluid and proppant are simultaneously present. Their partial densities determine the mass fractions of each of the components. Note that we allow the possibility of the vacancies' occurrence by considering the proppant density as a function of space coordinates and time. Some information on continuum mixture theory relevant to this paper can be found in [Brazgina et al. 2016].

The wellbore and the rock surrounding the fracture are not considered directly in the framework of the investigated model and are not included as additional components in the multicomponent media. Their presence is accounted through boundary conditions.

When modeling each component of the continuum, it becomes necessary to establish the corresponding constitutive relations. In this context, we use some simplifying hypotheses.

Generally, the proppant is considered as a granular material. However, since in the present case the proppant is the only reason for preventing cleavage closing under the pressure caused by the surrounding rock, it has a sufficiently high density. According to numerical simulations and experimental evidence, such granular media possess not only volumetric, but also shear stiffness and their behavior are the same as for an elastically deformable solid under pressure. Moreover, we assume that the proppant, repacked after hydraulic fracturing is finished, undergoes small deformations. Finally, we assume the material of the propping agent to be isotropic.

The second component of the model, usually oil, is considered as a weakly compressible Newtonian fluid in order to satisfy experimental observations. Different correlations are used for different types of oil in order to determine the effect of the applied pressure on the oil compressibility. Since in this paper we would like to outline and study the general problem of proppant flowback and to predict as to whether it occurs or not, we assume that the oil is an incompressible fluid.

**3.1. Balance and constitutive equations.** We introduce a Cartesian coordinate system  $(x, y, z)$ , where the  $x$  axis coincides with the direction of the crack length, the  $z$  axis with the direction of its opening width, and the  $y$  axis with the direction of the crack aperture (see Figure 1).

The mass balance for both components, namely oil and proppant, is

$$\frac{\delta_i \rho_i}{\delta t} + \rho_i \nabla \cdot \mathbf{v}_i = 0, \quad (2)$$

where subscript  $i = f, p$  refers to the components of the fluid or of the proppant, respectively,  $\rho$  is the density,  $\mathbf{v}_i$  is the velocity, and  $\nabla$  is the differential operator with respect to spatial coordinates. The substantial (material) derivative  $\delta_i/\delta t$  of a field quantity  $\phi$  is defined as

$$\frac{\delta_i \phi(\mathbf{r}, t)}{\delta t} = \frac{\partial \phi(\mathbf{r}, t)}{\partial t} + \mathbf{v}_i \cdot \nabla \phi(\mathbf{r}, t), \quad (3)$$

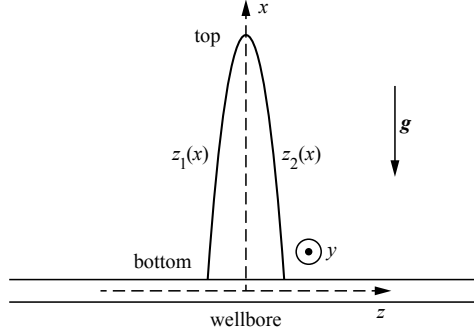


**Figure 1.** Schematic representation of the fracture.

where  $\mathbf{r}$  is the position vector of the control volume (point of observation) or in other words of the certain area in space through which the structure moves as time passes (see, e.g., [Ivanova et al. 2016]).

Since the fluid is assumed as incompressible, the substantial derivative in (2) is equal to zero for the fluid component. Thus, the mass balance for the oil leads to the incompressibility constraint

$$\nabla \cdot \mathbf{v}_f = 0. \quad (4)$$

The deformations of the proppant are supposed to be small, and the mass balance for the proppant component reduces to the following equation for the proppant density:

$$\rho_p(\mathbf{r}, t) = \rho_p(\mathbf{r}, 0)[1 + \text{tr}(\boldsymbol{\epsilon}_p(\mathbf{r}, t))], \quad (5)$$

where  $\text{tr}(\boldsymbol{\epsilon}_p)$  is the first invariant of strain tensor  $\boldsymbol{\epsilon}_p$ .

The balance of momentum for both components in the local form reads

$$\rho_i \frac{\delta_i \mathbf{v}_i}{\delta t} = \rho_i \mathbf{f}_e + \mathbf{f}_{\text{in}} + \nabla \cdot \mathbf{T}_i, \quad (6)$$

where  $\mathbf{f}_e$  is the external body force density,  $\mathbf{f}_{\text{in}}$  is the internal volumetric force density, and  $\mathbf{T}_i$  is the Cauchy stress tensor.

Gravity is the only external body force. The internal volumetric force represents the interaction between two continua, namely oil and proppant. This force should depend on the densities of both components and be eliminated in the balance equation for the whole media. The internal volumetric force can be written as

$$\mathbf{f}_{\text{in}} = \frac{\rho_f \rho_p}{\rho_f + \rho_p} \mathbf{f}_{fp}^d, \quad (7)$$

where  $\mathbf{f}_{fp}^d$  is the interaction force between oil and proppant per unit mass.

The interaction between fluid and proppant is due to the presence of viscous frictional forces caused between two continua when the oil flows through a proppant pack. The occurring friction depends on the relative velocity of the components. The main parameter determining the magnitude of the corresponding force is the coefficient of viscous friction between the two components, which depends on many factors, including the type of proppant coating, its size and shape, the rheological properties of oil, etc.

Here, we assume a linear dependence of the dissipative components of the forces on the difference in the velocities of the two components. Since we solve a quasistatic problem for the proppant and do not consider the proppant motion, the following equation holds:

$$\mathbf{f}_{fp}^d = \mu_{fp} \mathbf{v}_f, \quad (8)$$

where  $\mu_{fp}$  is the coefficient of viscous friction between proppant and oil.

Thus, the balance of momentum for fluid in the local form can be rewritten as

$$\rho_f \left( \frac{\partial \mathbf{v}_f}{\partial t} + \mathbf{v}_f \cdot \nabla \mathbf{v}_f \right) = \rho_f \mathbf{g} + \frac{\rho_f \rho_p}{\rho_f + \rho_p} \mathbf{f}_{fp}^d + \nabla \cdot \mathbf{T}_f, \quad (9)$$

where  $\mathbf{g}$  is the gravitational acceleration.

Note that in the stationary case the partial derivative in (9) is absent, because the flow is steady and the velocity in each point of observation does not change with time.

The appropriate constitutive relation for a linear incompressible fluid reads

$$\mathbf{T}_f = -\rho_f \mathbf{E} + \frac{\rho_f}{\rho_f + \rho_p} 2\mu_f (\nabla \mathbf{v})^s, \quad (10)$$

where  $p_f$  is the hydrostatic oil pressure,  $\mathbf{E}$  is the unit tensor,  $\mu_f$  is the coefficient of dynamic viscosity of the oil, and  $(\nabla \mathbf{v})^s$  is the symmetric part of the velocity gradient.

Since a quasistatic proppant behavior is considered, the balance of momentum for proppant reduces to

$$\rho_p \mathbf{g} - \frac{\rho_f \rho_p}{\rho_f + \rho_p} \mathbf{f}_{fp}^d + \nabla \cdot \mathbf{T}_p = 0. \quad (11)$$

We suppose the proppant to be a linear isotropic elastic material satisfying Hooke's law:

$$\mathbf{T}_p = \frac{\rho_p}{\rho_f + \rho_p} \left( \frac{E\nu}{(1+\nu)(1-2\nu)} \text{tr}(\boldsymbol{\varepsilon}_p) \mathbf{E} + \frac{E}{1+\nu} \boldsymbol{\varepsilon}_p \right), \quad (12)$$

where  $E$  and  $\nu$  are Young's modulus and Poisson's ratio, respectively,  $\boldsymbol{\varepsilon}_p$  is the linear strain tensor of the proppant, and  $\boldsymbol{\varepsilon}_p = (\nabla \mathbf{u}_p)^s$ , where  $\mathbf{u}_p$  is the proppant displacement.

Finally, let us assume that all variables do not depend on the  $y$  coordinate so that we can consider a state of plane-strain. Then by taking all of the simplifications into account, the whole system of equations in coordinate form is given by (13)–(19):

- equation for the proppant density

$$\rho_p(\mathbf{r}, t) = \rho_p(\mathbf{r}, 0) \left( 1 + \frac{\partial u_x}{\partial x} + \frac{\partial u_z}{\partial z} \right), \quad (13)$$

- incompressibility condition for the oil

$$\frac{\partial v_{fx}}{\partial x} + \frac{\partial v_{fz}}{\partial z} = 0, \quad (14)$$

- the balance of momentum for the oil along the  $x$  axis

$$\begin{aligned} & \rho_f \left[ \frac{\partial v_{fx}}{\partial t} + v_{fx} \frac{\partial v_{fx}}{\partial t} + v_{fz} \frac{\partial v_{fx}}{\partial z} \right] \\ &= -\rho_f g - \frac{\partial p_f}{\partial x} + \frac{\rho_f \rho_p}{\rho_f + \rho_p} \mu_{fp} v_{fx} + \frac{\rho_f}{\rho_f + \rho_p} \mu_f \left[ \frac{\partial^2 v_{fx}}{\partial x^2} + \frac{1}{2} \left( \frac{\partial^2 v_{fx}}{\partial z^2} + \frac{\partial^2 v_{fz}}{\partial z \partial x} \right) \right] \\ & \quad - \frac{\rho_f}{(\rho_f + \rho_p)^2} \mu_f \left[ \frac{\partial v_{fx}}{\partial x} \frac{\partial \rho_p}{\partial x} + \frac{1}{2} \left( \frac{\partial v_{fz}}{\partial x} + \frac{\partial v_{fx}}{\partial z} \right) \frac{\partial \rho_p}{\partial z} \right], \quad (15) \end{aligned}$$

- the balance of momentum for the oil along the  $z$  axis

$$\begin{aligned} & \rho_f \left[ \frac{\partial v_{fz}}{\partial t} + v_{fx} \frac{\partial v_{fz}}{\partial x} + v_{fz} \frac{\partial v_{fz}}{\partial z} \right] \\ &= -\frac{\partial p_f}{\partial z} + \frac{\rho_f \rho_p}{\rho_f + \rho_p} \mu_{fp} v_{fz} + \frac{\rho_f}{\rho_f + \rho_p} \mu_f \left[ \frac{\partial^2 v_{fz}}{\partial z^2} + \frac{1}{2} \left( \frac{\partial^2 v_{fz}}{\partial x^2} + \frac{\partial^2 v_{fx}}{\partial x \partial z} \right) \right] \\ & \quad - \frac{\rho_f}{(\rho_f + \rho_p)^2} \mu_f \left[ \frac{\partial v_{fz}}{\partial z} \frac{\partial \rho_p}{\partial z} + \frac{1}{2} \left( \frac{\partial v_{fz}}{\partial z} + \frac{\partial v_{fx}}{\partial z} \right) \frac{\partial \rho_p}{\partial x} \right], \quad (16) \end{aligned}$$

- the balance of momentum for the proppant along the  $x$  axis

$$\begin{aligned} & \rho_p g - \frac{\rho_f \rho_p}{\rho_f + \rho_p} \mu_{fp} v_{fx} \\ & + \frac{\rho_p}{\rho_p + \rho_f} \frac{E}{1+\nu} \left[ \frac{1}{2} \left( \frac{\partial^2 u_{pz}}{\partial z \partial x} + \frac{\partial^2 u_{px}}{\partial z^2} \right) + \frac{1-\nu}{1-2\nu} \frac{\partial^2 u_{px}}{\partial x^2} + \frac{\nu}{1-2\nu} \frac{\partial^2 u_{pz}}{\partial x \partial z} \right] \\ & - \frac{\rho_f}{(\rho_f + \rho_p)^2} \frac{E}{1+\nu} \left[ \frac{\partial \rho_p}{\partial x} \left( \frac{1-\nu}{1-2\nu} \frac{\partial u_{px}}{\partial x} + \frac{\nu}{1-2\nu} \frac{\partial u_{pz}}{\partial z} \right) + \frac{1}{2} \left( \frac{\partial u_{pz}}{\partial x} + \frac{\partial u_{px}}{\partial z} \right) \frac{\partial \rho_p}{\partial z} \right] = 0, \quad (17) \end{aligned}$$

- the balance of momentum for the proppant along the  $z$  axis

$$\begin{aligned}
 & -\frac{\rho_f \rho_p}{\rho_f + \rho_p} \mu_{fp} v_{fz} \\
 & + \frac{\rho_p}{\rho_p + \rho_f} \frac{E}{1+\nu} \left[ \frac{1}{2} \left( \frac{\partial^2 u_{pz}}{\partial x^2} + \frac{\partial^2 u_{px}}{\partial x \partial z} \right) + \frac{1-\nu}{1-2\nu} \frac{\partial^2 u_{pz}}{\partial z^2} + \frac{\nu}{1-2\nu} \frac{\partial^2 u_{px}}{\partial x \partial z} \right] \\
 & - \frac{\rho_f}{(\rho_f + \rho_p)^2} \frac{E}{1+\nu} \left[ \frac{\partial \rho_p}{\partial z} \left( \frac{1-\nu}{1-2\nu} \frac{\partial u_{pz}}{\partial x} + \frac{\nu}{1-2\nu} \frac{\partial u_{px}}{\partial x} \right) + \frac{1}{2} \left( \frac{\partial u_{pz}}{\partial x} + \frac{\partial u_{px}}{\partial z} \right) \frac{\partial \rho_p}{\partial x} \right] = 0,
 \end{aligned} \tag{18}$$

- and flowback criterion in the coordinate form

$$\mu_p \left( (1-\nu) \frac{\partial u_{pz}}{\partial z} + \nu \frac{\partial u_{px}}{\partial x} \right) < \left( (1-\nu) \frac{\partial u_{px}}{\partial x} + \nu \frac{\partial u_{pz}}{\partial z} \right) k \left[ 1 - \exp\left( -\frac{d-z_0}{z_0} \right) \right]. \tag{19}$$

**3.2. Boundary and initial conditions.** The initial distribution of the proppant grains along the fracture and the final shape of the fracture are supposed to be known, e.g., from a solution of the corresponding boundary-value problem.

As has been mentioned already, the presence of the wellbore and the rock surrounding the fracture will be accounted for by the boundary conditions, namely the pressures at the fracture edges and at the bottom of the crack and its tip.

When modeling hydraulic fracture usually it is assumed that the value of the pressure acting at the crack edges at the initial time is equal or close to the value of the rock pressure. The function of the pressure decrease depends on the amount of fluid flow. Note that this pressure depends only on the oil flow and does not depend on the proppant behavior. It means that one can suppose that the rock is acting only on oil:

$$T_{fzz}|_{z_1(x)} = P_r, \quad T_{fzz}|_{z_2(x)} = -P_r, \tag{20}$$

where  $T_{fzz}$  is the component of the stress tensor of oil acting in the direction of the crack opening,  $z_1(x)$  and  $z_2(x)$  are functions with respect to the crack edges (see Figure 1), and  $P_r$  is the rock pressure.

Apart from the rock pressure, there is closure stress acting at the crack edges. So in fact both rock pressure and closure stress act on the two-component continuum. Equation (20) leads to the assumption that the closure stress affects only the proppant (since the rock pressure acts on only the oil) and does not affect the oil. Such an assumption is correct from the mechanical point of view since the proppant does not allow for closing the fracture. Hence, the proppant particles are most affected by the stress that tends to close the crack edges. Consequently, the following boundary conditions hold:

$$T_{pzz}|_{z_1(x)} = \sigma_r, \quad T_{pzz}|_{z_2(x)} = -\sigma_r, \tag{21}$$

where  $\sigma_r$  is the closure stress. Many authors note that this stress affects proppant flowback and consider it as one of the main terms to control the proppant flowback [Milton-Taylor et al. 1992; Asgian et al. 1995; McLennan et al. 2015; Andrews and Kj rholt 1998; Canon et al. 2003; Aidagulov et al. 2007; Vo et al. 2014; Lu et al. 2016; Barree and Conway 2001; Larsen and Smith 1985; Ely et al. 1990]. The value of the closure stress is significant enough to hold the packed proppant in the fracture even when the outgoing force is big enough.

Apart from stresses acting at the crack edges, it is necessary to take into account the oil flow along the crack's boundary. If the fracture geometry is simple, it is permissible to assume that the inflow is perpendicular to the fracture boundary. Hence, the following conditions hold:

$$\begin{aligned} \mathbf{t} \cdot \mathbf{v}_f|_{z_1(x)} &= 0, & \rho_f \mathbf{n} \cdot \mathbf{v}_f|_{z_1(x)} &= D(\rho_f - \rho_f^p)|_{z_1(x)}, \\ \mathbf{t} \cdot \mathbf{v}_f|_{z_2(x)} &= 0, & \rho_f \mathbf{n} \cdot \mathbf{v}_f|_{z_2(x)} &= D(\rho_f - \rho_f^p)|_{z_2(x)}, \end{aligned} \quad (22)$$

where  $\mathbf{t}$  is the vector tangent to the fracture boundary,  $\mathbf{n}$  is the outer normal vector,  $D$  is the oil permeability coefficient, and  $\rho_f^p$  is the oil concentration in the rock.

We assume that the proppant particles at the crack edges adhere to them. It means that these particles cannot be removed from the crack. From a mechanical point of view, this assumption can be justified by the fact that the velocity of the laminar flow of oil and, accordingly, the probability of proppant transport are higher when approaching from the periphery to the center of the channel formed by the cleavage. Then the components of displacement at the boundary read

$$u_{px}|_{z_1(x) \cdot z_2(x)} = u_{pz}|_{z_1(x) \cdot z_2(x)} = 0. \quad (23)$$

Finally, it is necessary to define the boundary conditions at the bottom of the crack and at its tip. We assume that there is a pressure difference inside of the crack initiated by a bottom stress and the rock pressure.

In the case of a stationary problem, there will be a constant pressure difference, whereas in the case of a transient flow it is necessary to allow for the possibility of changes in the external conditions. Practically, such changes are usually very fast and can be observed in the case when the bottom pressure, determined by the operating conditions, significantly changes in time. Then the boundary conditions should depend on time and vary according to a certain prescribed law.

The following conditions hold:

$$T_{fxx}|_{x=0} = P_b, \quad T_{fxx}|_{x=l_f} = -P_r, \quad (24)$$

where  $T_{fxx}$  is the component of the stress tensor of oil acting in the directions of the fracture length,  $l_f$  is the fracture length, and  $P_b$  is the bottom pressure.

Finally, in order to solve the nonstationary problem, it is necessary to set the

initial conditions for the oil flow velocity and for the proppant displacement. We assume that at the initial moment the following conditions hold:

$$v_{fx}|_{t=0} = v_{fz}|_{t=0} = 0, \quad u_{px}|_{t=0} = u_{pz}|_{t=0} = 0. \quad (25)$$

#### 4. Conclusion

In this paper, a local stability criterion is proposed in order to verify the possible occurrence of proppant flowback as a function of the physical and mechanical properties of the proppant and of the oil, the external pressures, the geometric dimensions of the fracture, and the ratio of the average proppant particle size to the crack opening width. In order to obtain the stress components involved in the developed criterion, a physicomathematical model for the determination of the proppant strain-stress state was presented. The proposed model is based on a continuum description of a two-component medium consisting of oil, modeled by the Newtonian incompressible fluid, and the proppant, modeled by a linear-elastic deformable solid. We considered steady-state oil flow for estimating the probability of proppant flowback occurrence under regular conditions and transient flow for taking the possibility of fast changing of the external conditions into account.

#### Acknowledgments

This work was supported by the Ministry of Science and Higher Education of the Russian Federation within the framework of the Federal Program “Research and development in priority areas for the development of the scientific and technological complex of Russia for 2014–2020” (activity 1.2), grant No. 14.575.21.0146 of 26 September 2017, unique identifier: RFMEFI57517X0146. The industrial partner of the grant is LLC Gazprom-neft Science & Technology Centre.

#### References

- [Aidagulov et al. 2007] G. R. Aidagulov, M. J. Thiercelin, V. N. Nikolaevskiy, S. Kapustyanskiy, and A. Zhilenkov, “Prediction of long-term proppant flowback in weak rocks”, in *SPE Hydraulic Fracturing Technology Conference* (College Station, TX, 2007), Society of Petroleum Engineers, Richardson, TX, 2007.
- [Andrews and Kjörholt 1998] J. S. Andrews and H. Kjörholt, “Rock mechanical principles help to predict proppant flowback from hydraulic fractures”, pp. 381–390 in *SPE/ISRM Rock Mechanics in Petroleum Engineering* (Trondheim, Norway, 1998), Society of Petroleum Engineers, Richardson, TX, 1998.
- [Asgian et al. 1995] M. I. Asgian, P. A. Cundall, and B. H. G. Brady, “The mechanical stability of propped hydraulic fractures: a numerical study”, *J. Petrol. Technol.* **47**:3 (1995), 203–208.
- [Barree and Conway 2001] R. D. Barree and M. W. Conway, “Proppant holdup, bridging, and screen-out behavior in naturally fractured reservoirs”, in *SPE Production and Operations Symposium* (Oklahoma City, 2001), Society of Petroleum Engineers, Richardson, TX, 2001.

- [Brazgina et al. 2016] O. V. Brazgina, E. A. Ivanova, and E. N. Vilchevskaya, “Saturated porous continua in the frame of hybrid description”, *Contin. Mech. Therm.* **28**:5 (2016), 1553–1581.
- [Canon et al. 2003] J. M. Canon, D. J. Romero, T. T. Pham, and P. P. Valko, “Avoiding proppant flowback in tight-gas completions with improved fracture design”, in *SPE Annual Technical Conference and Exhibition* (Denver, 2003), Society of Petroleum Engineers, Richardson, TX, 2003.
- [Ely et al. 1990] J. W. Ely, W. T. Arnold III, and S. A. Holditch, “New techniques and quality control find success in enhancing productivity and minimizing proppant flowback”, pp. 889–898 in *SPE Annual Technical Conference and Exhibition* (New Orleans, 1990), Society of Petroleum Engineers, Richardson, TX, 1990.
- [Ivanova et al. 2016] E. A. Ivanova, E. N. Vilchevskaya, and W. H. Müller, “Time derivatives in material and spatial description — what are the differences and why do they concern us?”, pp. 3–28 in *Advanced methods of continuum mechanics for materials and structures*, edited by K. Naumenko and M. Aßmus, *Advanced Structured Materials* **60**, Springer, 2016.
- [Larsen and Smith 1985] D. G. Larsen and L. J. Smith, “New conductivity found in angular blends of fracturing sand”, pp. 205–210 in *SPE Production Operations Symposium* (Oklahoma City, 1985), Society of Petroleum Engineers, Richardson, TX, 1985.
- [Lu et al. 2016] W. Lu, B. O’Neil, K. Zhang, C. Wang, and H. Quintero, “Enhancing proppant flowback control through surface treatment of proppant”, in *International Petroleum Technology Conference* (Bangkok, 2016), International Petroleum Technology Conference, Richardson, TX, 2016.
- [Manderscheid and Gyekenyesi 1987] J. M. Manderscheid and J. P. Gyekenyesi, “Fracture mechanics concepts in reliability analysis of monolithic ceramics”, NASA Technical Memorandum 100174, NASA Lewis Research Center, 1987, <https://ntrs.nasa.gov/search.jsp?R=19870017836>.
- [McLennan et al. 2015] J. McLennan, I. Walton, J. Moore, D. Brinton, and J. Lund, “Proppant backflow: mechanical and flow considerations”, *Geothermics* **57** (2015), 224–237.
- [Milton-Taylor et al. 1992] D. Milton-Taylor, C. Stephenson, and M. I. Asgian, “Factors affecting the stability of proppant in propped fractures: results of a laboratory study”, pp. 569–580 in *SPE Annual Technical Conference and Exhibition* (Washington, DC, 1992), Society of Petroleum Engineers, Richardson, TX, 1992.
- [Vo et al. 2014] L. K. Vo, P. D. Nguyen, F. Liang, and C. Parton, “Enhancing proppant pack conductivity with consolidation and agglomeration performance: a laboratory study”, in *SPE International Symposium and Exhibition on Formation Damage Control* (Lafayette, LA, 2014), Society of Petroleum Engineers, Richardson, TX, 2014.

Received 5 Sep 2018. Revised 4 Oct 2018. Accepted 11 Nov 2018.

KSENIA P. FROLOVA: [kspfrolova@gmail.com](mailto:kspfrolova@gmail.com)

POLINA M. GRIGOREVA: [polina.grigoreva239@gmail.com](mailto:polina.grigoreva239@gmail.com)

*Peter the Great Saint Petersburg Polytechnic University, Saint Petersburg, Russia*

and

*Institute for Problems in Mechanical Engineering, Russian Academy of Sciences, Saint Petersburg, Russia*

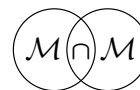
KONSTANTIN E. LEZHNEV: [lezhnev.ke@gazpromneft-ntc.ru](mailto:lezhnev.ke@gazpromneft-ntc.ru)

GRIGORIY V. PADERIN: [paderin.gv@gazpromneft-ntc.ru](mailto:paderin.gv@gazpromneft-ntc.ru)

*Gazprom-neft Science & Technology Centre, Saint Petersburg, Russia*







## THE OBJECT DETECTION BY AUTONOMOUS APPARATUS AS A SOLUTION OF THE BUFFON NEEDLE PROBLEM

MIKHAIL A. GUZEV, GURAMI S. TSITSIASHVILI AND MARINA A. OSIPOVA

The problem of object detection by autonomous apparatus is considered. The probabilistic formulation of the problem is proposed by means of a reduction to the classical Buffon problem. The latter naturally arises when the problem is formulated in the coordinate system associated with the apparatus. The problem of detection is considered for devices moving in the open space along a circle around one body, for vehicles patrolling along the linear boundary protecting the bodies, and for devices protecting the system of bodies. The problem of object detection was shown to admit an analysis in the presence of an asymptotic parameter determined by the ratio of the local size of the apparatus scanning area to the global size of the problem under consideration. For all problems, the minimum number of apparatuses that could detect a penetrating object with probability one was calculated.

### 1. Introduction

Nowadays, the attention of researchers is focused on the study of self-propelled particle systems [Della Corte et al. 2016; Brambilla et al. 2013; Bellomo and Brezzi 2016; Adamatzky and Jones 2008; Herrero and Soler 2015]. Analysis of these systems leads to the need to solve various problems closely related to the theory of dynamical systems. The simplest systems can be the systems of particles studied in the framework of Maxwell–Boltzmann, Fermi–Dirac, and Bose–Einstein statistics [Kardar 2007]. Billiard systems, where stochastic properties can arise even with a small number of particles and in the absence of random factors [Zaslavsky 2007], are an important analogue of self-propelled particles systems.

When considering the self-propelled particle systems, the number of particles is, as a rule, assumed to be sufficiently large. In particular, such assumptions are used in modeling the movement of vehicles, crowds and flocks, financial markets, and other socio-economic systems [Herrero and Soler 2015], consisting of a sufficiently large number of self-driven particles. In this connection, one should point out

---

**Communicated by Francesco dell’Isola.**

*MSC2010:* primary 60D05; secondary 70Q05.

*Keywords:* extraneous mobile object, autonomous unmanned vehicle, detection probability.

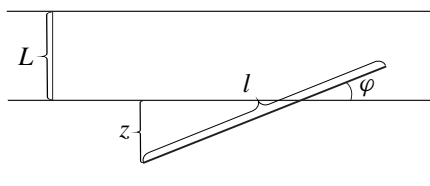


**Figure 1.** The Buffon needle problem.

the model of the quantum economy [Maslov 2005], in which a large number of self-driven particles leads to the appearance of synergistic effects — the nonlinear (exponential or power) dependence of the efficiency indicators on the number of particles.

At the same time, the self-propelled particle systems are close to the mobile robot systems that can be equipped with artificial intelligence. To describe the dynamics of the mobile robot systems, the models of differential games [Alspach 2004; Chung et al. 2011; Galceran and Carreras 2013], random graph models [Hazra et al. 2018; 2017a; 2017b], which underlie many artificial intelligence systems, etc., are used. Within these model frameworks, different problems are solved: determination of the shortest trajectory of a robot or a group of robots which covers the entire field of vision [Alspach 2004; Galceran and Carreras 2013], searching for the minimum number of robots that guarantee the capture [Chung et al. 2011], and many others.

This paper is devoted to solving the problem of calculating the detection probability of a mobile object penetrating through a system of mobile robots modeled by self-propelled particles and not possessing a sufficiently developed artificial intelligence. Such a problem may arise when designing a system of mobile robots that track the object penetration into a controlled area at sea, on land, in air, etc.

We analyze this problem using the solution of Buffon’s problem [Kendall and Moran 1963; Ambartzumian 1982] about calculating the probability of intersection of a random segment on a plane with a system of parallel lines. This model takes into consideration the kinematic and geometric features of the movement of mobile robots and the mobile object much more fully.

The Buffon problem (see Figure 1) is the determination of the probability of intersection of a needle with length  $l$ , which is randomly thrown onto a plane ruled by equally spaced parallel lines a distance  $L$  apart, with any one of these lines. This problem formed the basis for stochastic geometry and was widely used in applied statistics. The main elements of the probabilistic model in the Buffon problem are the random variables that determine the mutual position of the segment, occupied on the plane by the needle, and the equally spaced horizontal lines [Ambartzumian 1982; Kendall and Moran 1963]. The distance  $z$  from the segment’s lower end to

the first overlying line and the angle  $\varphi < \pi$  between this line and the segment are such random variables. Knowing the distribution law of the random vector  $(z, \varphi)$  formed by these random variables, we can determine the probability of the event  $P(l \sin \varphi \geq z)$  of the needle intersection with one of the parallel straight lines. For this event to happen, it is necessary and sufficient that the segment intersect with a straight line lying directly above its lower end.

In this paper we tried to adopt the Buffon problem to consider object detection by autonomous apparatus. The article outline is as follows.

In Section 2 we describe the joint motion of the vehicles and the object in order to calculate the probability of the intersection of the trajectory of an object, which is moving toward the body, with the apparatus scanning area. To determine the probability of the object detection, this model is recorded in a coordinate system associated with devices moving along a circle around the protected body.

In Section 3, we performed an analytical study of the proposed model for movement of the vehicles and the object in the polar coordinate system. With a certain ratio between the linear size of the detection area and the size of the area of the devices' motion, this task differs little from the classical Buffon problem. The resulting reduction allows us to calculate the minimum number of vehicles at which the probability of detecting an object is close to one.

Cyclic motion of vehicles along a closed linear segment is analyzed in Section 4. To calculate the minimum number of vehicles for which the probability of the object detection is close to one, the approach proposed in Section 2 is used, which consists of a transition to the coordinate system of the moving device.

In Section 5, we consider the protection model of the network structure of bodies which are located in the nodes of a square lattice bounded by the circle along which the vehicles move. For two different strategies of the vehicles' movement, the minimum number of vehicles was determined at which the probability of the object detection is close to one, and the most effective strategy is indicated.

Section 6 presents the final comments on the study performed and identifies the statements of new problems that follow from the considerations made in this paper.

Material of the article is partially presented in [Guzev et al. 2018], which examines the vehicle's movement along a circle around a single protected body and along a straight line segment.

## **2. Buffon problem in the coordinate system associated with vehicles moving around a circle**

Let  $n$  vehicles move along a circle of radius  $R$  with a fixed linear velocity  $v$  and at an equal distance from each other. Each of these vehicles is equipped with circular radar with scanning radius  $r$  (see Figure 2). We will use the following symbols

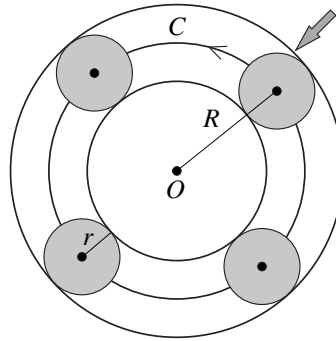


**Figure 2.** The vehicles' movement around a circle in a stationary coordinate system.

in all drawings: black dots are protected bodies, black arrows show the direction of vehicle motion, filled circles are the area of the locator survey, and wide filled arrows show the direction of object motion.

The circular radar can be understood as a vehicle that rotates a beam with an angular velocity large enough for the linear velocity of the beam to notably exceed the linear speed of the vehicle.

It is required to calculate the probability of detection of a mobile object by means of locators installed on the vehicles. By detection, we mean here that the object falls into a circle which is scanned by any of the vehicles.

The peculiarity of the task of calculating the probability of detecting a mobile object in a stationary coordinate system, associated with an external observer, is that both the vehicle and the object are moving, and therefore, some transition to the Buffon problem, in which at least parallel straight lines are fixed, is required.

Such a transition is realized when the motion of the object under study is considered in a coordinate system associated with vehicles rotating around a certain point  $O$  along a circle  $C$  of radius  $R$ . In this coordinate system, the radar scan circles with radius  $r$  become fixed. To be detected by the vehicle, the object trajectory should intersect one of these circles.

In order to simplify the study of this problem, we suppose that, in a stationary coordinate system, the mobile object moves with the velocity  $u$  along a segment connecting the starting point of its movement with the center  $O$  of the circle  $C$ .

In a rotating coordinate system, the shape of the object trajectory  $A_\psi$  differs from the segment (see Figure 3): it will be some curve that starts at a random point  $\psi$  of the circle  $C_*$ , with radius  $R + r$  and with center at  $O$ . Thus, in the coordinate system associated with the orbiting vehicles, circles of radius  $r$  play the role of parallel lines and curves  $A_\psi$  the role of the segments in the problem of Buffon.

We further assume everywhere in this paper that the random angle  $\psi$  has a uniform distribution on the segment  $[0, 2\pi]$ . The transition from the curve  $A_\psi$

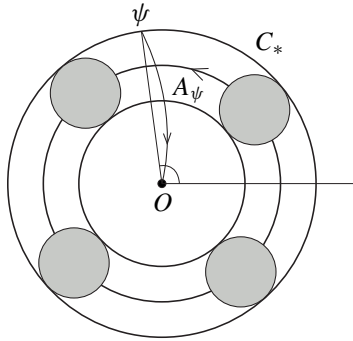


**Figure 3.** Trajectory of object motion in a Cartesian coordinate system associated with vehicles moving around a circle.

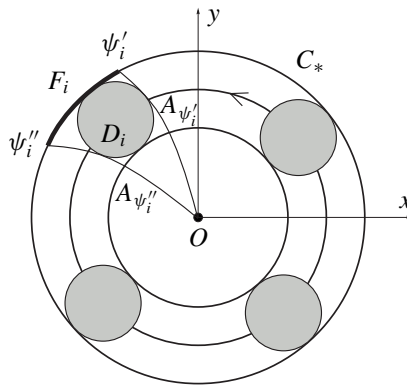


**Figure 4.** Control area of one circle of radar scan in the Cartesian coordinate system  $(x, y)$  associated with moving vehicles.

to the curve  $A_{\psi''}$  is carried out by rotation of the curve  $A_{\psi'}$  around the point  $O$  by the angle  $\psi'' - \psi'$ . It should be noted that, on the circle  $C_*$ , each circle  $D_i$  with radius  $r$  allocates an arc  $F_i$  bounded by two curves  $A_{\psi'_i}$  and  $A_{\psi''_i}$  that touch the circle  $D_i$ ,  $i = 1, \dots, n$ , from the outside (see Figure 4). Thus, on the circle  $C_*$ , the scan circle  $D_i$  with the center at the point, where the apparatus  $i$  is located, allocates the arc  $F_i$ ,  $i = 1, \dots, n$ . Now we can calculate the probability of detection of a mobile object by circular view radars installed on vehicles. Let the set  $\mathcal{F}$  be the union of the arcs  $F_i$ :  $\mathcal{F} = \bigcup_{i=1}^n F_i$ . This set is the union of a finite number of disjoint arcs (which may be less than  $n$ ). Then the total angular length  $s(\mathcal{F})$  of those arcs divided by  $2\pi$  is the required probability of detection a mobile object by radar locators installed on the vehicles.

Therefore, if the arcs  $F_i$ ,  $i = 1, \dots, n$ , do not intersect, the probability of the object detection by the vehicles is  $P = ns(F_i)/(2\pi)$ , where  $s(F_i)$  is the angular length of the arc  $F_i$ . In the general case,  $P = \min(1, ns(F_i)/(2\pi))$ .

### 3. Buffon problem in the polar coordinate system

The task of determining the curves  $A_\psi$  and finding the arcs  $F_i$  is solved, as a rule, numerically. However, at some additional assumptions, it is possible to obtain analytical formulas. Let us transition from the rectangular coordinate system  $(x, y)$  associated with the vehicle rotating around point  $O$  to the polar coordinate system (see Figure 5, left) with the vertical coordinate  $\rho = \sqrt{x^2 + y^2}$  and the horizontal coordinate  $\varphi = \arctan(x/y)$ .

In a rectangular coordinate system  $(x, y)$ , a circle of radius  $r$  centered at  $(O, R)$  is described by equations

$$x = x(\psi) = r \cos \psi, \quad y = y(\psi) = R + r \sin \psi, \quad 0 \leq \psi \leq 2\pi,$$

giving a parametric definition of the circle:  $\psi$  is a parameter. In the polar coordinate system  $(\rho, \varphi)$  this circle is given parametrically by the equations

$$\frac{\rho}{R} = \left( \frac{r^2}{R^2} \cos^2 \psi + \left( 1 + \frac{r}{R} \sin \psi \right)^2 \right)^{1/2}, \quad \varphi = \arctan \frac{(r/R) \cos \psi}{1 + (r/R) \sin \psi},$$

since  $\psi$  remains a parameter. A typical image of a circle with a radius  $r$  in this polar coordinate system looks like an oval with pointed upper end (see Figure 5, left). For small values of the parameter  $r/R \ll 1$ , the last system of equations can be approximated as

$$\frac{\rho}{R} \approx 1 + \frac{r}{R} \sin \psi, \quad \varphi \approx \frac{r}{R} \cos \psi.$$

Thus, a circle of radius  $r$  in the coordinate system  $(x, y)$ , rotating with the apparatus, transforms into almost a circle of radius  $r/R$  in a normalized polar coordinate system  $(\rho/R, \varphi)$  (see Figure 5, right). The linear speed of the vehicle is  $v$ , and

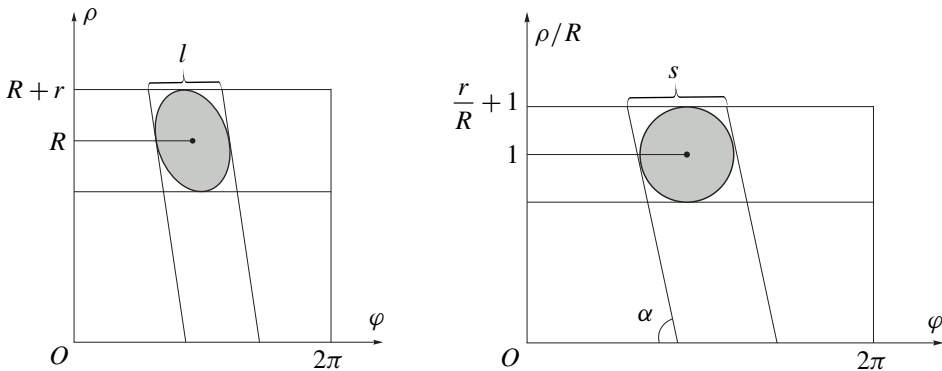


**Figure 5.** The control area of one circle of radar scan in the polar coordinate system (left) and in the normalized polar coordinate (right) associated with moving vehicles.

the speed of the mobile object in the fixed coordinate system is  $u$ , so in a fixed Cartesian coordinate system, the object moves to the center  $O$  of the circle  $C_*$  with velocity  $v$ , and the vehicles move along the circle  $C$  (in the angle  $\varphi$ ) with the angular velocity  $u/R$ . In the fixed polar coordinate system  $(\rho/R, \varphi)$ , the object moves along the radial coordinate  $\rho/R$  with velocity  $v/R$ , and the vehicles move along the angular coordinate  $\varphi$  with velocity  $u/R$ . Therefore, in the polar coordinate system  $(\rho/R, \varphi)$  associated with the vehicles, the vehicles are fixed, whereas the object moves along the radial coordinate  $\rho/R$  with the velocity  $v/R$ , and along the angular coordinate  $\varphi$  with velocity  $-u/R$  [Dreizler and Lüdde 2010].

Then, in the normalized polar coordinate system  $(\rho/R, \varphi)$  associated with the moving vehicles, the speed of the mobile object is equal to  $\sqrt{v^2 + u^2}/R$  and makes an angle  $\alpha = \arctan(u/v)$  with line  $\rho/R = 0$ . Therefore, each circle representing the control area of the radar locator overlaps a segment of length  $s = 2r/(R \sin \alpha)$  for the mobile object (see Figure 5, right).

Let's move from the probability of the object detection to the minimum number of vehicles  $M = \min(n : ns \geq 2\pi)$  at which the probability of a mobile object detection is equal to one; then

$$M = \min(n : nr \geq R \sin \alpha), \quad \frac{R \sin \alpha}{r} \leq M \leq \frac{R \sin \alpha}{r} + 1. \quad (1)$$

If the number of vehicles is  $n = M$ , then the distance between the centers of the neighboring survey circles can obviously be less than  $l$ .

#### 4. The movement of vehicles along a straight line

Now let the vehicles move along a segment  $BA$  of length  $L$  in one direction and, after reaching its end, turn and move in the opposite direction (see Figure 6). We believe that the distance between neighboring vehicles is  $2L/n$ ; a similar model was considered in [Kozhemyakin et al. 2017].

Then the scan circles associated with the vehicle locators move along the cylindrical surface with the generatrix  $A_*A_{**} = B_*B_{**}$  of length  $2r$  and the directrix

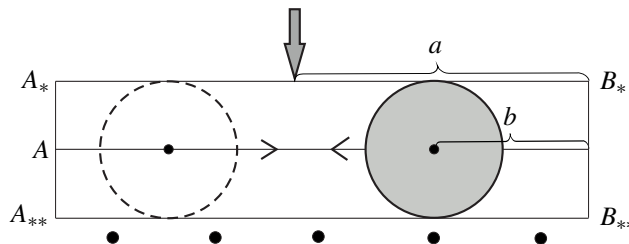


**Figure 6.** Vehicle and object motion in a fixed coordinate system. The bold arrow indicates the direction the object is moving.

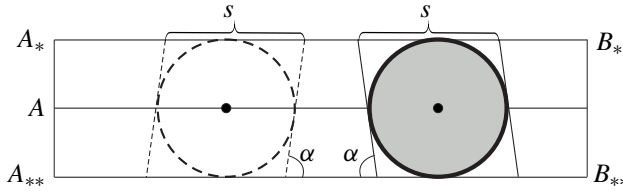


**Figure 7.** Vehicle and object motion in a coordinate system associated with the vehicles moving along the cylindrical surface.

$B_*A_*B_*$  of length  $2L$ . In a fixed coordinate system, the object moves vertically, and its horizontal coordinate at the time of crossing the strip is  $a$ ,  $0 \leq a \leq L$ . Let's transition to the coordinate system associated with the vehicles moving along the cylindrical surface and denote as  $b$  the distance from point  $B$  to the nearest vehicle in the movement direction (from right to left in Figure 6).

Let the probabilistic distribution of the random vector  $(a, b)$  be uniform on the rectangle  $[0, L] \times [0, 2L/n]$ . Then, in the coordinate system associated with moving vehicles, we can specify subsegments of length  $l = 2r / \sin \alpha$  on the segment  $A_*B_*$ , where the object can be detected (see Figure 7).

The task of calculating the probability of the object detection is more complicated when the vehicles are moving along a straight line but not along a circle. A relatively simple solution to this problem was obtained by transitioning from the probability of the object detection to the minimum number  $M$  of apparatuses for which the probability of the object detection is equal to one, namely  $M = \min(n : nr \geq L \sin \alpha)$ . Such a technique can be applied for multiagent systems, considered in [Maggio et al. 2013].

### 5. Protection of the net structure

The network structure consists of bodies in the nodes of a square lattice located inside a large circle. To protect the network structure, the following strategies can be proposed. The first strategy involves the protection of each body separately (see Figure 8, left). Let  $M_1(n)$  be the minimum number of devices that implement this strategy. However, we are trying to choose a defense strategy that reduces the number of devices. Therefore, we propose a second strategy to protect the entire network structure (see Figure 8, right). The minimum number of machines implementing the second strategy is denoted by  $M_2(n)$ . The calculation of  $M_1(n)$  and  $M_2(n)$  is based on formula (1), which determines the minimum number of vehicles moving around the body at the center of the circle.

For convenience in describing various ways to protect the network structure of bodies from object penetration, we transition from a Cartesian coordinate system  $(x, y)$  to a system of dimensionless coordinates  $(X, Y)$ ,  $X = x / (2(r + R))$  and

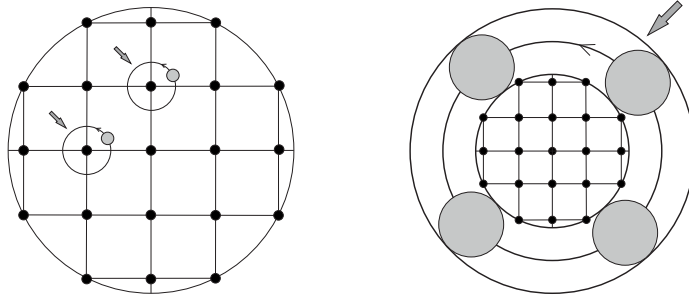


**Figure 8.** Strategies of apparatus motion: first (left) and second (right).

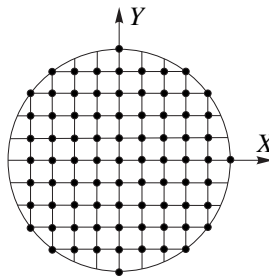


**Figure 9.** The location of bodies in the network structure.

$Y = y/(2(r + R))$ ). The parameters  $r$  and  $R$  were defined earlier in Section 2. In this coordinate system, a circle of radius  $r + R$  is transformed into a circle of radius  $\frac{1}{2}$ . In the coordinate system  $(X, Y)$ , consider a circle  $C_n$  of radius  $n$  centered at the coordinate origin and an integer square lattice (see Figure 9). Suppose that there are bodies in the nodes of this lattice inside the circle  $C_n$ , and  $N(n)$  denotes the number of these bodies. In the original coordinate system  $(x, y)$ , the circle  $C_n$  has a radius  $T_n = 2(r + R)n$ .

Around each of these bodies, its own group of vehicles moves along a circle of radius  $R/(r2(r + R))$ ; in the coordinate system  $(x, y)$ , this circle has radius  $R$ . Obviously, these circles do not intersect each other and lie entirely in a circle of radius  $n + 1$ . Then, in accordance with (1),  $M_1(n) \sim N(n)$ ,  $N(n) \gg 1$ , vehicles are needed to find with probability one an object that can move to any of these  $N(n)$  bodies, and by virtue of (1),

$$N(n)f \leq M_1(n) \leq N(n)(f + 1), \quad f = \frac{R \sin \alpha}{r}. \tag{2}$$

Consider an alternative protection system for  $N(n)$  bodies, assuming that the vehicles move along a circle with a center at  $(0, 0)$  and a radius of  $n + 1$ ; in the  $(x, y)$  coordinate system, the radius of this circle is  $2(n + 1)(r + R)$ . Then the

minimum number of vehicles  $M_2(n)$  moving along a circle of radius  $2(n+1)(R+r)$  (in the coordinate system  $(x, y)$ ) satisfies the relations

$$2(n+1)g \leq M_2(n) \leq 2(n+1)g + 1, \quad g = \frac{(R+r) \sin \alpha}{r}. \quad (3)$$

We now use the known estimates for  $N(n)$ . So in [Hardy 1999] an estimate of Gauss is given, showing that the number  $N(n)$  is equal to the area of the figure composed of unit squares of the lattice, for which the lower left corner lies in the circle  $C_n$ . Since the greatest distance between the points of the unit square does not exceed  $\sqrt{2}$ , all unit squares that intersect the boundary of the circle  $C_n$  are located in the ring

$$\{(X, Y) : (n - \sqrt{2})^2 \leq X^2 + Y^2 \leq (n + \sqrt{2})^2\}$$

with area  $4\pi\sqrt{2}n$ . Therefore, relations

$$\left| \frac{N(n)}{\pi n^2} - 1 \right| \leq \frac{4\sqrt{2}}{n} \implies N(n) \sim \pi n^2, \quad n \gg 1 \quad (4)$$

hold.

Thus,  $M_1(n) \sim N(n) \sim n^2$  and  $M_2(n) \sim n, n \gg 1$  (it follows from (3) and (4)). Combining relations (2)–(4), we obtain that for  $n \gg 1$  estimates  $M_1(n)/M_2(n) \sim n$  are valid.

Consequently, the application of the protection of the body system reduces the number of vehicles in proportion to  $n \gg 1$  compared to the protection of each body separately. The value of  $n$  is equal to the radius  $T_n$  of the large circle which surrounds the lattice points, divided by the lattice step  $2(r + R)$ .

The estimation of the  $N(n)$  value, given in (4), was repeatedly refined. Thus, Gauss showed that  $|N(10)/(\pi \cdot 10^2) - 1| \leq \frac{1}{100}$ , whereas for  $n = 10$  the right-hand side of inequality (4) is approximately equal to  $\frac{566}{1000}$ . The refinement of the estimation of the  $N(n)$  value [Hardy 1915; Huxley 2002] continues nowadays and is one of the key problems of analytic number theory.

It should be emphasized in conclusion that we considered a dynamic version of the Buffon problem which includes such characteristics as the trajectories and speeds of the mobile extraneous object and unmanned underwater vehicles. This circumstance leads to the necessity of transitioning to coordinate systems associated with moving vehicles and to additional, not always obvious, geometric constructions and the application of the small parameter method.

In addition to the trajectory of the object movement to the center  $O$  of circle  $C$  (see Figure 2) along the radius, other trajectories are possible, for example, helically [Guzev et al. 2017]. In this case, the body is protected if the viewing circle of each locator intersects with the viewing circle of another locator (see Figure 10). The

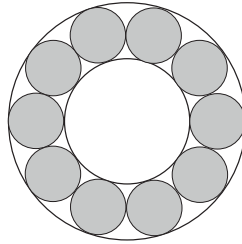


**Figure 10.** The disposition of the viewing circles of the locators to control the object movement along an arbitrary trajectory.

minimum number of devices detecting an object with probability one is  $M' = \min(n : ns' \geq 2\pi)$ ,  $s' = 2d$  and  $d = \arcsin(r/R)$ , and hence  $\pi/d \leq M' \leq \pi/d + 1$ .

Let  $M'_1(n)$  be the minimum number of vehicles that provide the detection of the object arbitrarily moving towards each body in the specified system; then

$$N(n) \frac{\pi}{d} \leq M'_1(n) \leq N(n) \left( \frac{\pi}{d} + 1 \right). \tag{5}$$

Let  $M'_2(n)$  be the minimal number of vehicles moving along a circle of radius  $2(n + 1)(R + r)$  and providing detection of an object in its arbitrary moving; then

$$\pi \left( \arcsin \frac{r}{2(n + 1)(R + r)} \right)^{-1} \leq M'_2(n) \leq \pi \left( \arcsin \frac{r}{2(n + 1)(R + r)} \right)^{-1} + 1. \tag{6}$$

From (4)–(6) we obtain that, in the case of an object with arbitrary motion, the protection of a system of bodies also requires a smaller number of vehicles than the protection of each body separately. The decrease in the vehicle number is proportional to  $n \gg 1$ , equal to the radius  $T_n$  divided by the step length of the lattice  $2(r + R)$ :  $M'_1(n)/M'_2(n) \sim n$ .

### 6. Conclusions

In searching for a solution to the problem of detecting the object, which is moving to the protected body, we came to the classical Buffon model. With such a reduction, obtaining the corresponding analytical results of the original problem turned out to be possible, provided that the vehicles move along a circle around the protected body. The constructed solution was used to analyze the possibilities of protecting the network structure of the body system. Note that the application of the results obtained for a single body to the body system became possible due to the homogeneity of the internal structure of the system and to the preservation of the geometry of the original problem at the system boundary. In particular, such a structure homogeneity is fixed by choosing the same scales in two orthogonal directions, and the geometry of the boundary is given by a circle.

The generalization of the results obtained is possible if we expand the set of the vehicles' trajectories. For engineering applications, the use of the zigzag motions is of interest [Galceran and Carreras 2013; Tuphanov and Scherbatyuk 2015], the effectiveness of which is confirmed in practice. However, an understanding of the fundamental aspects of the choice of control parameters for such a strategy is a blind spot of modern model theory. Therefore, gaining new knowledge for researchers engaged in this field is undoubtedly relevant.

### Acknowledgments

The authors are grateful to corresponding member of Russian Academy of Sciences A. F. Shcherbatyuk for useful discussions.

This work was partially supported by the Far Eastern Branch of the Russian Academy of Sciences (program "Far East" projects 18-5-050 and 18-5-083) and by the Russian Foundation for Basic Research (project 17-07-00177).

### References

- [Adamatzky and Jones 2008] A. Adamatzky and J. Jones, "Towards *Physarum* robots: computing and manipulating on water surface", *J. Bionic Eng.* **5**:4 (2008), 348–357.
- [Alspach 2004] B. Alspach, "Searching and sweeping graphs: a brief survey", *Matematiche (Catania)* **59**:1–2 (2004), 5–37.
- [Ambartzumian 1982] R. V. Ambartzumian, *Combinatorial integral geometry: with applications to mathematical stereology*, Wiley, 1982.
- [Bellomo and Brezzi 2016] N. Bellomo and F. Brezzi, "Mathematics, complexity and multiscale features of large systems of self-propelled particles", *Math. Models Methods Appl. Sci.* **26**:2 (2016), 207–214.
- [Brambilla et al. 2013] M. Brambilla, E. Ferrante, M. Birattari, and M. Dorigo, "Swarm robotics: a review from the swarm engineering perspective", *Swarm Intell.* **7**:1 (2013), 1–41.
- [Chung et al. 2011] T. H. Chung, G. A. Hollinger, and V. Isler, "Search and pursuit-evasion in mobile robotics", *Auton. Robot.* **31**:4 (2011), 299–316.
- [Della Corte et al. 2016] A. Della Corte, A. Battista, and F. dell'Isola, "Referential description of the evolution of a 2D swarm of robots interacting with the closer neighbors: perspectives of continuum modeling via higher gradient continua", *Int. J. Nonlin. Mech.* **80** (2016), 209–220.
- [Dreizler and Lüdde 2010] R. M. Dreizler and C. S. Lüdde, *Theoretical mechanics: theoretical physics, I*, Springer, 2010.
- [Galceran and Carreras 2013] E. Galceran and M. Carreras, "A survey on coverage path planning for robotics", *Robot. Auton. Syst.* **61**:12 (2013), 1258–1276.
- [Guzev et al. 2017] M. A. Guzev, G. Sh. Tsitsiashvili, M. A. Osipova, and M. S. Sporyshev, "Probability of detection of an extraneous mobile object by autonomous unmanned underwater vehicles", pp. 426–432 in *7th All-Russian Scientific and Technical Conference "Technical Problems of the Development of the World Ocean"* (Vladivostok, Russia, 2017), Institute for Problems of Marine Technologies, Vladivostok, Russia, 2017. In Russian.

- [Guzev et al. 2018] M. A. Guzev, G. Sh. Tsitsiashvili, M. A. Osipova, and M. S. Sporyshev, “Probability of detection of an extraneous mobile object by autonomous unmanned underwater vehicles as a solution of the Buffon problem”, preprint, 2018. arXiv
- [Hardy 1915] G. H. Hardy, “On the expression of a number as the sum of two squares”, *Quart. J. Math.* **46** (1915), 263–283.
- [Hardy 1999] G. H. Hardy, *Ramanujan: twelve lectures on subjects suggested by his life and work*, 3rd ed., American Mathematical Society, Providence, RI, 1999.
- [Hazra et al. 2017a] T. Hazra, C. R. S. Kumar, and M. Nene, “Multi-agent target searching with time constraints using game-theoretic approaches”, *Kybernetes* **46**:8 (2017), 1278–1302.
- [Hazra et al. 2017b] T. Hazra, M. J. Nene, and C. R. S. Kumar, “A strategic framework for searching mobile targets using mobile sensors”, *Wireless Pers. Commun.* **95**:4 (2017), 4681–4696.
- [Hazra et al. 2018] T. Hazra, M. J. Nene, and C. R. S. Kumar, “Modelling and analysis of information-based target searching using mobile sensors”, *Int. J. Sys. Cont. Commun.* **9**:1 (2018), 53–74.
- [Herrero and Soler 2015] M. A. Herrero and J. Soler, “Cooperation, competition, organization: the dynamics of interacting living populations”, *Math. Models Methods Appl. Sci.* **25**:13 (2015), 2407–2415.
- [Huxley 2002] M. N. Huxley, “Integer points, exponential sums and the Riemann zeta function”, pp. 275–290 in *Number theory for the millennium, II* (Urbana, IL, 2000), edited by M. A. Bennett et al., Peters, Natick, MA, 2002.
- [Kardar 2007] M. Kardar, *Statistical physics of fields*, Cambridge University, 2007.
- [Kendall and Moran 1963] M. G. Kendall and P. A. P. Moran, *Geometrical probability*, Griffin’s Statistical Monographs & Courses **10**, Hafner, New York, 1963.
- [Kozhemyakin et al. 2017] I. V. Kozhemyakin, D. V. Nikishenko, V. A. Ryzhov, N. N. Semenov, and M. N. Chemodanov, “Development the system of autonomous group management for heterogeneous surface and underwater unmanned vehicles”, pp. 48–57 in *7th All-Russian Scientific and Technical Conference “Technical Problems of the Development of the World Ocean”* (Vladivostok, Russia, 2017), Institute for Problems of Marine Technologies, Vladivostok, Russia, 2017. In Russian.
- [Maggio et al. 2013] M. Maggio, E. Bini, G. Chasparis, and K.-E. Årzén, “A game-theoretic resource manager for RT applications”, pp. 57–66 in *Proceedings of the 25th Euromicro Conference on Real-Time Systems* (Paris, 2013), IEEE Computer Society, Los Alamitos, CA, 2013.
- [Maslov 2005] V. P. Maslov, “Nonlinear averages in economics”, *Math. Notes* **78**:3–4 (2005), 347–363.
- [Tuphanov and Scherbatyuk 2015] I. E. Tuphanov and A. Ph. Scherbatyuk, “A centralized planner considering task spatial configuration for a group of marine vehicles: field test results”, pp. 1679–1684 in *2015 IEEE/RSJ International Conference on Intelligent Robots and Systems* (Hamburg, 2015), IEEE, Piscataway, NJ, 2015.
- [Zaslavsky 2007] G. M. Zaslavsky, *The physics of chaos in Hamiltonian systems*, 2nd ed., Imperial College, London, 2007.

Received 9 Jan 2019. Revised 21 Apr 2019. Accepted 27 Jun 2019.

MIKHAIL A. GUZEV: guzev@iam.dvo.ru

GURAMI SH. TSITSIASHVILI: guram@iam.dvo.ru

MARINA A. OSIPOVA: mao1975@list.ru

*Institute for Applied Mathematics, Far Eastern Branch, Russian Academy of Sciences, Vladivostok, Russia*





## Guidelines for Authors

Authors may submit manuscripts in PDF format on-line at the submission page.

**Originality.** Submission of a manuscript acknowledges that the manuscript is original and is not, in whole or in part, published or under consideration for publication elsewhere. It is understood also that the manuscript will not be submitted elsewhere while under consideration for publication in this journal.

**Language.** Articles in MEMOCS are usually in English, but articles written in other languages are welcome.

**Required items.** A brief abstract of about 150 words or less must be included. It should be self-contained and not make any reference to the bibliography. If the article is not in English, two versions of the abstract must be included, one in the language of the article and one in English. Also required are keywords and a Mathematics Subject Classification or a Physics and Astronomy Classification Scheme code for the article, and, for each author, postal address, affiliation (if appropriate), and email address if available. A home-page URL is optional.

**Format.** Authors are encouraged to use L<sup>A</sup>T<sub>E</sub>X and the standard amsart class, but submissions in other varieties of T<sub>E</sub>X, and exceptionally in other formats, are acceptable. Initial uploads should normally be in PDF format; after the refereeing process we will ask you to submit all source material.

**References.** Bibliographical references should be complete, including article titles and page ranges. All references in the bibliography should be cited in the text. The use of B<sub>I</sub>B<sub>T</sub><sub>E</sub>X is preferred but not required. Tags will be converted to the house format, however, for submission you may use the format of your choice. Links will be provided to all literature with known web locations and authors are encouraged to provide their own links in addition to those supplied in the editorial process.

**Figures.** Figures must be of publication quality. After acceptance, you will need to submit the original source files in vector graphics format for all diagrams in your manuscript: vector EPS or vector PDF files are the most useful.

Most drawing and graphing packages — Mathematica, Adobe Illustrator, Corel Draw, MATLAB, etc. — allow the user to save files in one of these formats. Make sure that what you are saving is vector graphics and not a bitmap. If you need help, please write to [graphics@msp.org](mailto:graphics@msp.org) with as many details as you can about how your graphics were generated.

Bundle your figure files into a single archive (using zip, tar, rar or other format of your choice) and upload on the link you been provided at acceptance time. Each figure should be captioned and numbered so that it can float. Small figures occupying no more than three lines of vertical space can be kept in the text (“the curve looks like this:”). It is acceptable to submit a manuscript with all figures at the end, if their placement is specified in the text by means of comments such as “Place Figure 1 here”. The same considerations apply to tables.

**White Space.** Forced line breaks or page breaks should not be inserted in the document. There is no point in your trying to optimize line and page breaks in the original manuscript. The manuscript will be reformatted to use the journal’s preferred fonts and layout.

**Proofs.** Page proofs will be made available to authors (or to the designated corresponding author) at a Web site in PDF format. Failure to acknowledge the receipt of proofs or to return corrections within the requested deadline may cause publication to be postponed.

- A polynomial chaos expanded hybrid fuzzy-stochastic model for transversely fiber reinforced plastics 99  
Eduard Penner, Ismail Caylak, Alex Dridger and Rolf Mahnken
- Dynamic boundary conditions for membranes whose surface energy depends on the mean and Gaussian curvatures 131  
Sergey Gavriluk and Henri Gouin
- Energy-based trajectory tracking and vibration control for multilink highly flexible manipulators 159  
Ivan Giorgio and Dionisio Del Vescovo
- A model of the proppant flowback: setup of the theoretical framework 175  
Ksenia P. Frolova, Polina M. Grigoreva, Konstantin E. Lezhnev and Grigoriy V. Paderin
- The object detection by autonomous apparatus as a solution of the Buffon needle problem 189  
Mikhail A. Guzev, Gurami S. Tsitsiashvili and Marina A. Osipova

*MEMOCS* is a journal of the International Research Center for the Mathematics and Mechanics of Complex Systems at the Università dell'Aquila, Italy.

